https://lib.uliege.be https://matheo.uliege.be

Mémoire

Auteur : Rondiat, Matéo
Promoteur(s) : Nguyen, Ngoc Duy; Silhanek, Alejandro
Faculté : Faculté des Sciences
Diplôme : Master en sciences physiques, à finalité approfondie
Année académique : 2024-2025
URI/URL : http://hdl.handle.net/2268.2/22981

Avertissement à l'attention des usagers :

Tous les documents placés en accès ouvert sur le site le site MatheO sont protégés par le droit d'auteur. Conformément aux principes énoncés par la "Budapest Open Access Initiative"(BOAI, 2002), l'utilisateur du site peut lire, télécharger, copier, transmettre, imprimer, chercher ou faire un lien vers le texte intégral de ces documents, les disséquer pour les indexer, s'en servir de données pour un logiciel, ou s'en servir à toute autre fin légale (ou prévue par la réglementation relative au droit d'auteur). Toute utilisation du document à des fins commerciales est strictement interdite.

Par ailleurs, l'utilisateur s'engage à respecter les droits moraux de l'auteur, principalement le droit à l'intégrité de l'oeuvre et le droit de paternité et ce dans toute utilisation que l'utilisateur entreprend. Ainsi, à titre d'exemple, lorsqu'il reproduira un document par extrait ou dans son intégralité, l'utilisateur citera de manière complète les sources telles que mentionnées ci-dessus. Toute utilisation non explicitement autorisée ci-avant (telle que par exemple, la modification du document ou son résumé) nécessite l'autorisation préalable et expresse des auteurs ou de leurs ayants droit.

Faculty of Sciences | Department of Physics

Morphological instabilities of silver nanowires induced by electric current injection

---

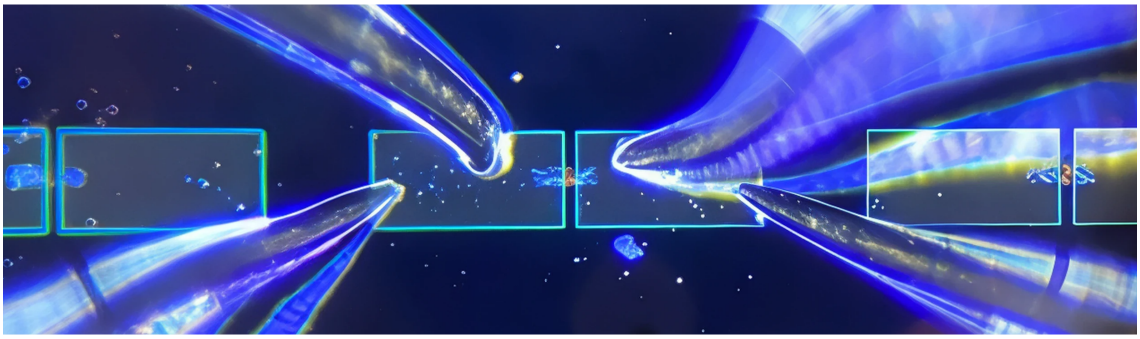

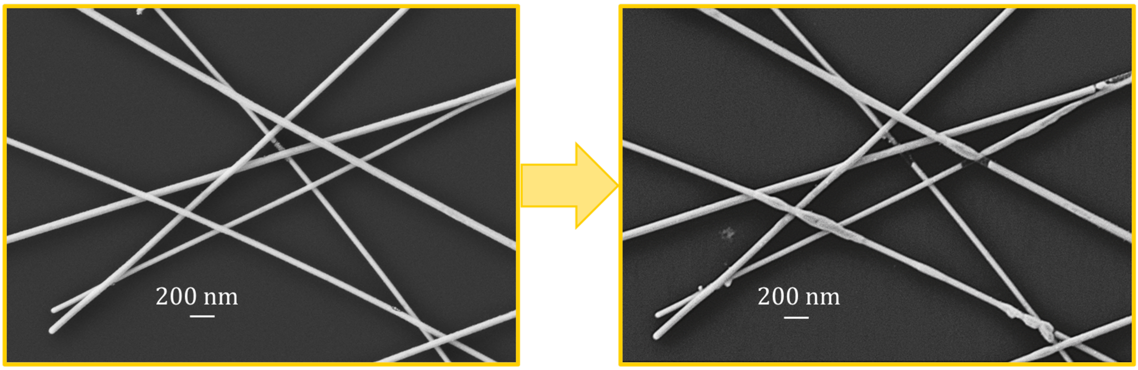

Master Thesis

Supervisors: Pr. Ngoc Duy Nguyen and Pr. Alejandro V. Silhanek

By Matéo RONDIAT

2024-2025

Acknowledgements

I would first like to thank Prof. Ngoc Duy Nguyen and Prof. Alejandro V. Silhanek for their invaluable help and guidance during our meetings and throughout the review of this work. This thesis could not have been completed without their support, and for that, they have my deepest gratitude.

I would also like to express my sincere thanks to Prof. Stéphane Dorbolo, Prof. Jean-Yves Raty, and Dr. François Damanet for kindly agreeing to serve on the jury and for their thorough review of this thesis.

I would also like to express my deepest gratitude to the PhD students François Balty and Amaury Baret for their help and patience in the laboratory, as well as during the initial reviews of this manuscript. Working alongside them allowed me to deepen my knowledge and take my first steps into the field of research.

I am also grateful to all the SPIN and EPNM members for their warm welcome. Thanks to this supportive and pleasant atmosphere, I was able to work and grow as a scientist in the best possible way.

Finally, I would like to thank my family and my girlfriend for their invaluable emotional support throughout this work. They never stopped believing in me, even during difficult times, and gave me the strength to keep moving forward with this project.

Contents

Introduction 1

Condensed matter physics investigates the origin of the macroscopic properties exhibited by materials. These properties often arise from local and topological aspects of the material. For instance, electrical resistance is related to the motion of electrons within the material and, consequently, to scattering events with phonons. Adopting a perspective at smaller scales makes it possible to explain these macroscopic properties. Transparency, conductivity, strength, weight, and hydrophobicity are typically properties that can be optimized and studied to manufacture devices exhibiting these characteristics. Over the past few decades, the development of new materials capable of combining such properties has been a focus in the worldwide community [1–3]. Developing such materials can broaden the possibilities for developing devices [4, 5] and reduce energy consumption in the field of optoelectronics [6].

For instance, transparent conductive materials (TCMs) are designed to achieve both high transparency and good electrical conductivity, which can be utilized to develop chromogenic devices [4, 7], light-emitting diodes [4, 8], dye-sensitized solar cells [4, 9], smart windows [4, 10]. However, these properties depend on phenomena occurring at the microscopic level and one property can be favoured while another is not. Typically, transparency and electrical conductivity are often in opposition [4]. Indeed, focusing on the band gap theory, transparency requires a material with a large band gap, such as an insulator, which has almost no free electrons, to minimize light absorption. In contrast, conductivity arises from an overlap between the conduction band and the valence band, a condition typically met in conductors such as metals, which are opaque at the nanoscopic scale. As a result, TCMs have been extensively studied for many years, with Indium Tin Oxide (ITO) currently standing as the leading material in this field. Indeed, it exhibits excellent optical transparency over the visible range (91.5% in the 400-1100 nm) as well as low resistance (sheet resistance of $\approx 10\,\Omega/\square$) [11]. However, thin films made of ITO present several drawbacks: they are brittle under mechanical stress, and the scarcity of indium complicates low-cost production [12]. Consequently, alternative materials based on conductive nanowires, such as silver nanowires (AgNWs), [13] have been explored to replace ITO [14].

AgNWs deposited onto a transparent substrate such as glass or transparent flexible polymers create pathways that allow current to flow at the surface of the material while photons can be transmitted through the gaps between wires [5]. In addition, compared to ITO, AgNW networks are mechanically flexible and compatible with low-cost and scalable fabrication processes [5]. They also exhibit notable thermal conductivity [15], which can be advantageous in thermal management applications.

Thanks to these properties, AgNWs show great potential for integration into a wide range of devices such as solar cells [13, 16], organic light-emitting diodes [17, 18], heaters [19], and thermal transparent conductive films [20]. However, NWs tend to exhibit instabilities when exposed to external constraints such as temperature, electric current, light, chemical environment, and mechanical bending, potentially degrading the network and its functional properties. Therefore, numerous studies have investigated the limitations of these networks under various forms of stress, including thermal [21–28], mechanical [29, 30], chemical [31], optical [32], and electrical [33–36]. Consequently, the study of thermal and electrical stress appears to be relevant in the context of the applications mentioned. While the effects of thermal stress have been extensively explored over the past decade, electrical stress has received less attention and is still an active area of research. This work therefore aims to investigate the behaviour of AgNW networks under electrical current injection.

It is established that AgNWs exhibit instabilities when subjected to electrical currents. These instabilities are often attributed to the Joule effect and/or electromigration [23, 33, 37, 38], which both induce atomic migration in the NWs. In this work, the origin of electrical failure is also investigated, with the aim of identifying the processes that trigger instabilities in AgNW networks under electrical stress. Furthermore, a study combining numerical modelling and experimental data is conducted to assess the limitations of the model established in this work and to potentially reveal unexplored instability mechanisms in AgNWs. The predicted electrical instabilities of the model are also investigated to highlight discrepancies between the experimental and simulated networks.

Chapter 2 is devoted to presenting the current state of research on instabilities in AgNW networks. It begins with an overview of thermal instabilities, which serves to motivate the study and provides a foundation for understanding the AgNW stabilities. This is followed by an introduction to electrical instabilities, focusing on the key mechanisms that can arise when current flows through AgNW networks, namely electromigration and Joule heating. A brief introduction to electrical breakdown is also included to establish a basis for understanding how such events could potentially occur in these networks. Finally, the chapter concludes with a short review of existing numerical models, highlighting potential gaps and uncertainties in the current literature.

Chapter 3 begins by describing the fabrication process of the samples and detailing each step required for sample preparation. Indeed, microscale networks are developed, which require specific steps for their fabrication. The experimental setup is then presented, providing insight into how the AgNW networks are characterized and tested. Finally, the numerical model is introduced as well as an explanation of how it is applied throughout this master's thesis.

Chapter 4 is dedicated to data analysis and discussion. Visual inspection through scanning electron microscopy (SEM) provides qualitative insights into the changes occurring in the AgNW networks after electrical failure, while quantitative data analysis allows for a more detailed interpretation of these results in parallel with the visual observations. In addition, the numerical model helps to predict and localize instabilities. The limitations of such predictions are also discussed to explain the discrepancies between the model and reality. Overall, these results provide insights into the critical current density leading to electrical failure in AgNWs, as well as the typical junction resistance within AgNW networks, while also revealing unexpected aspects of their behaviour under electrical stress.

State of the art 2

2.1 Silver nanowires

AgNWs have attracted significant interest over the past decades in the scientific community. Due to their nanoscale dimensions and their structure, they exhibit atypical properties that differ significantly from those of bulk materials. Indeed, AgNWs can exhibit different shapes depending on their synthesis methods [39] (e.g., the polyol method yields AgNWs with a pentagonal cross-section [40], while wet chemical synthesis produces AgNWs with a cubic crystal structure [41]). Particularly, in this work, AgNWs with a pentagonal cross-section are considered (see Figure 2.1).

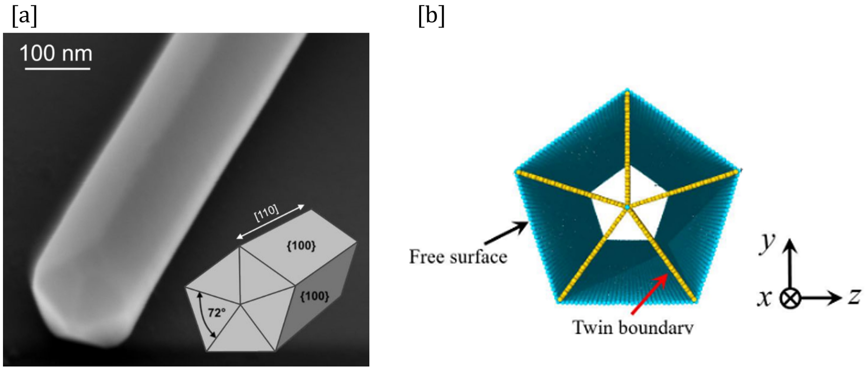

Figure 2.1: [a] SEM image of a single NW with a schematic drawing showing the five associated monocrystals reproduced from [42]. [b] Schematic drawing highlighting atoms breaking the symmetry of the monocrystal (at the surface and twin boundaries) reproduced from [42]. Atoms arranged according to the crystal structure were omitted from the illustration.

It is recognized that such pentagonal symmetry is incompatible with the overall energy minimization of the structure. This means that AgNWs are structurally metastable and thus more prone to morphological transformations when subjected to various stresses [43]. This could be an obstacle for several applications wherein NWs are subjected to thermal, mechanical and electrical stresses.

During the growth process, polyvinylpyrrolidone (PVP) is utilized as a capping agent which promotes the growth of the NW along a specific direction [44]. Moreover, the layer of PVP helps to stabilize the structure and to protect it from external factors, while suppressing the development of instabilities in the NW [44]. Even though this layer tends to stabilize the NWs, it also increases the electrical resistance of the network composed of these wires by heavily increasing the contact resistance between connected NWs [44, 45]. Thus, AgNWs are typically subjected to thermal annealing to eliminate the PVP layer, which, in turn, exposes them again to potential intrinsic instabilities.

As a result, considerable attention has been directed toward understanding these instabilities in AgNWs, with a focus on elucidating the mechanism that can trigger such morphological changes. For instance, thermal annealing is often employed to improve the conductive properties of AgNWs. Therefore, it is relevant to explore the instabilities induced by thermal stress. Hence, the underlying question is as follows: *can heat trigger structural instabilities in AgNWs?*

2.1.1 Thermal instability

This question has been extensively studied. Indeed, when NWs are subjected to thermal stress *spheroidization* can occur. This process is often compared to the Rayleigh-Plateau instability, which describes how a liquid jet breaks into a series of droplets due to surface tension-driven instabilities. Similarly, when NWs are subjected to high temperatures, they begin to fragment into small spheres (see Figure 2.2 [a], [b] and [c]) as a result of surface energy minimization. Spheroidization can be explained by the theory of McCallum et al. [46] and has been studied in detail by Balty et al. [22]. Contrary to Rayleigh-Plateau instabilities in liquid jet, temperature is a key parameter to trigger thermal instabilities in NWs. Indeed, this increase in temperature destabilizes the NWs, leading to compressive stress, which facilitates atomic migration (this aspect of atomic migration will be discussed in section 2.2.3).

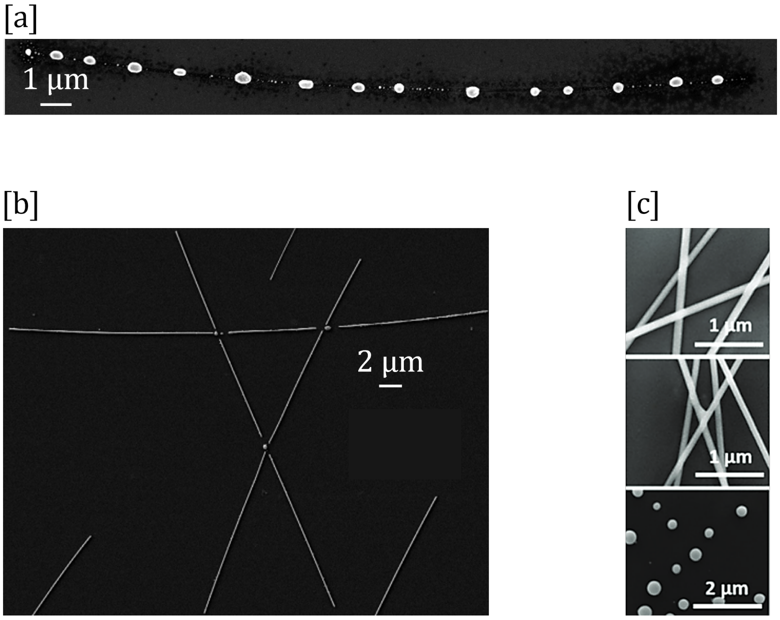

Figure 2.2: [a] SEM image of a completely spheroidized NW. [b] SEM image of partially spheroidized NW, indicating that thermal instabilities appear initially at the junction. [c] SEM image of a network undergoing thermal stress (respectively , 25 °C, 255 °C and 500 °C)

Alternatively, thermal stress can be beneficial to enhance the conductivity of the network [47]. It is well-known that the junctions at the intersections of two NWs play a major role in the overall resistance of the network due to the small contact area between two wires, as well as the potential presence of an insulating protective layer (PVP) around each NW. To better understand the processes occurring when networks are subjected to heat stress, an introduction to the different regimes of electric resistance is provided [23, 47, 48].

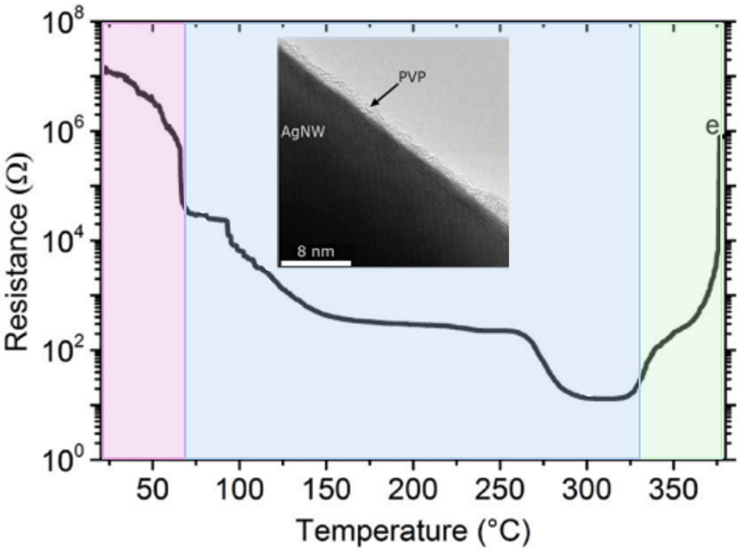

Figure 2.3: Evolution of a network's resistance as a function of temperature reproduced from [49]. Initially, the network has a resistance of approximately $10^7\,\Omega$, which corresponds to the non-conducting regime (purple box in the figure). The resistance then rapidly decreases due to the sintering effect (blue box in the figure). Finally, as the temperature continues to rise, the junctions degrade, leading to the rapid breakdown of the network. The coloured box highlights the different resistance regimes that a network may exhibit (green box in the figure).

1. **Non-conducting network** (purple box in Figure 2.3): the protective layer on AgNWs acts as an insulator, reducing the current flow through the network. As a result, the overall resistance of the network can be compared to that of an insulating material. This layer is often made of PVP, which functions as an insulating barrier around the nanowires.

2. **Sintering** (see blue box in Figure 2.3): with an increase in temperature, either due to global heating or to the Joule effect (Figure 2.9), the protective layer is removed, leading to the formation of new types of junctions, specifically metal-metal junctions. Moreover, if the temperature still increases, the junctions can initiate the sintering process, resulting in a reduction of the resistance associated with the junctions (see Figure 2.3). This sintering effect results in a decrease in the overall resistance, as the improved junctions allow for better conductivity (see Figure 2.4). This effect is also referred to as a 'welding' process, however, this term is improperly used [50]. Indeed, the junctions do not melt and recrystallize afterwards. The improvement is instead due to material diffusion at the junction, which tends to reduce resistance. Therefore, the term 'sintering' is preferred to describe this process.

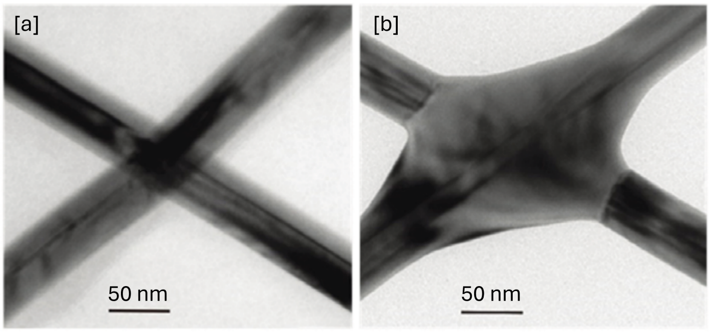

Figure 2.4: [a] SEM image of a non-annealed junction is shown. [b] The same junction has been thermally annealed, highlighting the differences between the two junctions [48].

3. **Breaking network** (green box in Figure 2.3): at a certain point, junctions or the wires themselves begin to deteriorate due to thermal instabilities, leading to the disruption of a percolating path. This phenomenon can eventually trigger the destruction of the percolating network (these concepts are defined in Box 1).

Moreover, other types of instabilities have been explored in the literature, including bending failure [51, 52], chemical failure [35, 53], and photodegradation [37], as well as different factors that could enhance these instabilities, such as the influence of the substrate [51] and corrosion [54]. These instabilities are directly associated with specific characteristics of these materials. For instance, bending failure is related to the functionality of AgNW networks. However, given that conductivity is the most commonly exploited property in devices incorporating NWs, it is particularly relevant to investigate instabilities related to electrical stress. This work therefore focuses on electrical instabilities, a subject that is not fully understood as of today.

2.2 Electrical instabilities

2.2.1 Parameters related to electrical instabilities

Beforehand, several parameters related to both AgNWs and conductivity must be introduced to understand the context of this work. AgNWs exhibit properties that cannot be explained by the classical theory of conductors. For instance, it has been observed that a single NW exhibits a resistivity different from that of the resistivity of bulk silver [55–57]. When the mean free path of the conducting electrons is comparable to or larger than the diameter of the conductor, the resistivity of the material must be modified. Moreover, it has been found that resistivity depends directly on the diameter of the NWs [34, 55, 56]. Indeed, Bid et al. proposed the following expression, which gives the resistivity of a single nanowire, ρ_{NW}, as a function of its diameter, D_{NW} (typically around dozen of nm), the resistivity of the bulk material, $\rho_{bulk} \approx 1.55 \times 10^{-8}\,\Omega\,\mathrm{m}$ [58], and the mean free path, $\Lambda \approx 520\,\text{Å}$ [59]:

$$\rho_{NW} = \rho_{bulk}(1 + \frac{\Lambda}{2D_{nw}})[56]. \tag{2.1}$$

Thanks to this resistivity the Pouillet's law can be applied to directly access the resistance of a single NWs. Thus, the resistance R becomes a function of the cross-sectional area A, length l, and the resistivity of the material in ρ_{NW},

$$R = \rho_{NW}\frac{l}{A}. \tag{2.2}$$

With this information on resistance, one might think that the resistance of an entire network can be easily obtained (e.g., by considering a nanowire as a resistive element in an electronic circuit and using classical circuit laws to calculate the network resistance). However, AgNWs exhibit a unique characteristic: the resistance of the junctions. This resistance is associated with the connection between two adjacent nanowires. Several studies have attempted to determine values for this junction resistance, and they show that it can play a major role in the overall resistance of the network and thus cannot be neglected [50, 60–64]. Nevertheless, it remains a poorly understood topic in the field of nanowires. If the junction resistances can be accessed and coupled with Pouillet's law, the resistance of the network can be quantitatively explained. However, this applies under the assumption that the network is conductive. This characteristic of conductive networks is described using percolation theory. A brief introduction to this theory is provided in Box 1, primarily to introduce terms relevant to both AgNWs and percolation theory.

Box 1: Percolation [65]

Percolation is a phenomenon in statistical physics that describes the formation of pathways in a stochastic system. It explains how a effect propagates through a structure, such as a viscous fluid penetrating a porous substrate, a fire spreading through a forest, a breakdown in a railway network, or, in the context of this work, the connection between two electrodes via the random deposition of NWs.

This theory is based on a two-dimensional system divided into small sites, where each site has a probability of being occupied or not. The occupied or non-occupied state does not have a strict definition and depends on the context and the system that is being studied. However, the global occupation of these sites is crucial in determining the propagation of a phenomenon through the system. A common way to illustrate percolation theory is to consider a square forest divided into discrete sites 2.5 [a], where each site may be occupied by a tree. Let's suppose that a fire starts at one edge of the forest, the key question for this situation is: *will the fire propagate from one side of the forest to the other ?* In fact, percolation theory can address this question. If percolation occurs, it means that the trees form a continuous path from one side to the other. In this case, the system is said to be percolating, and in our example, the fire will end up spreading from one side of the forest to the other.

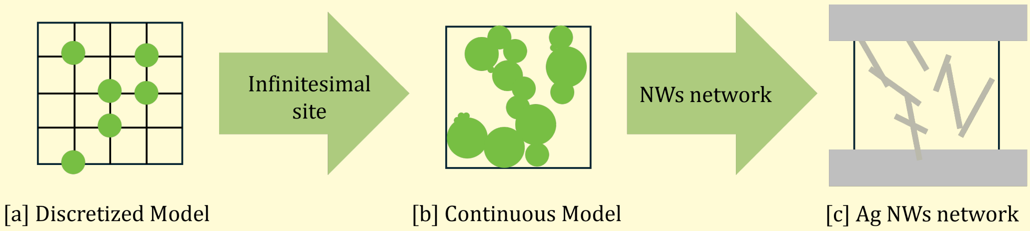

[a] Discretized Model

[b] Continuous Model

[c] Ag NWs network

Figure 2.5: [a] An example of the discretized model is shown. This situation illustrates a non-percolating system since no continuous path connects the two sides. [b] An example of the continuous model is provided. In this case, the system is percolating, as a path connects both sides. [c] An example of a typical percolating AgNWs network is presented.

Since sites do not naturally appear in most experiments, implementing a continuous theory seems particularly relevant for the application of this theory 2.5 [b]. Percolation in a continuous system can be deduced from the discretized model by reducing the distance between sites to an infinitesimal scale. In this case, the phenomenon can appear anywhere within the system.

This continuous theory can be applied to AgNW networks (see Figure 2.5 [c]) to understand typical parameters of the systems such as the resistance, but also it gives new vocabulary related to both percolation and field of AgNW networks. Indeed, a network where current can flow to one electrode to the other one is called *percolating* otherwise *non-percolating* [66]. Moreover, each NW that participated to the conduction of the current in the system is included in what is called the *percolating cluster*[66]. Alternatively, any path that connects the two electrodes is referred to as a *percolating path*.

As nanowires can be seen as resistive elements in a circuit, energy losses are observed in the form of thermal energy, also known as **Joule heating**. This heat generation can raise the temperature of the network, potentially inducing thermal instabilities caused by internal thermal stress. In addition, electrons can scatter off the ions in the crystal lattice. These interactions transfer momentum to the ions, leading to atomic displacement, a process referred to as **electromigration** (to be introduced and discussed in detail in Section 2.2.3). Furthermore, examination of AgNWs at microscopic length scales allows discussion of the phenomenon of **electrical breakdown**. Indeed, at this small scale, electrical breakdown may occur due to the high ratio between the applied voltage and the short length of the nanowire, making such instabilities more likely.

In the following sections, different aspects of AgNW instabilities will be introduced, along with their origins. However, explaining one instability without mentioning the others is a real challenge, since several instabilities are intertwined. For instance, the Joule heating effect tends to accelerate the electromigration process [37]. Therefore, the following sections discussing these two instabilities must be read in parallel, as both instabilities arise when a current is applied to an AgNW network.

2.2.2 Joule heating

Joule heating in classical conductors often leads to variations in several parameters. For instance, it is known that an elevation in temperature increases the phonon vibrations in a crystal, and therefore, electrons flowing within the material interact even more with the ions leading to more frequent collisions. As a result, charge carrier mobility is reduced, and the material's resistance increases as well. However, this Joule heating impact can be reversed simply by cooling down the material itself (i.e., by stopping the current injection). In that case, the evolution of the resistance is completely reversible, since the resistance of the conductor at a certain temperature remains the same before and after current injection. Since AgNWs are conductors, it could be inferred that they would exhibit the same characteristics. However, this is not the case, such an elevation in temperature will destabilize the network, leading to a non-reversible increase in resistance [33]. Indeed, Joule heating induces morphological instabilities in AgNWs, which can, in the worst cases, lead to wire breakdown. Therefore, even if the current is turned off, the network remains affected after the electrical stress, resulting in a non-reversible increase in resistance. Even though this resistance change arises from the increase in temperature, electromigration can also impact this non-reversible change in resistance (see Section 2.2.3).

Observations indicate that Joule heating tends to create *hot spots* within the network, particularly at junctions where resistance is highest [21, 23, 47]. Indeed, due to the distribution of current within a network, some wires can carry higher currents than others, leading to an increase in the Joule effect. Therefore, the network exhibits regions with higher temperatures, known as *hot spots*. However, other results also predict *hot spots* due to electromigration in nanoscale devices. Indeed, since electromigration produces a displacement of matter, it can create voids in the nanostructure. These voids will induce a redistribution of mass in the structure, leading to a non-constant resistance along the wire, meaning that *hot spots* are created due to electromigration [67]. If the generated heat reaches a sufficient high level at the junctions or at hot spots generated by electromigration, atomic diffusion may be triggered, leading to the spheroidization of the hot spot. In extreme cases, this atomic migration can ultimately destroy a part of the conductive path leading to an increase of the resistance [21, 35]. However, these results do not solely result from Joule heating. These breaking events may be further intensified by additional instabilities, such as electromigration.

2.2.3 Electromigration

Most of the time, when a current flows through a conductor, the electron flux is assumed to have no significant impact on the system. However, electrons have charge, momentum, and can interact with their environment. Therefore, under certain conditions, the current can induce a movement of matter, a phenomenon known as electromigration [68].

Dynamically, this corresponds to the transfer of momentum from conducting electrons to ions through scattering events, resulting in mass transport. This overall momentum transfer generates a drifting force commonly referred to as the 'electron wind force' [69]. Moreover, electromigration is facilitated by Joule heating, as the increased atomic vibrations enhance atomic mobility. However, the movement of matter is not exclusively driven by thermal effects and electrical current, other factors may also contribute 2.6.

Therefore, limiting the analysis of atomic migration solely to electromigration provides an incomplete picture of reality and other effects must be considered [70] (see Figure 2.6).

- **Concentration gradient**: when a difference in concentration exists within the material, diffusion can occur, leading to atomic motion driven by the gradient.
- **Thermomigration**: in regions of the solid with higher temperatures, ions have greater kinetic energy, allowing them to diffuse more easily within the lattice.
- **Stress-induced migration**: a stress gradient has three major effects: it acts as a driving force for atomic motion, leads to the formation of voids or extrusions, and directly alters the concentration distribution of ions.

All these effects, including electromigration, are accounted for in the general equation of atomic migration [70]. Where in Figure 2.6 n_v is the concentration of vacancies, D_v is their diffusivity, $Z^\star$ is defined as the sum of the valence of ions and the effective valence representing the amplitude of the net momentum transfer, e is the electron charge, ρ is the resistivity, $\vec{j}$ is the current, k is the Boltzmann's constant, T the temperature, κ is the thermal conductivity, σ is the mechanical stress, f and Ω are respectively the relaxation vacancy factor and the atomic volume.

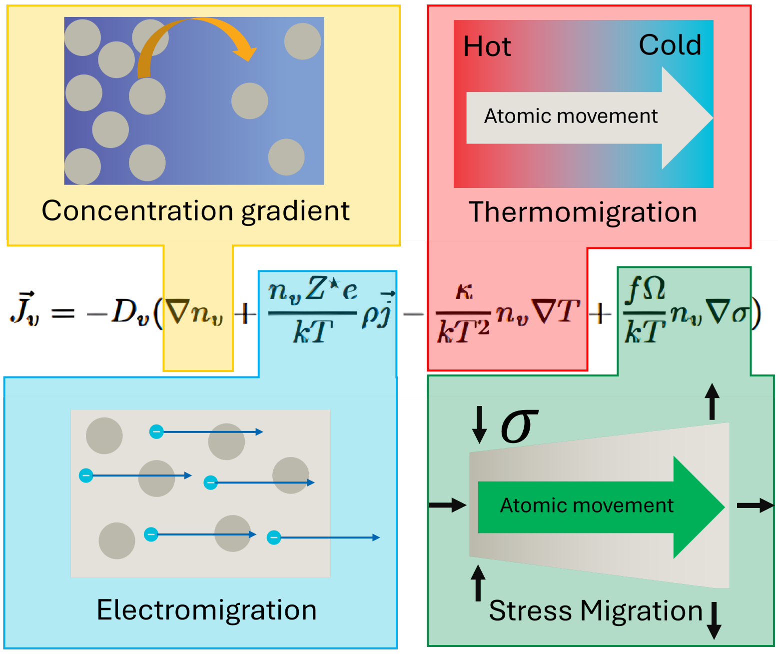

Figure 2.6: The general equation describing atomic migration includes contributions from concentration gradients (yellow box), electromigration (blue box), thermal effects (red box), and stress-induced migration (green box). A detailed treatment of this equation can be found in Joseph Lombardo's PhD thesis [70].

As this work focuses solely on electrical stress, only the term related to electromigration are discussed, even though other mechanisms must be considered to fully understand the atomic migration of matter induced by current flow. This atomic motion is rarely observed in macroscopic devices, as it requires high current densities. For instance, Black et al. observed electromigration under a current density of around $10^6\,\mathrm{A/cm^2}$ in aluminium [71] whereas Patil et al. observed apparition of voids in bulk silver at $10^4\,\mathrm{A/cm^2}$ [72]. Compared to a simple wire with a diameter of a few centimeters used to charge a computer[1], through which a current of 8.5 A is carried, the current density is around $2\,\mathrm{A/cm^2}$. Therefore, for electromigration to occur, either an extremely high current must be applied, or the conductor must be very small. This effect is typically observed

---

[1] These values were taken from this product page https://us.stockinthechannel.com/Product/Lenovo-GX20Z46287-power-adapter-inverter-Indoor-170-W-Black/54244379.

at the nanoscale, as such dimensions allow efficient heat dissipation. Consequently, high current densities (typically above 10^6 A/cm^2) can induce electromigration without melting the wire. This phenomenon is commonly observed in microelectronic devices [73]. Electromigration act continuously as long as current is applied. Thus, the study of duration of the applied current is indirectly implied when electromigration is taken into account. Therefore, it could be interesting to include the time parameters in the study of AgNWs instabilities.

Previous studies have examined how an AgNWs network can be affected when a constant current is applied over several weeks. Networks that are electrically affected tend to remain stable 3–4 weeks after a bias of 2 V (which corresponds to a temperature increase in the network of 30 °C or 60 °C, depending on the resistance of the network) [35]. However, several parameters (network density, applied bias) can be altered to trigger the process of degradation [74]. Curiously, these studies do not take electromigration into account as one of the processes that could trigger the increase in resistance related to network degradation. Therefore, several questions arise: *what current value triggers electromigration in AgNWs networks and break it in a relatively short time (under* 1 s*)?*

One can think that the density of current to trigger electromigration is AgNW is the same than the one found by Patil et al. However, the density current values observed, are obtained for materials in a polycrystalline state. Which means that the materials themselves contain defects that can either favour or hinder atomic migration when a current flows through the metal. Given that AgNWs are composed of five monocrystalline domains, it is reasonable to question whether electromigration occurs within a similar range of current densities.

Some answers to these questions are provided in an article written by Liu et al., who investigated the failure mechanisms AgNWs with hexagonal cross section (4H-AgNW) [75]. Although their results cannot be directly applied to the pentagonal-shaped nanowires studied here, they offer valuable insights into the parameter ranges necessary to observe electromigration. Liu et al. reported that a 4H-AgNW with a resistance of 402 Ω exhibited a critical current density (the current density at which the NW begins to deteriorate) of around 10^8 A/cm^2, a value consistent with those found in other studies on AgNW failure [6, 76]. This value differs from the current density reported by Patil et al. [72], highlighting the difference of AgNW behaviour with common bulk conducting material. Moreover, as Liu et al.'s study focused on a single NW, claiming that this current density represents a universal failure threshold, could be considered an exaggerated conclusion, since it can depend on additional parameters unrelated to the current alone (see Figure 2.6 mentioning thermal, concentration and stress coupling for atomic diffusion).

Another study investigated the impact of current on NWs made of a single crystal. This study was led by Stahlmecke et al. and typically shows the current density used for electromigration in nanostructured silver nanowire [77]. They used a current density of around 10^7 A/cm^2, in between the value observed by Patil et al. and Liu et al. This further indicates the range of currents that should be applied to a NW to trigger instabilities. Moreover, Stahlmecke et al. observed the localized nature of electromigration. Indeed, their NWs tended to induce instabilities near the cathode region (see Figure 2.7). This localisation effect might be related to $Z^\star$ previously discussed in Figure 2.6 [78]. It was also observed that the localization of instabilities across the entire network depends on the current density injected into the network [79]. Specifically, at a current densities (0.3 A/cm^2), instabilities tended to appear in the central region of the network, where the temperature is also higher compared to the edges. Conversely, when the current density decreased (below 0.2 A/cm^2), instabilities tended to appear near the anode region. In another survey studying instabilities of gold NWs Stahlmecke et al. observed the same behaviour (voids forming near the anode) [80] which is in opposition compared to their previous observation in AgNWs [77].

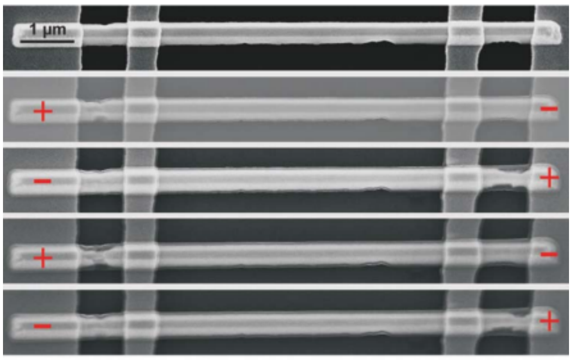

Figure 2.7: SEM images of silver nanowires produced by electron beam lithography, reproduced from the article by Stahlmecke et al. [77]. The NWs exhibit instabilities near the cathode region (indicated by the red plus symbol).

This discrepancy could stem from an aspect of electromigration that had been neglected in the previous model. Indeed, electromigration is often introduced through the 'wind force' (F_{wind}). However, this force should be understood as an effective one, primarily governed by the previously discussed mechanism 2.6. Nevertheless, a second force must be considered to fully describe the atomic diffusion. This additional force is related to the electric field, which tends to move the ions in the opposite direction, and it is called the 'direct force' (F_{direct}). Depending on whether one force predominates over the other, the atomic motion can be directed in the same direction as the current flow or in the completely opposite direction. Which explain why different materials can exhibit different behaviour leading to the formation of instabilities either at the cathode or the anode. However, it has been found that the situation where F_{direct} dominates F_{wind} is a very rare occurrence [69, 81–84]. On the other hand, these concept of effective force should be taken into account to gain a complete understanding of the electromigration process in nanostructures.

Since it is now established that electromigration occurs above certain values of current density, it would be interesting to explore the parameters that could affect this value. Indeed, as mentioned previously, this value depends on the crystal configuration. The crystal configuration is directly related to the symmetries exhibited by the wire within the lattice. These structural characteristics vary primarily depending on the synthesis method used for the nanowire. As observed, AgNWs with different crystal configurations can exhibit a maximum current density that varies by a factor of 10. Since, the focus of this work is on polyol-grown NWs (which have a particular pentagonal cross-section), determining the current density for these NWs would be particularly useful. Several studies have examined current densities leading to the breakdown of the network after several seconds, with values around 10^6 A/cm^2 [23, 33, 38, 85].

Based on these results, the logical next step is to study the maximum current density a single NW can withstand. This is precisely the focus of the article by Waliullah et al. [86]. Their results show that individual NWs fail at a current density of approximately 10^8 A/cm^2, consistent with previous measurements on various crystalline structures. Their study also highlights the stochastic nature of the maximum current density. They investigated 93 NWs with diameters ranging from 53 nm to 173 nm and found a mean failure current density of $9.7 \pm 3.0 \times 10^7$ A/cm^2. These findings suggest that the maximum current density does not vary significantly with different NW diameters. Consequently, based on these results, one can assume that the diameter of NWs in this work do not significantly affect the maximum critical current density. As different values of the maximum critical current density are mentioned in the literature, it would be interesting to compare the critical current density found in this work with those mentioned in this section.

It is worth noting that the previous results are obtained under direct current (DC) conditions, which represent only one method of current injection. Investigating the behaviour of AgNWs under alternating current (AC) could therefore provide valuable insights into the impact of electrical stress. From the perspective of electromigration, AgNWs are expected to be more stable under AC. Indeed, while DC induces a constant directional force on ions, promoting unidirectional migration and void formation, AC applies a periodically reversing force that limits net atomic motion, thereby reducing void formation. As a result, instabilities are expected to occur less frequently under AC conditions. This hypothesis was confirm by Wang et al. who measured the evolution of the network resistance under both AC and DC injection [79]. As anticipated, they concluded that NWs exhibit greater stability under AC stress than under DC stress. Therefore, methodologies aiming to study instabilities driven by electromigration would preferably employ direct current (DC) rather than alternating current (AC).

Moreover, electrical instabilities can trigger a cascading failure process. When a bias is applied to a network of AgNWs, the current distributes according to Ohm's law and the principles governing the combination of resistive elements in series and parallel. If a certain current density is sufficient to initiate electromigration and/or Joule heating, this may lead to the failure of an individual wire. In such a case, the current redistributes throughout the network and a percolating path may disappear, resulting in an overall increase in resistance.

Kholid et al. observed such a process in AgNWs networks [87]. They concluded that this avalanche effect is directly linked to the current threshold required to initiate the breakdown effect in the network. The main results from their study, summarized in the following key findings, are illustrated in Figure 2.8:

- In a dense network (with low resistance), the number of breakdowns is relatively low. However, as breakdowns occur, the resistance increases with each subsequent failure.
- As the network begins to deteriorate, the maximum current that can be sustained decreases, as fewer conductive paths are available within the percolating network.

This result should be taken into account during our experiments to address the issue of resistance increase observed throughout the experimental process (see Chapter 4).

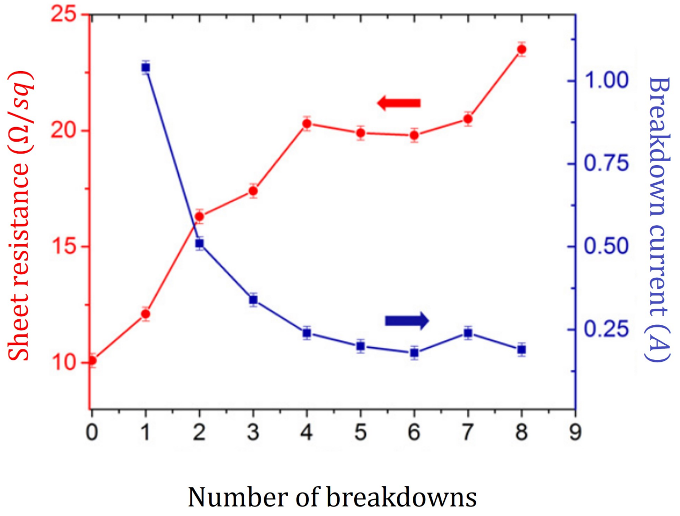

Figure 2.8: Graph reproduced from the article of Kholid et al. [87] that shows the evolution of the resistance and of the injected breakdown current in the network as a function of the number of breakdowns observed.

Current injection also contributes to enhancing the conductivity of the network. As previously discussed, it can induce instabilities which may trigger a sintering effect (see Figure 2.9). Similar to the approach used for thermal instabilities, researchers [87] have explored these electrical instabilities to improve the conductivity of a network. The aim is analogous to managing thermal stress:

identifying the right parameters that will enhance conductivity without causing network failure. They measured the maximum current density that could be applied to their network to ensure that electrical annealing would not degrade it. Then they performed cycles of current injection just below the maximum current density, with injection periods of 1 min and 3 min. Using this method, they successfully reduced the network's resistance by 18%.

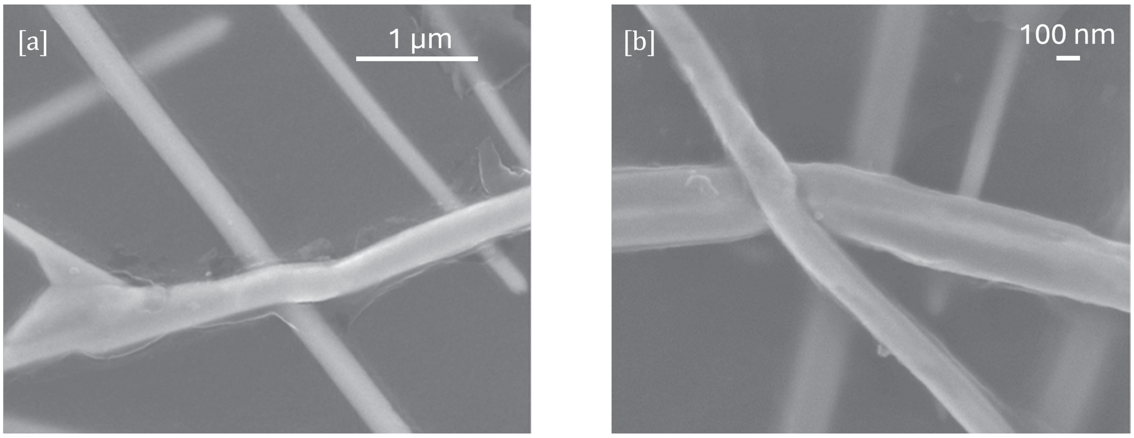

Figure 2.9: [a] [b] SEM images of a electrically annealed (using a current density of $50\,\mathrm{A/cm^2}$ for 5 min) AgNWs network reproduced from [87]. A sintering effect occurs here, merging the two wires together.

As seen during this section, Joule heating and electromigration are the two main features responsible for electrical instabilities. However, there is a phenomenon that was not taken into account in previous studies, which could theoretically occur in AgNW networks. The following section introduces the electrical breakdown effect and explains why it could potentially arise in the networks studied in this work.

2.2.4 Electrical breakdown

Due to the distribution of current within the network, different potential points appear. These varying potentials can induce currents outside the network, for instance in the surrounding air. Thus it becomes relevant to explore how environmental factors influence their behaviour. In particular, this section focuses on electrical breakdown, a phenomenon that may occur when a voltage is applied across the network. Introduction of the physical processes involved when a strong electric field is applied to a gas, such as air, is led in this section [88, 89]. Although gases are typically considered insulating materials, capable of impeding current flow under normal conditions, this insulating property is not absolute. Under specific conditions, even an insulator can permit current flow.

In this work, it is assumed that electrical breakdown can occur in an AgNWs network since two non-touching AgNWs can meet the conditions necessary to create a current through the surrounding air. More precisely, the condition to be met is given by Paschen's law [90]:

$$\frac{V_b}{d} = \frac{B \cdot p}{\ln\left(A \cdot p \cdot d\right) - \ln(\ln\left(1 + \frac{1}{\gamma_{se}}\right))}. \tag{2.3}$$

Here, d denotes the distance between the two electrodes, and V_b is the breakdown voltage (i.e., the voltage required to initiate electrical breakdown in the dielectric material). The parameter p represents the gas pressure, typically at atmospheric conditions. The constant γ_{se} reflects the ratio of electrons emitted by the electrodes to the number of ions generated in the gas. Lastly, A and B are gas-dependent empirical constants. When conditions are met electrical discharge occur which might lead to a sudden and extensive destruction of the network (these Pashen's law is also directly related to visual aspect of the electrical discharge discussed in Box 2).

Since, it is assumed that the distance between NWs is typically on the order of few micro/nano meters. It can be inferred that the network under study in this work can exhibit this type of phenomenon. This assumptions is based on an article that observed a huge deteriorated area due to an relatively high application of potential (around 20 V for network around 30 Ω) [36]. Thus, the outstanding question is: *could such a phenomenon appear in AgNWs network ?*

Box 2: Discharge in a gas

Gas discharge at high electric fields produces a current in a gas that is initially considered as an insulator. This phenomenon occurs due to the multiplication of electrons in the gas named electron avalanche (see Figure 2.10)[91]. However, the visual manifestation of this discharge depends on various parameters, such as the applied bias, the shape of the electrodes, and the surrounding environment. In this section, the most common types of gas discharge is discussed to distinguish them visually.

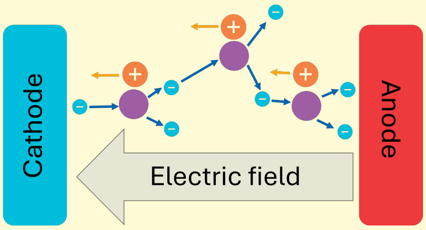

Figure 2.10: Schematic picture of avalanche process in a gas. Electrons are accelerated by the bias applied and collisions with an other atom will produced electrons that will be also accelerated: this is called the avalanche process.

- **Corona discharge**: since ions are created in the gas at high voltage, recombinations can occur, leading to photon emission. However, corona discharge does not generate electrons throughout the entire gas. As the electric field decreases with distance, electrons lose energy and eventually stop ionizing the gas, this limit is known as the edge of the corona. This phenomenon significantly increases the current compared to the insulating regime, as more electrons are now created through ionization (see Figure 2.11[a]).
- **Glow discharge**: the entire gas becomes a plasma, and it is no longer an insulating material. The potential drops drastically due to the presence of ions. Recombination occurs throughout the gas, causing the environment to glow (see Figure 2.11[b]).
- **Arc discharge**: since the plasma has formed, a huge current can flow through, producing light and heat. The potential drops even more drastically than in the glow discharge, and the current is significantly higher (see Figure 2.11[c]).

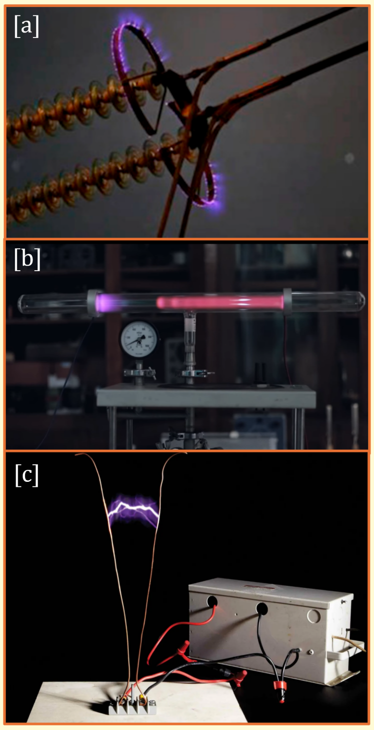

Figure 2.11: Experimental picture of the Corona discharge, glow discharge and arc discharge reproduced from [92–94]

2.2.5 Instabilities prediction

An overview of the instabilities occurring during current injection is provided in this chapter. However, these instabilities, resulting from current flow in networks, are often undesirable as it can lead to a breaking event (see Figure 2.8). Therefore, it is essential to explore ways to mitigate their impact. One potential approach involves predicting where these instabilities may arise. Thus, comparing such simulations with experimental treatments can help highlight phenomena such as electromigration and Joule heating, while also revealing aspects that have not yet been explored in the field of AgNW networks. This section provides a brief overview of the strategies that have been developed to address this issue.

As previously discussed, several studies have identified the general regions where instabilities occur (see Section 2.2). However, these regions are characterized post-current injection, which does not offer a predictive framework. A more effective way to tackle this issue is through simulation. The study of AgNWs has led to the emergence of various simulation methods. However, they are primarily used to analyse junction resistance or overall network resistance [60, 85, 95, 96]. Other studies have used COMSOL simulations to investigate the effects of coupled electrical and thermal stress on nanowires [38, 67, 97]. Additionally, simulations have been employed to understand the process of electrical annealing [95].

However, these simulations have not been employed to predict which NWs will exhibit instabilities. This raises the question of the feasibility of such a simulation, including the ability to predict network resistance, current distribution within the network, and potential instabilities. In addition, the reliability of instability localization should be assessed to evaluate the overall accuracy of the simulation. Therefore, to investigate this issue, the 'digital twin' methodology will be employed in this work to compare experimental and computational approaches applied to the AgNW network. This concept is well-known in the research community, even in fields outside of NW studies[98–100].

Methodology 3

This chapter provides the necessary background to understand the experimental tools and setups used in this work. AgNW networks have been specifically developed to tackle the key issues discussed in the last chapter. As a reminder, these questions are:

- What is the current density that causes NWs failure? Do our results validate the ones previously reported in the literature?
- What are the different phenomena that can generate failure in NWs networks?
- What are the limitations of predicting failure using the model introduce in section 3.2?

To attempt to answer these questions, simulations are performed to predict the localisation of the instabilities and the range of voltage that should be investigated. The actions undertaken are summarized below and illustrated in Figure 3.1 :

1. Produce and characterize AgNW networks via Scanning Electron Microscope (SEM).
2. Compute the voltage range to be applied and predict the zone prone to electrical failure.
3. Apply voltage pulses until complete failure, then characterize and compare to the predictions.

This approach can help identify potential unexplored instabilities and confirm or refute the presence of others discussed in Chapter 2. For instance, if the model predicts instabilities solely due to the current flowing through the network, and instabilities are observed both in the predicted areas and in other unexpected regions, one may infer that the current is not the only factor influencing the network under an applied bias voltage. Obviously, such conclusions can only be drawn if the predictive model is reliable. Therefore, a study of this model is necessary to draw conclusions about the emergence of additional, previously unaddressed instabilities in the AgNW network.

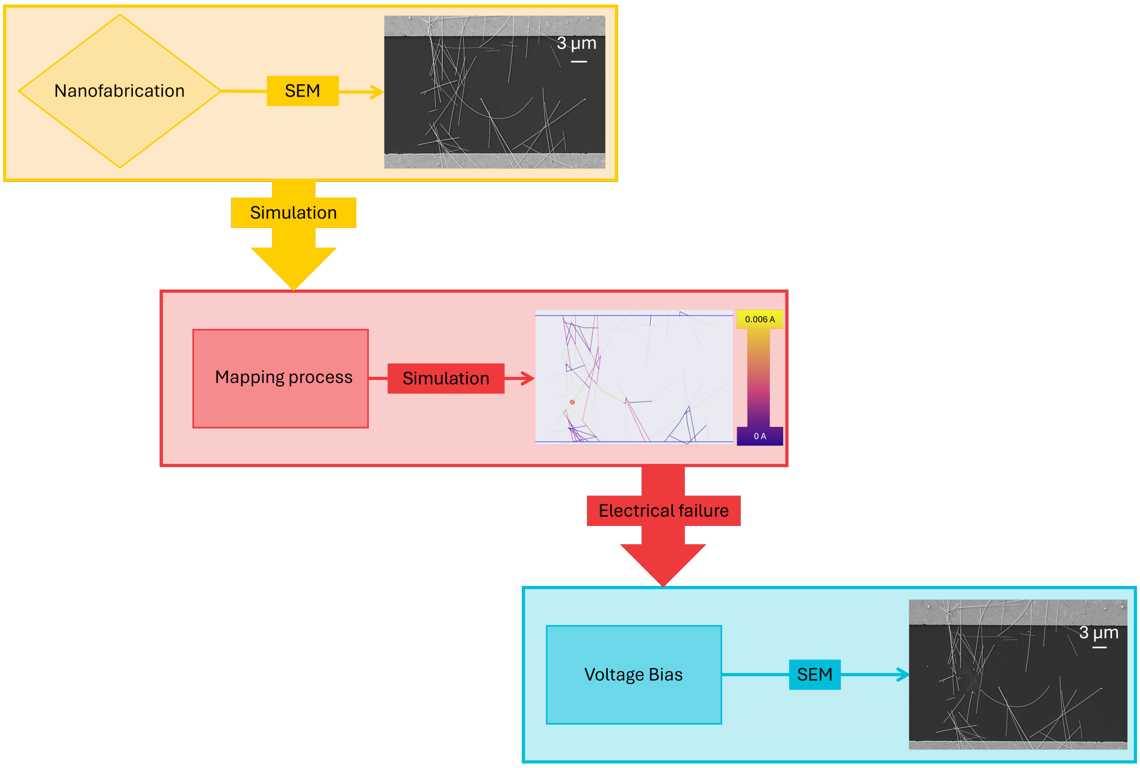

Figure 3.1: Flowchart of the methodology applied in this work. **Yellow box** is related to the samples' development (nanofabrication) and the characterization of these networks before the application of voltage (first SEM image). **Red box** is related to the simulation process, including the mapping and the simulation of the network. **Blue box** is the final step, which involves the application of voltage and comparison made both with the simulation and the image taken before voltage application.

This chapter is divided into two sections. Firstly, the experiment section (see Section 3.1) describes the experimental set to used in this work, including the instrumentation and how it is utilized to apply voltage and measure current. In addition, details on the fabrication process, including all the necessary steps involved in the sample preparation, are provided in Subsection 3.1.1 Secondly, a section dedicated to the simulation process (see Section 3.2) explains how the computational model operates.

3.1 Experiment

3.1.1 Sample fabrication

As the networks' characteristics are input parameters in simulations, both the experimental design and the network structure must be compatible and comply with the limitations of the simulation environment. Indeed, the simulation assumes that the networks will be subjected to a bias voltage (control variable under study) and the mapping process is done manually and can be very time-consuming when the number of wires to map is large (limit number of interconnected NWs). Moreover, considering only a dozen NWs in the simulation helps also to more accurately capture the physics behind the electrical failures observed in the SEM images. Therefore, the analysis carried out in this work can be seen as a **toy model**.

Therefore, networks containing only a small number of NWs are required (which favour both toy model approach and time needed for the mapping process). Obviously, having percolating network is also necessary to ensure current flow, which might introduces a conflicting requirement. Indeed, while fewer NWs favour the mapping process, this condition may prevent the formation of a percolating network. To satisfy these constraints, small-sized networks (on the order of a few micrometres) are prepared. This scale is comparable to the typical length of individual AgNWs, meaning that in some cases, a single nanowire may be enough to form a percolating path. To differentiate standard AgNWs samples and the specifically designed sample developed in this work they are referred to as *micro-networks*, in reference to their reduced physical dimensions. The following part of this section explains in detail the methodology for producing such micro-networks.

The fabrication process is divided into three main techniques that are used throughout this master thesis: **electron beam lithography** (EBL), **spin coating**, and **physical vapour deposition** (PVD). The networks can be obtained through the use of a mask. This mask is created by patterning a spin-coated material using EBL. Then, NWs are deposited to form the networks. Finally, another mask is used to define the electrodes required for applying a bias voltage to the network. The holes in the mask are filled using a PVD method, which creates the necessary electrodes. The details of the fabrication process are developed through this Chapter.

Electron Beam Lithography (EBL): managing to create a microscopic pattern is a real challenge in terms of fabrication. Therefore, tools that could lead to create those objects is crucial. Precisely, elaboration of a pattern thanks to a mask creation is essential in this project. Masks help mainly with the development of part of the sample at a small scale. This mask is most of the time removed afterwards and helps only to deposit the part needed for the sample. In this work, it allows for control over the size and shape of the fabricated parts of the sample [101], such as the electrodes development and networks. This mask patterned via the EBL technique.

EBL helps to pattern material and therefore, as mentioned, obtain the required mask (see Figure 3.2 [a]). Indeed, the electron beam writes the pattern onto a substrate called resist, which leads to the formation of the mask after removing the non-desirable part mentioned earlier. Resists are materials used to define patterns on a substrate, they are obviously convenient in the mask fabrication process. Two main types of resist can be employed: positive and negative. In this work, only positive resist is used. In a positive resist, the regions exposed to the electron beam become soluble. After exposure, the sample undergoes a step known as **development**, in which the soluble regions of the resist are removed using a chemical solution, which reveals the required pattern. After the mask has been used, it can be removed by applying isopropanol to it. This process is called **lift-off**. In this work, polymethyl methacrylate (PMMA) and copolymethyl methacrylate (Co-PMMA) are used as resists for EBL. They are both polymers that degrade upon exposure to an electron beam. Indeed, the incident electrons induce a reduction in molecular weight and an increase in solubility of the exposed regions, these properties are essential for the development of the mask. The primary distinction between PMMA and Co-PMMA concerns the degree to which they interact with the electron beam when subjected to identical exposure conditions (beam energy and diameter). When used in a bilayer configuration, Co-PMMA is more sensitive and therefore exhibit a large interaction volume with the electron flux compared to PMMA [102]. This characteristic is particularly convenient (see Box 3) for the development of the masks required in this project.

Spin coating: depositing a uniform thin layer of solution is a common step in device fabrication, and several techniques can be used to achieve this. Spin coating is one of the most commonly used methods to deposit a thin layer of material onto the surface of a substrate [103, 104]. In this method, a droplet of the desired solution is placed on a rotating substrate (see Figure 3.2 [b]). Due to the centrifugal effect generated during spinning, the liquid spreads evenly across the surface, resulting in a thin (around several micrometers of thickness [105]), homogeneous film. The final thickness of the deposited layer mainly depends on the angular velocity of the spinning process as well as properties related to the solution, such as viscosity. However, viscosity cannot be significantly altered by the method as it depends on the solution utilized. Following the deposition, the sample is typically heated on a hot plate to evaporate any residual solvent, leaving a uniform solid layer. In this project, spin coating will be employed to deposit both resist layers (PMMA and Co-PMMA) and the AgNWs.

Physical Vapour Deposition (PVD): PVD is based on physical phenomena, as opposed to Chemical Vapor Deposition (CVD) [106], which relies on chemical reactions. PVD encompasses many techniques [107] including Thermal Vacuum Evaporation (TVE), which is used in this work. The goal of this technique is to deposit a controlled amount of material onto a substrate [108]. In the TVE process, a pellet of the desired material is placed on a resistively heated support. When heated, the pellet undergoes thermal evaporation, releasing releasing atoms of the material into the chamber (see Figure 3.2 [c]). Atoms move freely in the vacuum environment and are deposited onto the surface of a substrate positioned above the pellet, forming a solid film. The thickness of the deposited layer can be controlled by adjusting the quantity of pellets in the resistive crucible. Importantly, the entire process must be carried out under vacuum conditions (9×10^{-6} mbar) to prevent contamination from residual particles present in the environment.

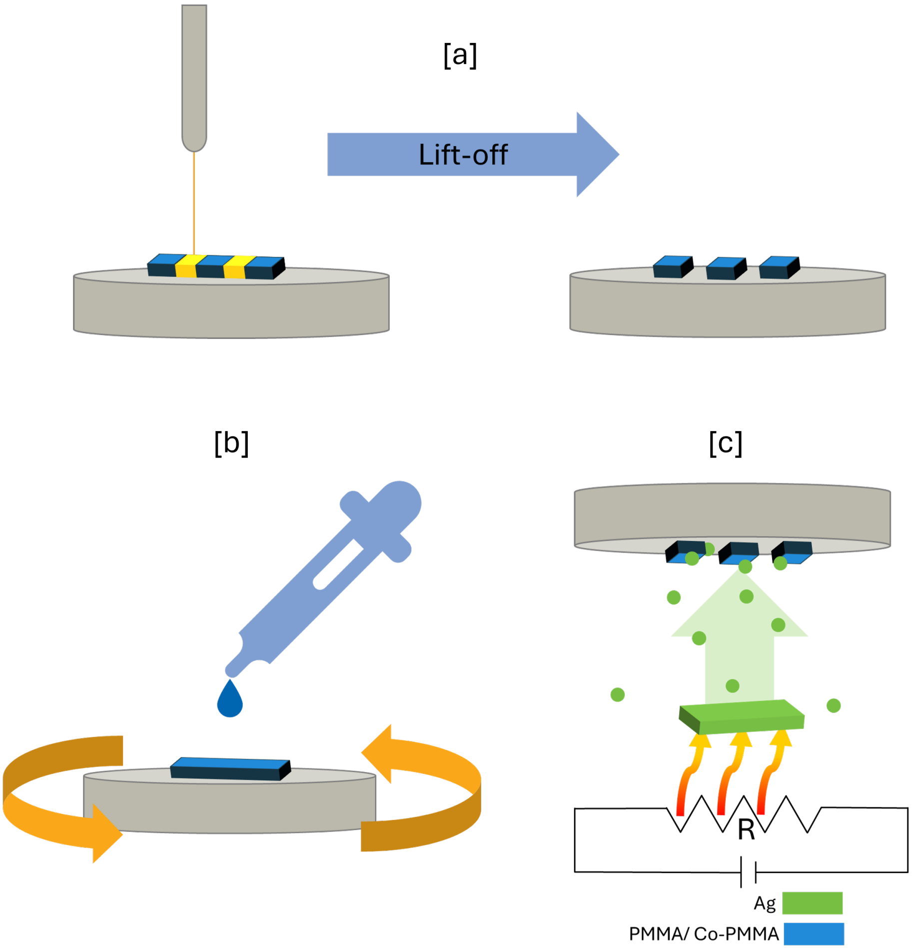

Figure 3.2: [a] Schematic drawing of a sample exposed to an electron beam (left sketch). After development, the non-exposed region remains (right sketch). [b] Schematic illustration of the spin-coating process. A liquid is deposited using a pipette while the substrate holding the sample rotates. [c] Schematic illustration of the TVE process. Heat is generated by Joule heating through a resistive element. The sample is placed above (shown in blue, representing the mask used for atom deposition), where atoms will coat the sample thanks to the global emanation of atoms coming from the solid source (shown in green).

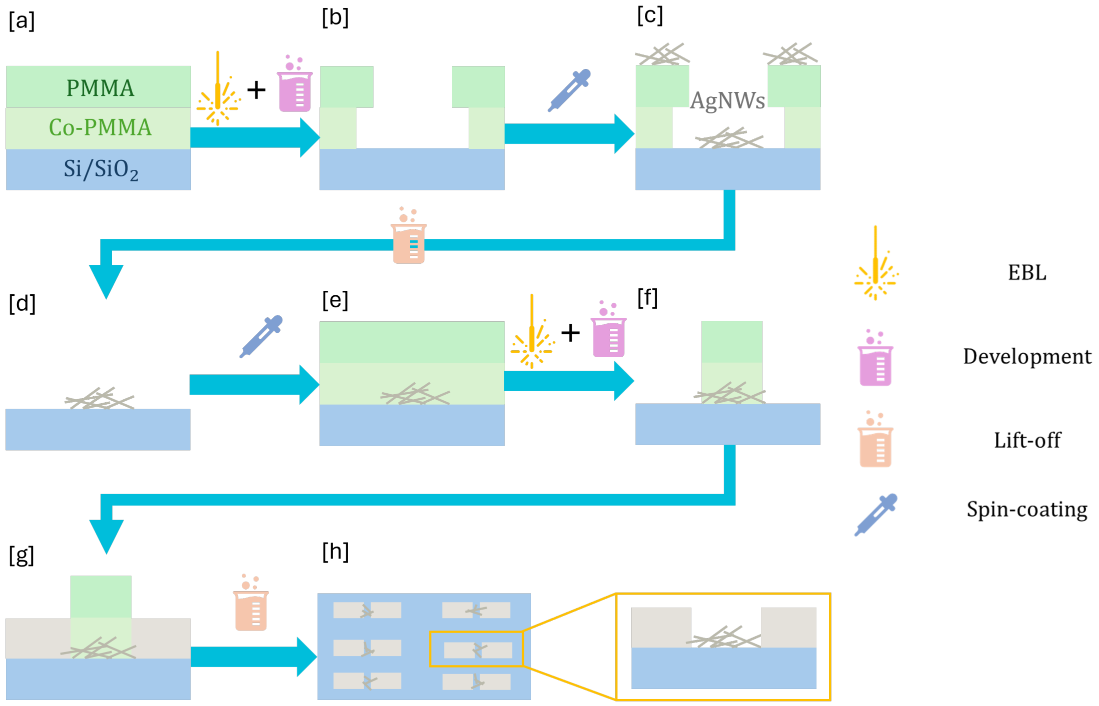

Figure 3.3: Schematic illustration of all the steps required to obtain the micro-networks. [a] Spin-coating is performed twice to deposit one layer of Co-PMMA and one layer of PMMA onto the Si/SiO$_2$ substrate. [b] After EBL (represented by the yellow ray) and the development (represented by the purplish beaker), both layers are patterned, and the mask is obtained. [c] Spin-coating (represented by the blue pipette) of Ag NWs is performed on the mask, which is then removed by lift-off (represented by the salmon-coloured beaker), leaving only the deposited NWs on the substrate [d]. [e] Another spin-coating step is performed to create the top layer that defines the electrode area. [g] PVD is used to deposit silver for the electrodes. [h] After the final lift-off, the sample remains with the networks and the electrodes located at the edges of the micro-network.

Figure 3.3 summarizes all the steps performed to manufacture the samples. Initially, a silicon wafer coated with a layer of insulating SiO$_2$ was used to support the fabrication of the mask required for the AgNW micro-network deposition. Subsequently, a bilayer of PMMA and Co-PMMA is deposited onto the substrate using spin-coating in order to define the mask via EBL (see Figure 3.3 [a]). The reason for using two distinct resist layers in this process is discussed in Box 3.

Box 3: Why using PMMA and Co-PMMA ?

Using two different resist layers is convenient to obtain precision lithography. To illustrate this concept, consider the following thought experiment. Suppose only a single resist layer is deposited onto the sample. After performing EBL and developing the resist, the resulting mask consists of a uniform layer with just one hole in it (see Figure 3.4). This layer will be in direct contact with the AgNW network that is subsequently deposited by spin-coating. During the lift-off process, the edges of the resist may take parts of the network with the mask. Therefore, the remaining part of the network does not have the required dimensions for the work.

To overcome this issue, a second resist layer (more receptive to electron beam exposure) is employed. This results in a bi-layer mask with an undercut profile: the top layer presents a narrow aperture that defines the geometry of the network, while the bottom layer exhibits a wider opening (used as a support for the real mask). This configuration prevents the nanowires from adhering to the sidewalls of the mask. Consequently, during lift-off, the AgNW network remains intact, and micro-networks have the correct dimension (see Figure 3.4).

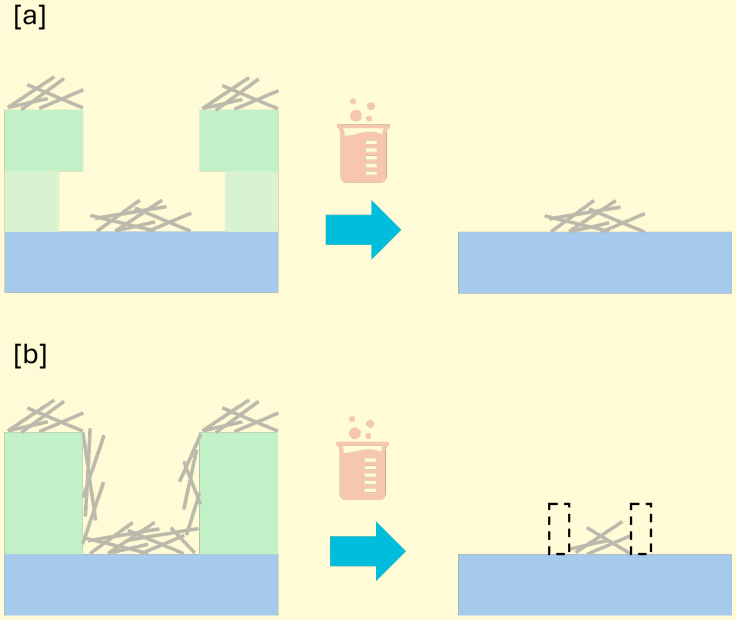

Figure 3.4: Schematic illustration of the two contrasting situations. [a] Process for mask development with bi-layer configuration. [b] Process for mask development with a single layer, resulting in the absence of several NWs after deposition (dotted boxes following the lift-off show that some NWs are absent compare to the bi-layer configuration).

The goal is to pattern the network in these two resist layers using the EBL method (yellow icons in Figure 3.3). The pattern is drawn by the electron beam, and the undesired parts of the mask are removed through development with methylisobutylketone (MIBK), which eliminates the exposed areas (represented by the purplish beaker in Figure 3.3 [b]). The next step is to deposit the NWs onto the mask. Spin-coating is again used to deposit the NWs into the patterned region (see Figure 3.3 [c]). The mask is removed afterwards using isopropanol (represented by the salmon-coloured beaker in Figure 3.3 [f]). AgNWs networks (deposited on the substrate) are thus obtained (see Figure 3.3 [d]). To add electrodes, another spin-coating step is performed to deposit PMMA and Co-PMMA, which is used to pattern the mask for the electrodes (see Figure 3.3[e]). Next, an overlay is created via EBL onto the network to pattern the holes that generate the electrodes (see

Figure 3.3 [f]). The electrodes are then deposited via PVD from a silver solid source. Evaporated silver atoms fill the holes opened by EBL, leading to the formation of two electrodes that are in contact with the network, owing to the previously created overlay (see Figure 3.3 [g]). Finally, a lift-off process is performed to remove the non-desirable resist layer. The result of these steps is a piece of wafer with several micro-networks (see Figure 3.3 [h] and 3.5).

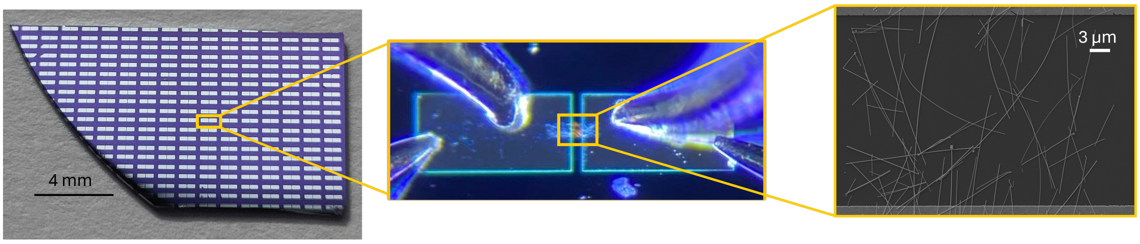

Figure 3.5: [a] Wafer after the complete fabrication process. Each micro-network is comprised between two rectangular-shaped electrodes. [b] A micro-network can be seen while a bias voltage is being applied via the metallic probes (see subsection 3.1.2 for more information about the application of the voltage). [c] SEM image of the networks.

All the micro-networks presented in this work are produced using this technique, with the same steps and parameters, resulting in similar networks even on different pieces of wafer. However, differences in density can be observed due to the non-homogeneous distribution of the AgNWs during spin-coating. As a result, the resistance of the micro-networks may vary, occasionally by an order of magnitude, depending on the specific micro-network studied in the experimental treatment. This discrepancy across the networks may also be attributed to the radial distribution observed when nanowires are spin-coated [109].

3.1.2 Experimental protocol

This subsection is dedicated to the description of the operating procedure for voltage application. Specifically, it explains the steps performed on the micro-network in order to characterizes each of them via imaging or via the measurement.

Beforehand, SEM images of the micro-networks are acquired. A program is then created to map these NWs. Basically, by clicking on the ends of the NWs, information on the length, the angle, and the position of the NWs centre is saved to insert it as an input in the simulation (see Figure 3.6). The subsequent step involves simulating all networks to extract three essential pieces of information: the localization of the wires that will undergo a breaking event, the voltage range required to break the entire network, as well as the pulse increment to limit the experiment time to 30 s. Indeed, the networks will be subjected to a sequence of increasing pulses; therefore, choosing the right increment is crucial to optimize the time of the experiment. This aspect of the input parameters is discussed later on in subsection 3.2

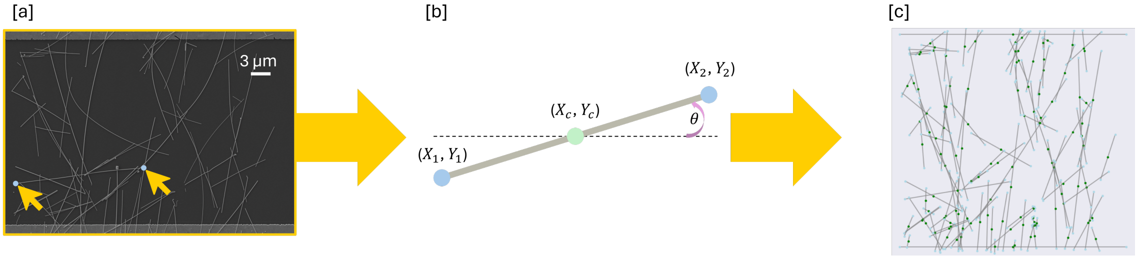

Figure 3.6: Picture illustrating the network mapping process. [a] A network on the sample is selected and imaged using SEM. [b] The data related to the position of a wire is saved (X_1, X_2, X_c, Y_1 ,Y_2, Y_c and θ). [c] Shows schematically what is stored overall during the mapping process of a micro-network.

Once the voltage range to be applied is determined by the simulation, the networks can undergo a series of voltage pulses (also determined by the simulation process). A four-probe measurement is carried out using a Keithley 2450 source meter. In this setup, two probes are used to apply the bias voltage, while the current flowing through the network is measured trough the other two probes (see Figure 3.7).

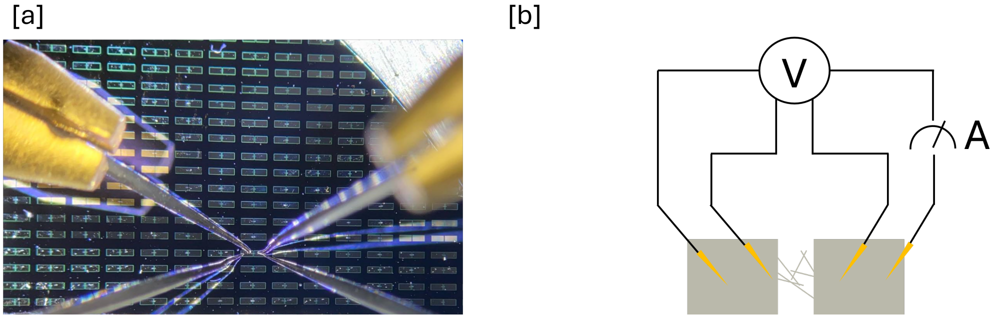

Figure 3.7: [a] Experimental four-probe set-up during electrical measurement. Connection with the electrodes is made through to the probes in contact with the two electrodes. [b] Schematic picture of the four-probe set-up [110].

As briefly mentioned, the full experimental setup involves more than merely applying a bias voltage and measuring the resulting current. Each network is subjected to a sequence of voltage pulses (0.1 s) with brief pauses between pulses (typically 9 s) to allow thermal relaxation and to ensure dissipation of heat generated by Joule heating [111], as is the case in this work, the focus is on the impact of electrical stress. At each step, the amplitude of the pulses is progressively increased, following the increment pulse found by the code (see Figure 3.8) in order to reach the current threshold that may lead to the breaking of individual nanowires and subsequently the entire network.

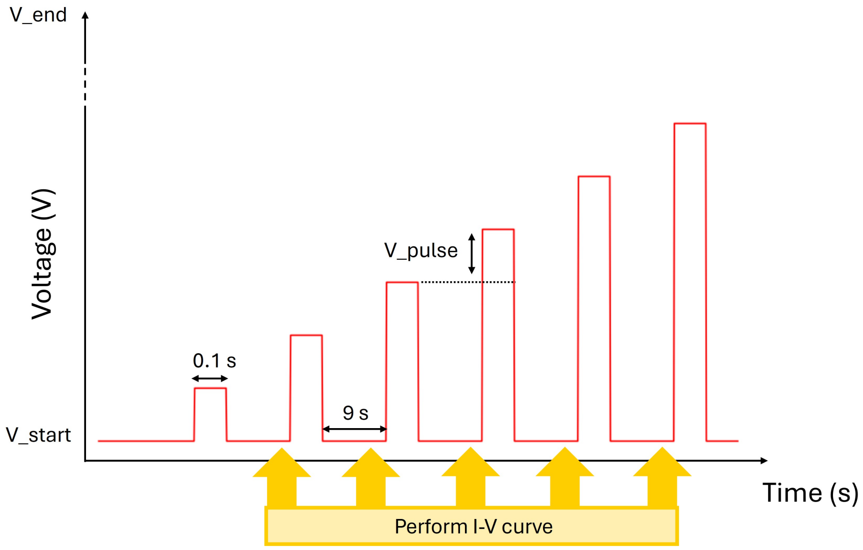

Figure 3.8: Pulse pattern used for the experiment. The voltage pulse starts at V_{start} (previously obtained via the simulation), and the pulses increase with an increment of V_{pulse} until either the network breaks or the pulse reaches the value of V_{end} (also obtained via the simulation). Each pulse lasts 0.1 s, and the delay between successive pulses is set to 9 s.

After each voltage pulse, an I–V (current–voltage) curve is recorded to determine the resistance of the micro-network. It is important to note that this measurement is conducted using a different four-probe configuration: the current is injected while the voltage is measured (this configuration is the opposite compared to the voltage pulse one). This setup ensures better control over the injected current and thus prevents alteration of the micro-network's structure during the measurement due to electromigration. As a result, the I-V curve is obtained using a range of currents between -10^{-6} A and 10^{-6} A, this preventing electromigration during the measurement process. Indeed, assuming the worst-case scenario where the entire current flows through a single NW, the resulting current density would be of the order of $\frac{10^{-6}}{10^{-5}\times10^{-5}} = 10^4$ A/cm^2 (considering wire dimensions on the order of 100 nm). This value is two orders of magnitude lower than the current densities reported in Subsection 2.2.3, suggesting that the formation of instabilities during resistance measurements can be avoided.

The resulting resistance is registered as well as the voltage pulses, allowing access directly to the evolution of the network resistance. This evolution will serve as a criterion in the subsequent section. Observing how the resistance varies with increasing voltage pulses allows for determining whether the network is starting to degrade (indicated by an increase in overall resistance) or whether the current conduction is improving (reflected by a decrease in overall resistance). Typically, voltage pulse applications are stopped when the resistance increases drastically (the resistance of the network exceeds $10^6\,\Omega$).

Subsequently, the network is imaged using SEM to compare the pristine network with the same network after it has undergone degradation due to voltage application. Finally, the simulation results are compared to both the experimental measurements and the visual observations to address the questions raised earlier in the study.

3.2 Simulation

This section discusses the simulation process. As mentioned earlier, the goal for the simulation code is to provide the voltage range that should be applied to the network to break the micro-networks as well as the broken wires' localization.

Firstly, the code considers the wires previously generated from a SEM image via the mapping process (see Subsection 3.1.2). Electrodes are placed at the edges of the network, as in the experiment, and a random bias voltage is applied to the network to find the first wire to break in the network. Following the basic principles of electrical circuits including Kirchhoff's laws, the code solves the electrical circuit that represents the network to calculate the current flowing through each wire when bias voltage is applied. This result stems from the fact that each NW can be seen as a resistive element, and the entire networks can be paired to an electrical circuit composed of a series of resistances placed in parallel and/or in series. The code uses an approach based on Modified Nodal Analysis (MNA) to compute the distribution of current in network, which consists of the elaboration of a matrix containing the information on the topography of the network (localisation of the potential, resistance in play, and voltage applied) and is also based on Kirchoff's current law. Commercial softwares have also implemented this approach to compute the current distribution in electrical circuits, such as *QUCS* [112] or *SPICE* [113]. Therefore, the code establishes a matrix equation based on MNA and solves it numerically to find the current flowing in the entire network. By knowing the resistance of each element in the network (obtained directly from Pouillet's law), the potential applied at the node in the circuit, and the current flowing in the entire network, every current flowing in a resistive element can be obtained.

Specifically, this current may reach a value where instabilities such as electromigration may occur. By solving the matrix equation, the wire that exhibits the largest current can be found. If the maximum current[1] that a wire can undergo is known, the opposite process can lead to the voltage value. This value corresponds to the potential that exhibits the maximum current in the wire that undergoes the largest current. Subsequently, the wire segment that undergoes this current to this new value of voltage is removed by the code, and thus, the current flowing in each

---

[1] Currently, this value is yet to be determined. However, a part of this section is directly dedicated to the research of this breakdown current (see Figure 3.11 for instance).

wire is recomputed, which may cause other wires to break at a different voltage. This process of finding the wire that will undergo the largest current and assessing the voltage corresponding to this situation continues until the network becomes disconnected, i.e. the network becomes non-percolating.

With this procedure the code is currently able to predict where the wire will break (see Figure 3.9) and at which voltage it should appear.

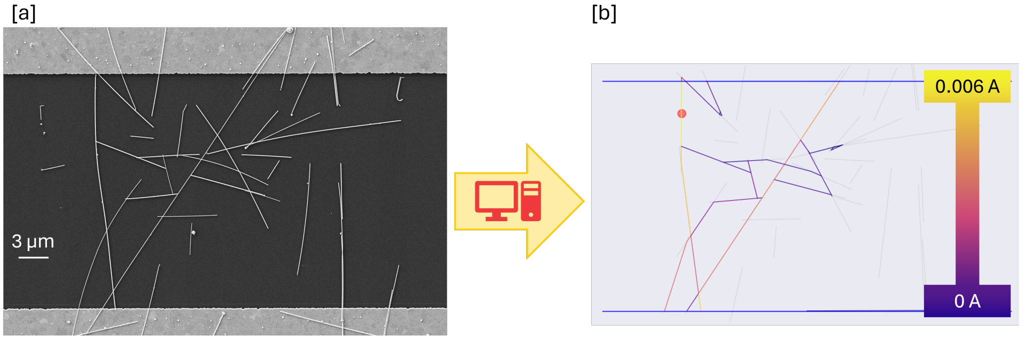

Figure 3.9: Picture of the simulation process. [a] SEM image of the network. [b] Spatial distribution of the current in the network predicted by the simulation.

It should be noted that the junction resistance is considered as an input in the code, which means that it can be tuned to directly impact the resistance of the simulated network. This value of the junction resistance is first chosen by fitting the resistance computed by the code with the resistance measured experimentally on dozens of networks (these networks are not used as data in the result section). Moreover, several assumptions are made for the numerical treatment, which need to be introduced. Therefore, in the results and discussion section, these assumptions must be considered in order to understand the overall behaviour of the network when a current flows through the system. These assumptions are listed below.

- **Each NW in the simulation has the same diameter**: Balty et al. [22] observed that the diameter of the wires coming from a solution, named after the diameter of the wire contained in the solution, actually follows a Gaussian-like distribution centred on the desired value of diameter (see Figure 3.10).

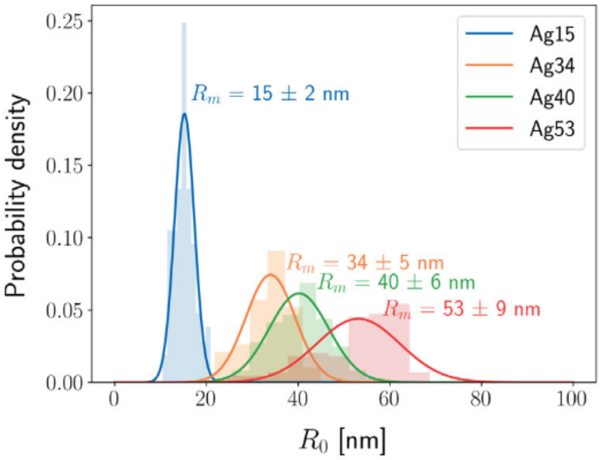

Figure 3.10: Reproduction from the article of Balty et al. [22], showing the distribution of the NWs' radius for a given solution. In this work, NWs with a radius of 40 nm are used, which corresponds to the green distribution.

- If the threshold current is reached in a wire, **the part of the wire that reaches this current is removed**. As mentioned in Section 2.2.3 a certain current value can trigger the electromigration. Therefore, it is assumed that for a certain value of current, the wire breaks due to this current. Moreover, following the results listed in Section 2.2.3, the diameter of the wire does not drastically affect the maximum current that a wire can undergo (always on the order of 10^7 A/cm^2). Therefore, it can be assumed that the maximum current that a wire can undergo is similar for every wire.
- **The junction resistance remains constant during the simulation and has a fixed value**. As mentioned in Section 2.2.1, junction resistance is currently not completely understood. For instance, the evolution of this resistance as a function of the applied voltage is still unknown. Thus, as a first approximation, this value is assumed to be constant for the simulation.

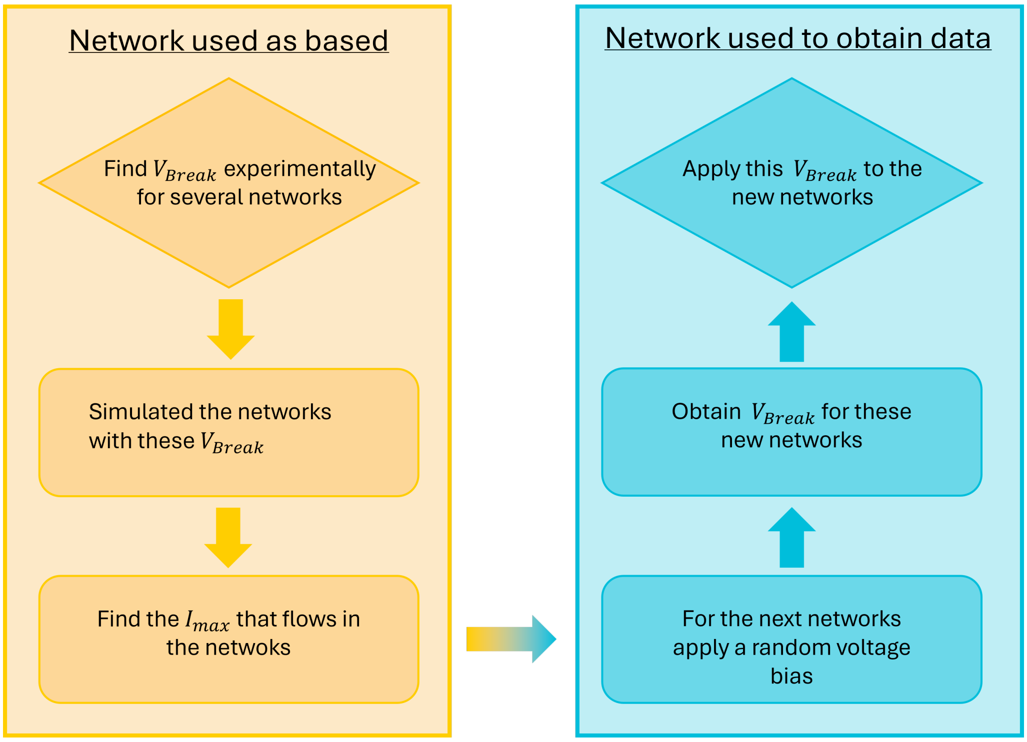

Figure 3.11: Flowchart illustrating the process developed to find the approximated V_{break} for the networks. **Yellow box** includes all the steps performed with the network that were used as a basis to find V_{break}. **Blue box** includes all the steps performed with the networks used to obtain all the data treated in Chapter 4.

To predict the voltage range that should be investigated to observe instabilities, initial measurements must be conducted to evaluate the current that causes wire breakdown. Therefore, voltage application is performed to break networks in order to identify the voltage that causes wire failure within the network. Then, these networks are simulated using the same voltage range to determine the maximum current that a wire can withstand under these conditions in the simulation. This current value is used as a basis for prediction[2]. In other words, once the specific voltage corresponding to this current value is found, it can be inferred that experimentally, in the vicinity of this voltage, the network will also break. This whole process is schematically explained in Figure 3.11. To sum up, the only information needed to obtain the voltage range is the topology of the networks and the value of the current obtained by simulating the broken networks with the voltage

---

[2] Similarly to what was done with the junction resistance, here the value of current used for the simulation is based on dozens of networks broken due to voltage application. These networks are not used as data for the results section.

that generates this breaking event experimentally. Thus, by solving the matrix equation previously introduced, the voltage that will experimentally break the wire can be directly obtained.

As the estimated voltage provides only an approximation of the voltage that should be applied to destroy the network, the experiment instead assumes a range of voltages based on the value obtained via the code. Specifically, the upper limit for the voltage pulse is set to 110% of $V_{break}(V_{max})$, while the lower limit is set to 10% of V_{break} (V_{min}) to ensure the experimental breakdown. Given that the pulse range is predefined (with V_{min} and V_{max}), and that the time interval between two pulses is measured (around 25 s), the appropriate value of V_{step} ensuring a 30 min experiment duration could be directly determined. Practically, a text file is generated and used as an input for the experiment. It contains the name of the micro-network, and the values of V_{min}, V_{max}, and V_{step}. The voltage range is adjusted in some extreme cases where the predefined values do not lead to network breakdown during the experiment.

Some features, listed here below, are ignored by the model. These limitations must be taken into account in the discussion reported in Chapter 4.

- The code does not account for the distribution of wire diameters observed in the network. As previously mentioned, it assumes a uniform diameter for all wires.
- The evolution of resistance resulting from potential improvements at the junctions is not considered. This constitutes a significant approximation, justified by the limited information available on the subject.
- Defects in nanowires are not considered. This represents a strong assumption, as it is reasonable to believe that defective nanowires are more susceptible to the onset of instabilities [114].
- The heat generated during voltage application is not accounted for in the code, implying that the flowing current is the sole parameter capable of inducing instabilities.
- The code models the network as a two-dimensional system. While this approach is generally valid, it may introduce discrepancies with the actual three-dimensional structure of the network (this aspect is discussed in the following Chapter 4).
- The connection to the electrodes is assumed to be ideal, introducing no resistance into the network. In other words, the contact resistance between a wire and an electrode is considered negligible.

Results and discussion 4

This section presents the results obtained using the methodology introduced in Chapter 3. The main objective is to compare the experimental data with the model used to analyse micro-networks. To this end, various aspects of the simulations are discussed, along with the general behaviour of AgNW networks. Differences and similarities are highlighted to provide insights into the code used in this work.

As a brief reminder, the recorded data are listed below:

- Images of the (micro) AgNW network before and after the application of voltage bias;
- Electrical measurements recorded during voltage application (including resistance, voltage pulses, and current pulses);
- Key simulation-derived parameters, such as the voltage threshold for network failure and the network's resistance.

These data allow one to answer the questions previously raised in Chapter 2. This chapter is separated into three parts. First, Section 4.1 is dedicated to a comparative study of the network before and after electrical failure. Second, Section 4.2 is devoted to the analysis of the electrical measurements, mainly focusing on the evolution of resistance. Finally, Section 4.3 presents a discussion of the model used for the simulation, highlighting what the code can currently achieve and what it still lacks as well as a discussion on morphological instabilities to introduce well-known concepts and explore new perspectives.

4.1 Morphological characterization of the failures

Before delving into the main subject, let us consider what might happen when voltage is applied to the networks. This discussion helps to distinguish already known instabilities from hypothetical ones, discussed in Box 2. As discussed in Chapter 2, three main processes could lead to network deterioration such as electromigration, Joule effect and electrical breakdown. Figure 4.2 illustrates that, depending on the instability, the resulting morphological change can exhibit either a localized (such as in electromigration) or large area effect (like in electrical breakdown[1]). In this chapter, the term *multiple breakdown* is introduced to describe instabilities involving more than one NW such as the one that might happen if electrical breakdown occurs.

---

[1] which is still an assumptions here since no evidence of electrical breakdown in AgNW has been reported so far.

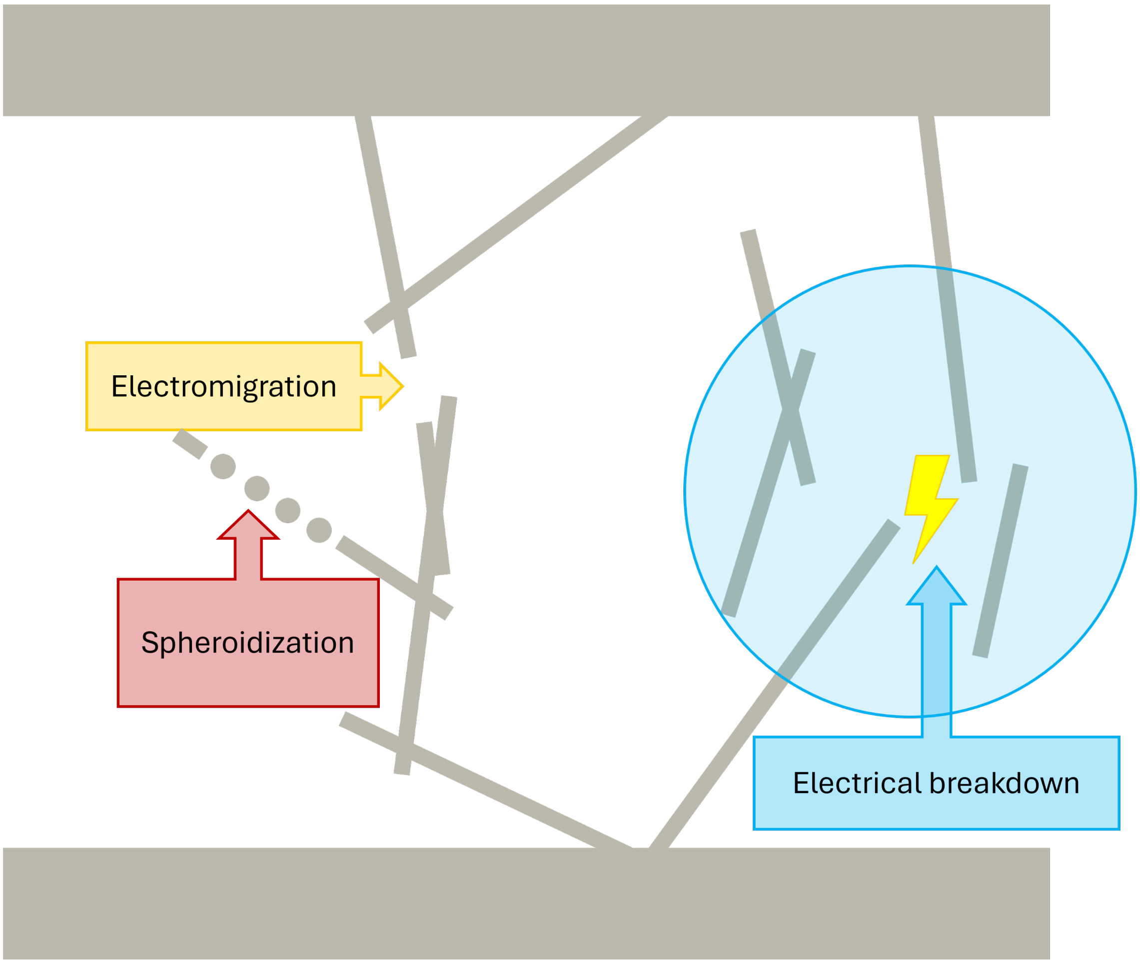

Figure 4.1: Schematic drawing summarizing the three main instabilities expected to occur during voltage application including electromigration, spheroidization and electrical breakdown.

Even though electrical breakdown remains a hypothesis, this idea is supported by an observation made during tests on the networks [2]. Indeed, following the application of a potential, some nanowires that are not part of the percolating cluster exhibited signs of instability. The underlying assumption is that two wires, one belonging to the percolating cluster and the other merely connected to the electrode, experience a sufficient potential difference to generate a current through the surrounding air.

---

[2] These networks are not taken into account in the data analysis, as the methodology applied to them had not yet been well established at that stage.

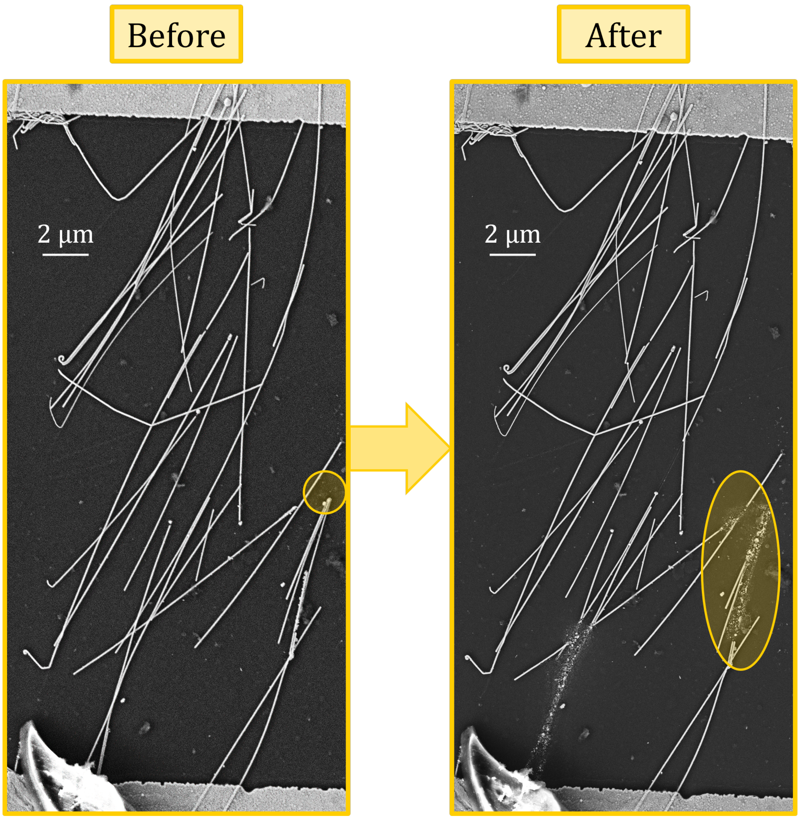

Figure 4.2: SEM images acquired before and after the electrical failure reveal that nanowires not involved in the percolating cluster also experienced damage, highlighting a potential electrical breakdown.

Time is also a crucial parameter when discussing instabilities. While electromigration occurs suddenly once current threshold is reached, spheroidization is a more gradual processes. Both instabilities involve atomic migration, which leads to the destabilization of the NW and to a local shrinking [22, 77]. These different aspects of instabilities must be taken into account in this section to provide insight into what may occur when voltage is applied to micro-networks.

Firstly, to investigate the instabilities shown in Figure 4.2, simple networks, consisting of a single NW, are considered. These elementary cases provide insight into the electrical failure that may occur when current flows through an isolated wire. In this context, the influence of other NWs is neglected, as the nanowire alone forms the micro-network. Consequently, these cases do not address multiple breakdowns but rather focus on failure mechanisms in a single segment (see Figure 4.3).

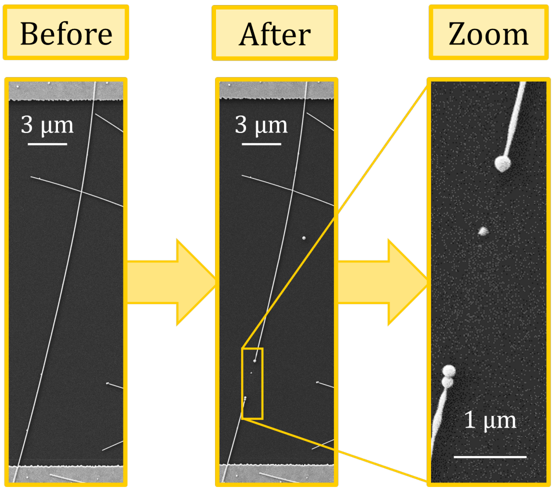

Figure 4.3: Micro-network composed of a single nanowire before and after. Other nanowires visible in the image are not part of the percolating cluster and were therefore cropped out to highlight the nanowire forming the micro-network. The instability in a wire segment does not affect the surrounding nanowires.

Furthermore, this single segment instability is also observed in networks containing more than one nanowire in the percolating cluster (see Figure 4.4).

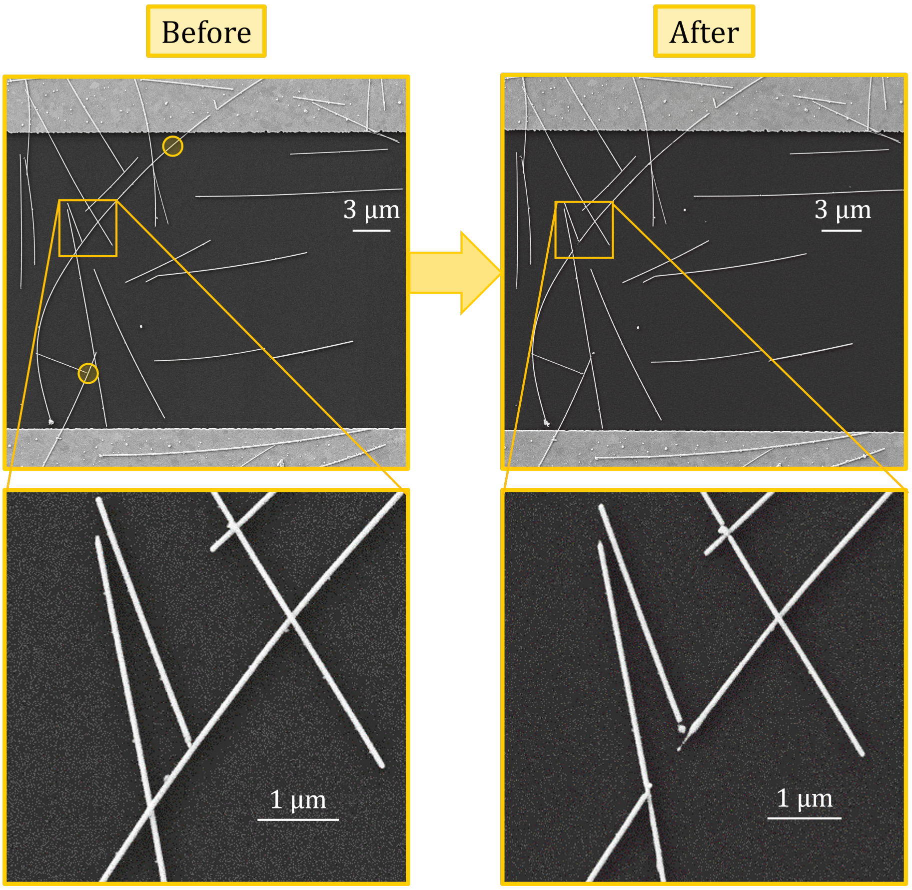

Figure 4.4: Micro-network composed of more than one NW. It can be seen that the instabilities are localised and does not affect other wires. Zoom is performed on the wire that exhibited instabilities.

These two examples suggest that AgNW networks can undergo instabilities in a single wire, possibly due to electromigration. Besides, other types of deterioration are observed during image analysis. These events include multiple breakdowns while the deterioration may also affect a large area of the network (see Figures 4.5 and 4.6).

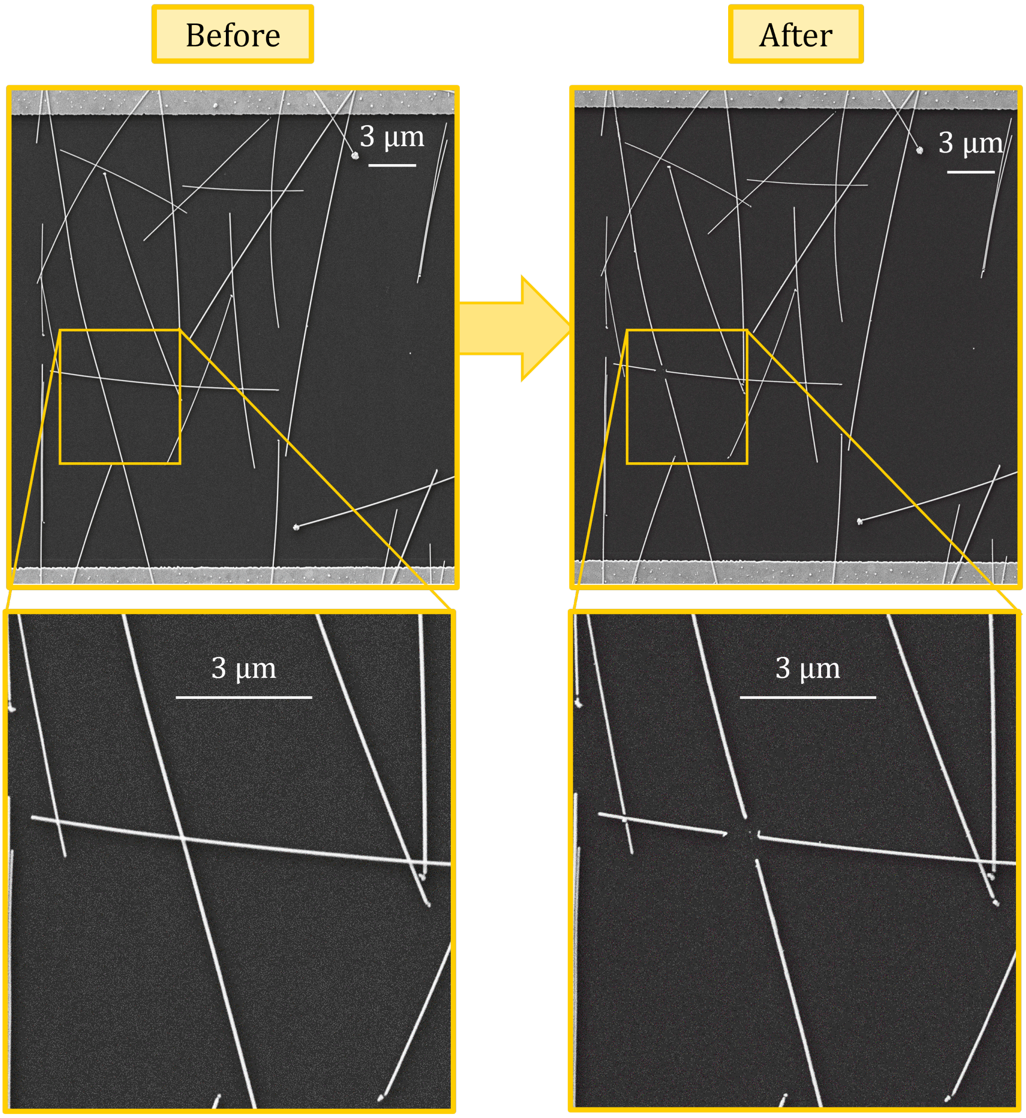

Figure 4.5: Micro-network composed of more than one NW. It can be seen that the instability affects the junction, thus impacting the two wires forming it. Zoom is performed on the wires that exhibited instabilities.

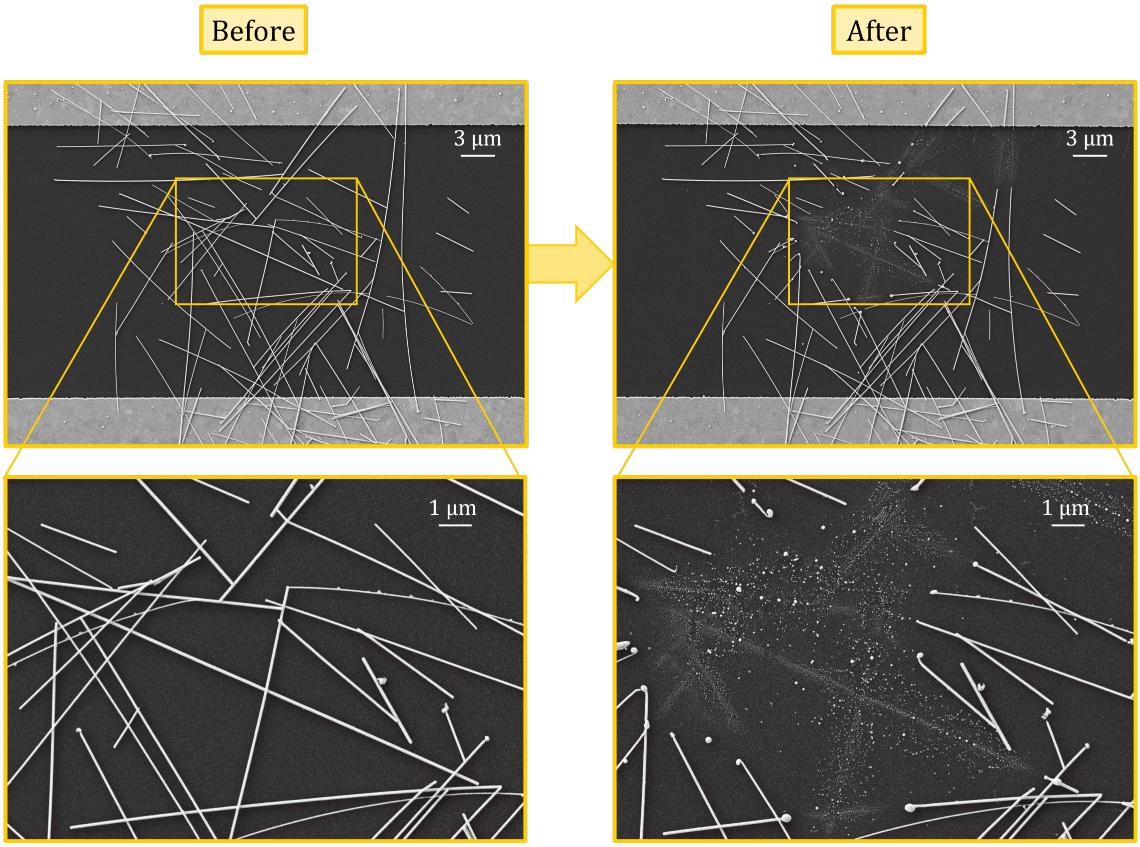

Figure 4.6: Micro-network before and after voltage application, zoom centred on the instabilities is also performed. It can be seen that the instability is multiple breakdown and affects a large area. Zoom is performed on the wires that exhibited instabilities.

The mechanisms underlying the multiple breakdown instabilities shown in Figure 4.6 are currently unknown. They might result from heat accumulation due to the Joule effect, which is often cited when voltage is applied to AgNW networks [33, 74, 85]. However, one argument may counter this hypothesis. Typically, when this form of widespread degradation occurs, the affected wires (or parts of them) vanish entirely due to the underlying instabilities. In contrast, during thermal instabilities, nanowires tend to spheroidize, which is not the case here. This realization leads to two main hypotheses:

- Locally, the network undergoes a temperature above the spheroidization temperature. For instance, Balty et al. [22] observed spheroidization at 750 °C, meaning that if these wires disappear due to heating, the network locally experiences thermal stress above this temperature. This assumption therefore implies the presence of Joule heating capable of generating temperatures higher than those observed in the NWs studied by Balty et al.

- Voltage application can cause gaps to form within the network (see Figure 4.4). These minor breaking events do not systematically lead to the failure of the percolating cluster. Therefore, if the network remains percolating, voltage continues to be applied, due to the process introduced in Section 3.1.2, which may trigger electrical breakdown at the locations of these gaps (see Figure 4.7).

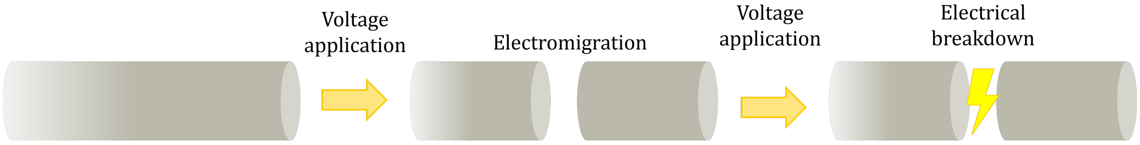

Figure 4.7: Schematic illustration of the electrical breakdown hypothesis. A single wire in the network undergoes instabilities due to electromigration. A gap is created, and if the network remains percolating, voltage application continues, which might lead to electrical breakdown.

Furthermore, this hypothesis of electrical breakdown is favoured by a phenomenon observed via SEM imaging. Following voltage application, several networks displayed a phenomenon resembling corona discharge. This manifests as white filaments forming between the nanowires.

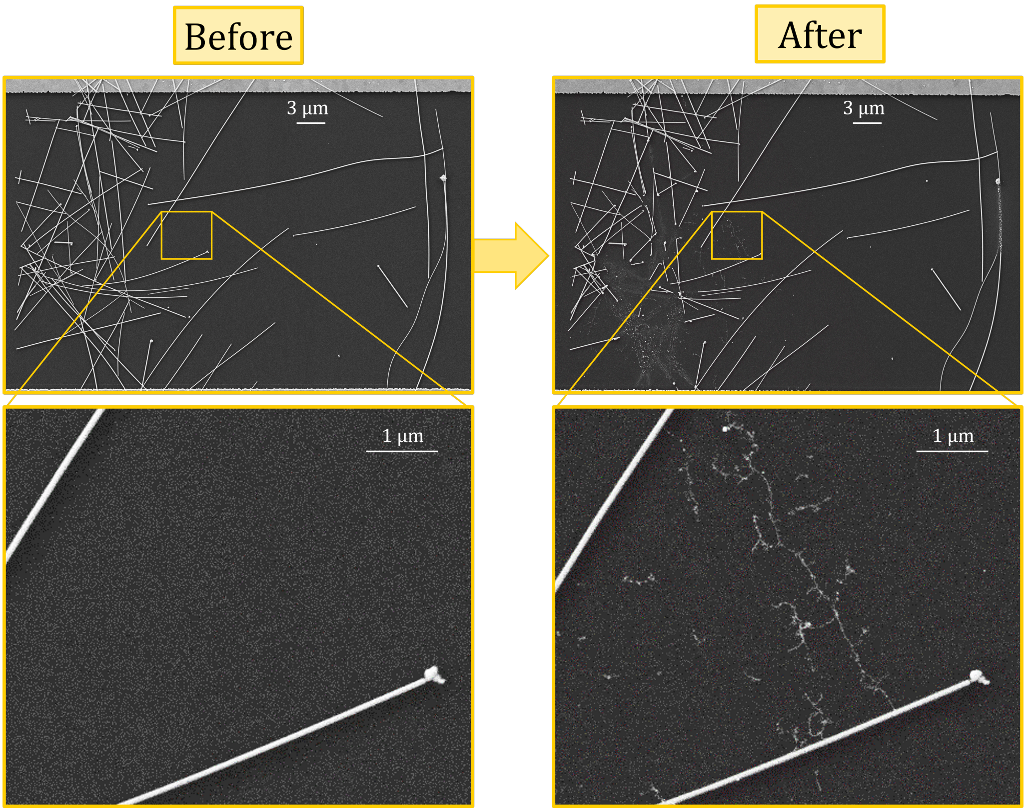

Figure 4.8: Micro-network images before and after voltage application, with a zoom highlighting the phenomenon believed to resemble corona discharge.

The composition of the filament remains unknown. This visual phenomenon could possibly be related to the formation of silver dendrites originating from electrochemical processes [115]. Access to this information and the growing process of the filament would offer insights into the behaviour of AgNW networks.

However, the appearance of these filaments is not the only unexpected instability observed after voltage application (see Figure 4.9). Indeed, several networks exhibit a displacement or bending of the NWs following the voltage application. These particular behaviours could be attributed to internal mechanical stress stored in the NWs during deposition. This hypothesis is further discussed in Section 4.2, along with its potential impact on the analysis of experimental data.

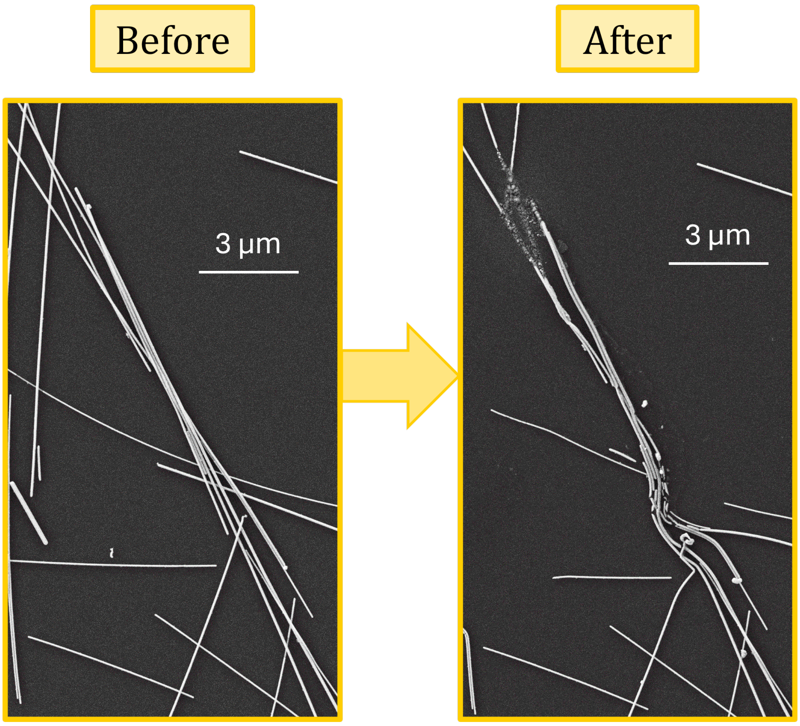

Figure 4.9: SEM images before and after voltage application reveal signs of mechanical instability.

One can also investigate the impact of magnetic interactions between two wires carrying current. Considering a maximum current density $j_{max} = 10^7\,\mathrm{A/cm^2}$ (as discussed in Section 2.2.3), a wire diameter $D = 100\,\mathrm{nm}$ a wire length $l = 10\,\mu\mathrm{m}$ and a separation between the wires $d = 1\,\mu\mathrm{m}$, the Laplace force $F_{Laplace}$ between two parallel wires can be expressed as:

$$F_{Laplace} = \frac{\mu_0 I_1 I_2 l}{2\pi d} \approx 10^{-20}\,\mathrm{N} \tag{4.1}$$

Where I_i is defined as $j_{max} \cdot \pi \cdot (\frac{D}{2})^2$, assuming the wire has a cylindrical geometry. This cylindrical geometry is adopted to simplify the calculation and to provide an order-of-magnitude estimate of the Laplace force. The magnetic permeability of free space is defined as $\mu_0 = 4\pi \times 10^{-7}\,\mathrm{H\,m^{-1}}$. The Laplace force can be compared to the static friction force to investigate potential movement due to wire interaction when a current is flowing through the wires. Assuming that the wires are completely lying on the substrate allows us to write that the intensity of the normal force (N) is equal to the weight of the wire (W). Furthermore, assuming that the static frictional coefficient between a wire and the substrate is equal to $\mu_s = 0.5$ (this frictional coefficient corresponds to the typical coefficient between a metal and silicon [116]) allows us to write the intensity of the static frictional force (F_f) as:

$$F_f = \mu_s \cdot N = \mu_s \cdot W = \mu_s \cdot \rho \cdot \pi \cdot (\frac{D}{2})^2 \cdot l \cdot g \approx 10^{-19} \tag{4.2}$$

Where, ρ is the density of bulk silver and g is the gravitational acceleration. This brief calculation suggests that the Laplace force can be neglected in the context of AgNW networks as it is 10 times lower than the frictional force.

4.2 Experimental data analysis

Following the introduction of the network's visual aspects, it is also valuable to analyse the resulting current pulses, and the resistance measured after the voltage pulses. A total of 69 micro-networks are tested using the voltage pulse application described in Section 3.1.2. Figure 4.10

present an example of the evolution of resistance as a function of the applied voltage pulse of a micro-network.

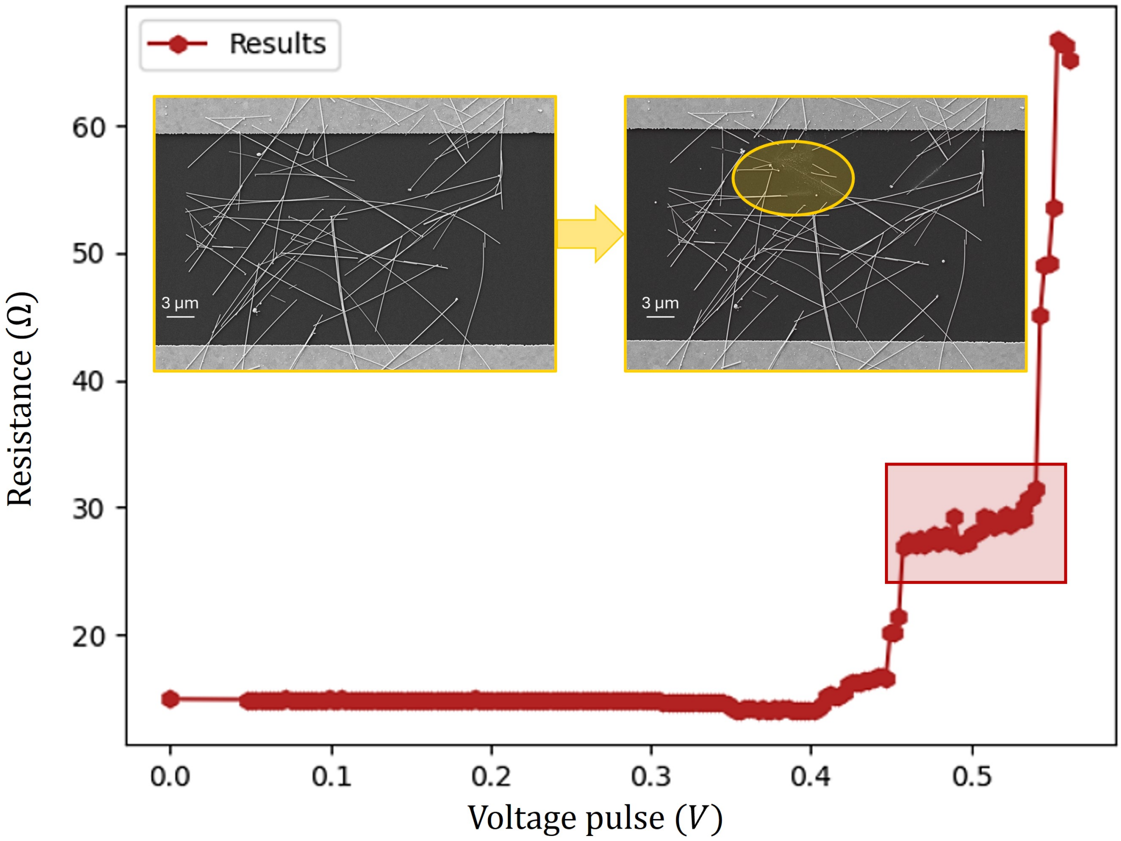

Figure 4.10: Micro-network before and after voltage application. The evolution of resistance as a function of the voltage pulse for this network can also be observed. The last point corresponding to the breaking of the network (over 10^6 Ω) is removed. This procedure is applied consistently to all the graphs presented in this section. The red box marks a plateau that follows the discrete steps, implying that the network reaches a stable configuration within this voltage interval.

It can be seen that the resistance tends to increase as the pulses become higher. Indeed, this is consistent with the assumption of generation of local defects on the NWs, which manifest as an effective decrease of the diameter (see Figure 4.11). According to Pouillet's law, the resistance increase locally, reducing the current passing trough the network at a given voltage.

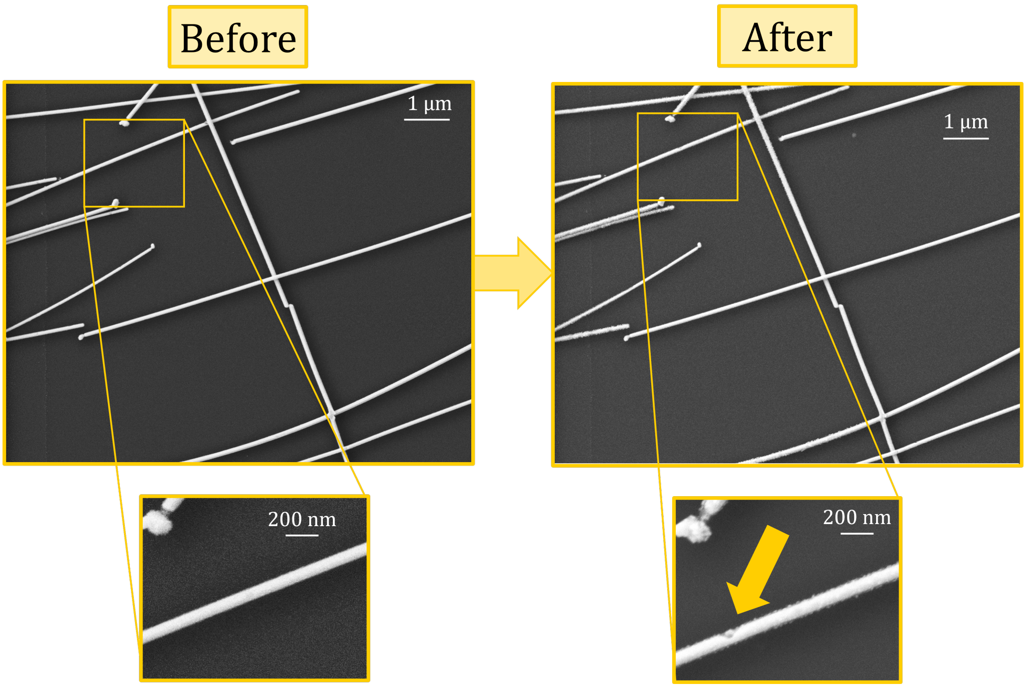

Figure 4.11: SEM images of micro-networks before and after voltage application, with a zoom on the wire where instabilities first appeared. The surface roughness observed on the nanowires after the voltage application might be due to chemical reactions occurring during the experiment.

Additionally, discrete increases in resistance can be observed. This behaviour can be linked to the percolative nature of the network. Indeed, breaking events do not necessarily disrupt the entire conducting path. If the network contains multiple percolating paths, these can break successively, one after the other. As each path fails, the overall resistance increases in discrete steps, corresponding to the sequential loss of conductive path [117]. Moreover, the steps increase are followed by plateau which indicates that the network is still percolating. In Figure 4.10, a plateau is observed between approximately 0.4 V and 0.5 V, indicating that within this voltage range, the network, despite breakdown events, reaches a stable configuration for current distribution.

While electrical stress can induce an increase in resistance, the opposite is also observed. This process is often related to the improvement of junction resistance conductivity. Indeed, through instabilities such as Joule heating and electromigration, resistance is improved via a sintering process. Figure 4.12 illustrates that this decrease occurs prior to the deterioration of the network. Atomic migrations initially lead to junction improvement. However, when higher voltage pulses are applied, deterioration develops rapidly.

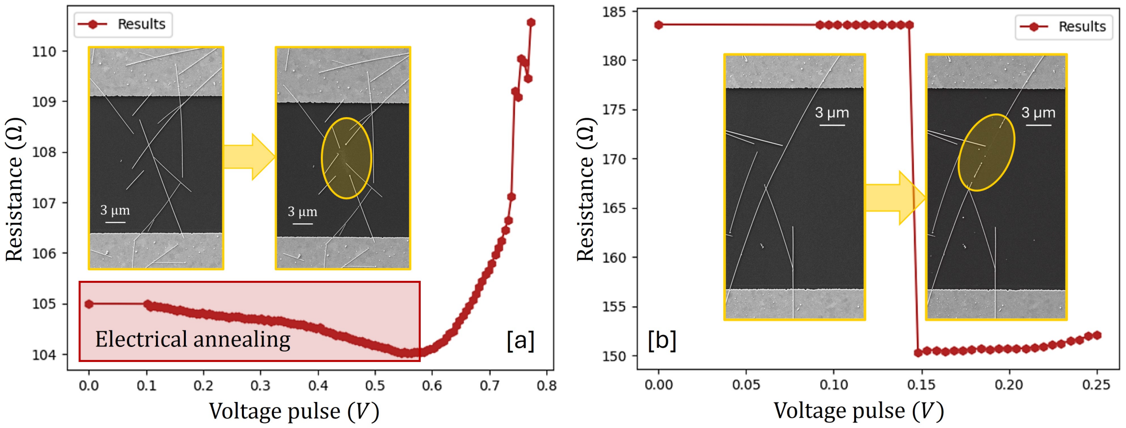

Figure 4.12: [a] Micro-network before and after the voltage application. The evolution of resistance as a function of the voltage pulse for this network can also be observed, where a monotonous decrease in resistance is visible. [b] Micro-network before and after the voltage application. The evolution of resistance as a function of the voltage pulse for this network can also be observed, where a sharp step decrease in resistance is visible.

The results reported in in Figure 4.12 [a] show a monotonous decrease in resistance related to the electrical annealing. However, this decrease is also observed in discrete steps in Figure 4.12 [b]. Analogous to the mechanism associated to the origin of resistance increase steps, the decrease steps are also assumed to be related to percolation and specifically to apparition of percolating path. This raises an important question: *how can new percolating paths appear spontaneously?* Indeed, this assumption is not straightforward, as the NWs cannot move across the substrate to form new connections. However, a three-dimensional perspective of the network may help address this problem. Let us consider the following situation (see Figure 4.14): during deposition, NWs are randomly deposited, and it can be assumed that some may fold during the process and create “bridges” above other wires. Even if this phenomenon occurs, SEM imaging performed in this work does not provide depth resolution or information surface roughness. Indeed, several NWs exhibit displacement of their ends upon breaking. Which might be due to release of energy stored via the mechanical stress during the deposition of the electrode. This phenomenon can be observed in Figure 4.13.

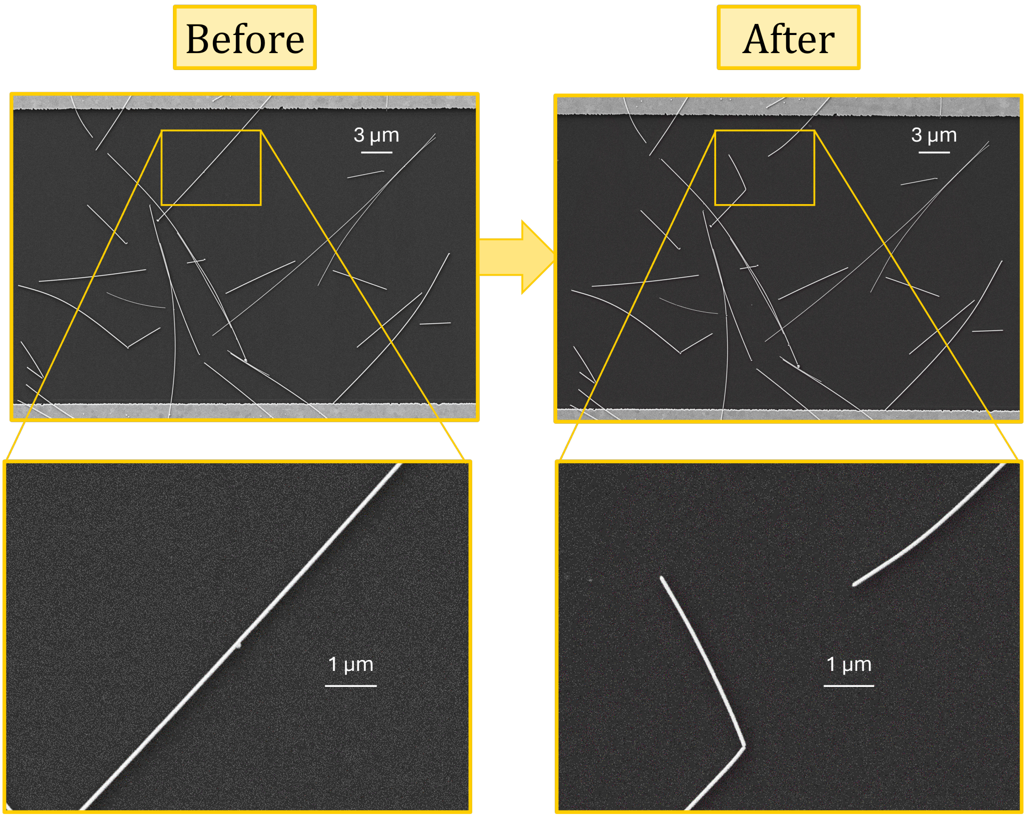

Figure 4.13: SEM image before and after voltage application with a zoom performed on a NW which illustrates the bending hypothesis. The NW which break after voltage application bend revealing potential mechanical inner stress.

Therefore, due to the applied voltage, Joule heating occurs, leading to the thermal expansion of the wires. This process could reduce the gap between two NWs. Sintering might then be triggered, fixing the junction and thereby creating a new path in the percolating network. As a result, the current flows more easily through the network, which is reflected as an abrupt resistance drop (a decrease step). Furthermore, this hypothesis is supported by two studies: Damerchi et al. [51] developed a theoretical framework to explain wire failure under thermal stress, relying on relaxation-based mechanisms, and Batra et al. [52] observed restructuring of AgNWs under current flow. To confirm this assumption, conductive atomic force microscopy (CAFM) could be employed to reveal the formation of the percolating path while a current is applied [118]. Indeed, if the CAFM captures an image of the current distribution in the network after each pulse, it can confirm or refute the hypothesis of path formation within the network.

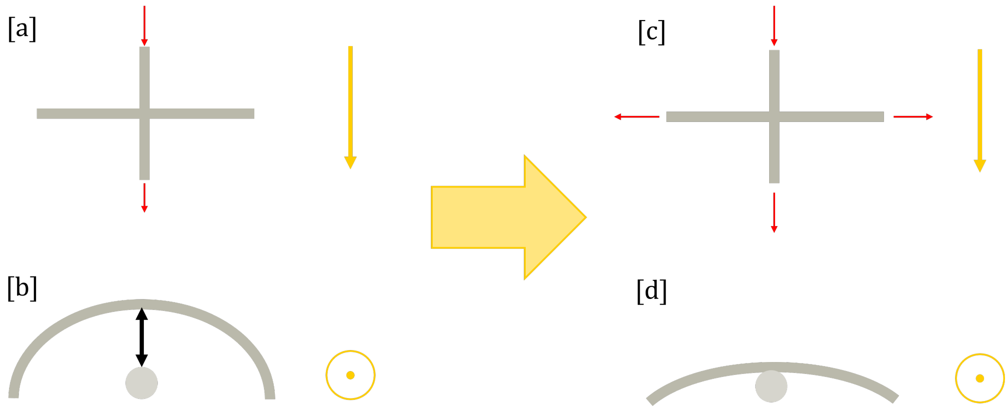

Figure 4.14: [a] Top view of the junction, as typically observed in SEM imaging. Current (red arrows) flows in one NW. The direction of the current is assumed to vary depending on the location of the electrodes and the topology of the network. [b] Schematic side view showing a nanowire forming a "bridge" above another wire. [c] After voltage application, the top view remains unchanged, as SEM imaging cannot capture vertical displacement. However, current can flow in both NW. [d] Side view after voltage application, illustrating that the wires are now in contact, possibly due to thermal expansion, thereby forming a new junction. The yellow arrow and yellow circle are placed as visual guides.

In order to evaluate the efficiency of the electrical annealing process, Figure 4.15 presents the minimum resistance as a function of the initial resistance. The data corresponding to the green area indicates that networks exhibited a resistance decrease during the application of voltage. As an indication, one network exhibited a resistance decrease of around 72% (this value is defined as R_{min}/R_{init}), which is surprising compared to the electrical annealing processes introduced (see Box 5 in Section 2.2.3). Actually, this network exhibited a huge drop in resistance around 0.15 V. The resistance between two steps dropped from a value of 283 Ω to 114 Ω. This also clearly indicates the importance of investigating this step drop when performing electrical annealing.

Indeed, Kholid et al. [87] observed a continuous decrease in resistance during the electrical annealing. They concluded that this decrease is due to an improvement of the junction quality. However, it has been shown here that discontinuous decreases may appear during annealing, which is not observed or taken into account in their study. Moreover, if this decrease in resistance is solely due to an improvement of the junction, then every low resistive network (initial resistance under 50 Ω) should exhibit this continuous resistance decrease as many junctions appear in these networks. However, in this work, some low resistive networks exhibited a resistance decrease of less than 1%, which is also unexpected compared to the results of Kholid et al. (see Figure 4.16). As this junction improvement is explained via electromigration (and Joule effect), the logical next step in this section is to discuss electromigration in NWs.

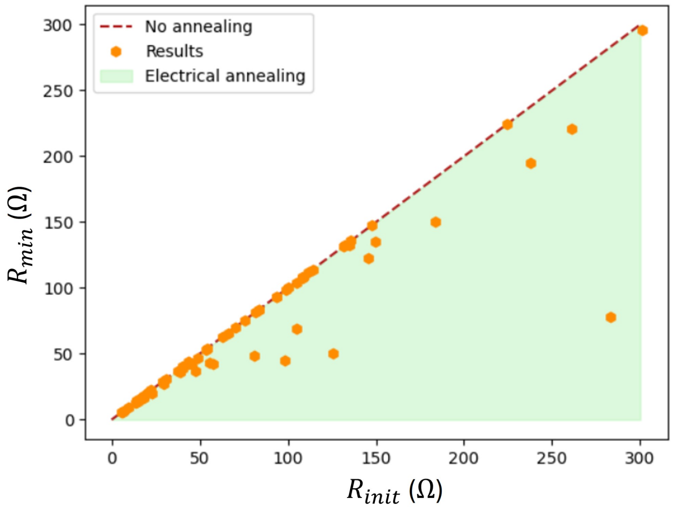

Figure 4.15: Graph of the minimal resistance (R_{min}) as a function of the initial resistance (R_{init}). A slope of 1 indicating ideal networks where no annealing occurs is also plotted.

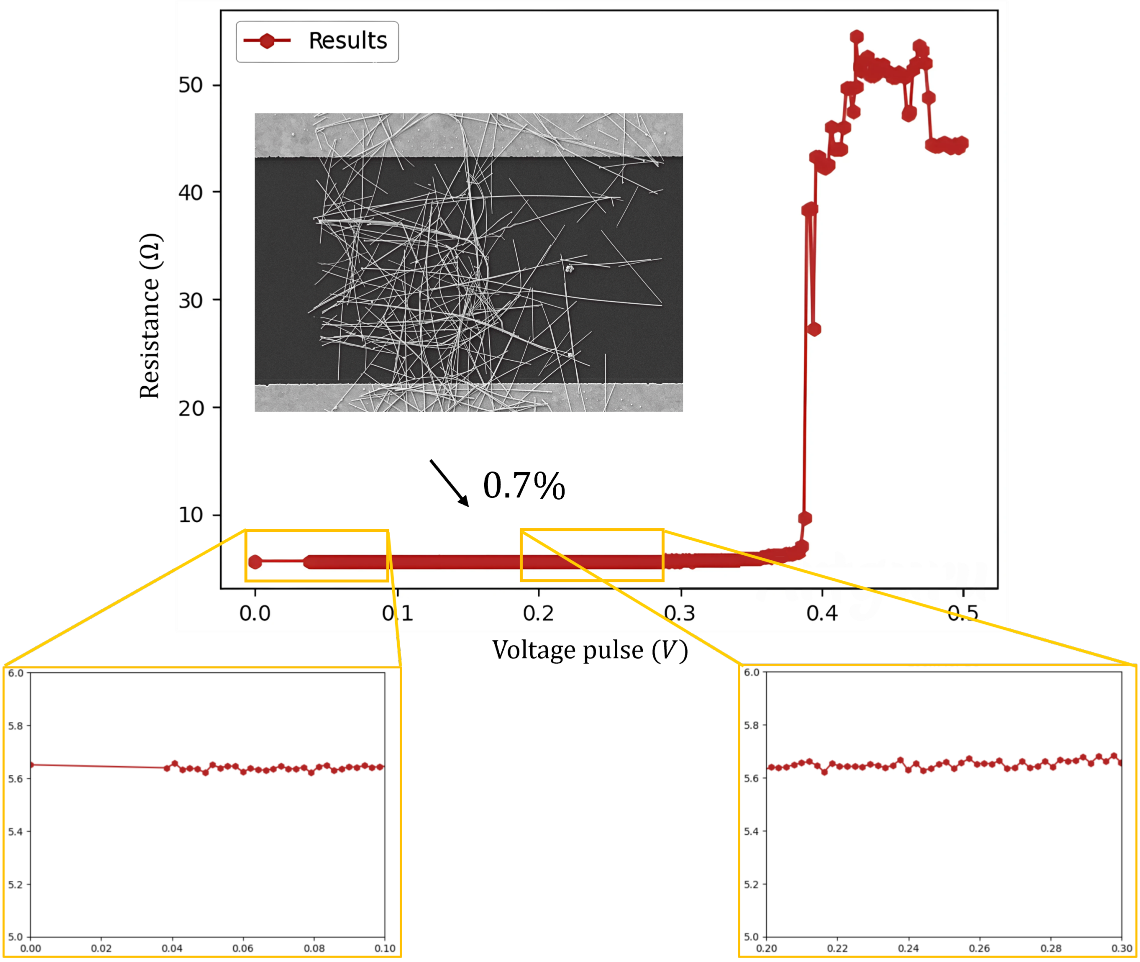

Figure 4.16: SEM image of the micro-network with its resistance evolution graph showing almost no decrease in resistance (around 0.07%).

In order to estimate the maximum current density sustainable by a NW, the analysis is restricted to networks that underwent a single breaking event. Indeed, percolation is lost by breaking just one wire, meaning that this wire carries a current exactly equal to the current measured during the voltage pulse (see Figure 4.17). Moreover, networks with a single breaking event are selected because, in these cases, the wire undergoing this pulse is known (as it is the only wire that breaks during the experiment) which helps to determine the current density flowing in this wire before the breakdown. This process could be applied to each network by focusing only on the last wire that breaks. However, the chronological order of the breaking events is unknown because images are taken only before and after the voltage is applied. Therefore, it is not possible to identify the last wire to break in networks exhibiting more than one electrical failure.

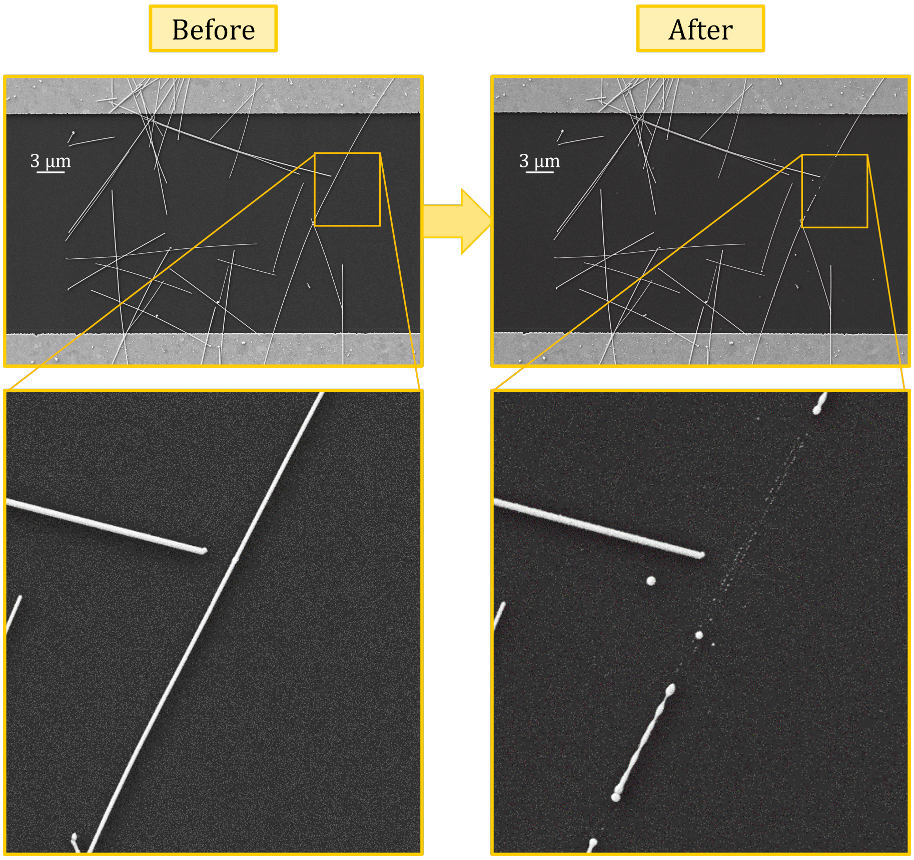

Figure 4.17: SEM image of the micro-network before and after the application of potential. One wire undergoes a breaking event which leads to the rupture of the percolating cluster.

Fifteen networks met these conditions, allowing the identification of the wire undergoing the breaking event each time. The diameter of the NWs has been measured via ImageJ software[3] to compute the cross-sectional area of the NW. Indeed, following the geometric and trigonometric properties of a pentagonal cross-section, the distance between two opposite edges of the pentagon (D) (defined more generally as the diameter in the literature) and the surface area of the pentagon (A) are linked by the following relation [119]:

$$A = \frac{5}{4}\mathrm{cotan}(36\,^{\circ})\left(\frac{D}{2\sin(54\,^{\circ})}\right)^2 \tag{4.3}$$

The maximal current density is computed by taking the last current measured during a voltage pulse and dividing it by A. The results found in this work are in good agreement with those

---

[3] Several measurements were performed along the wire to calculate a mean value, which can be used as a good approximation of the wire diameter.

reported in the literature (see Table 4.1), specifically with the findings of Waliullah and Bernal [86]. Thus, this comparison provide insight into the current density required to trigger instabilities and ultimately break a single nanowire. The value of current density found in this work can therefore be used as an input in codes simulating nanowires to predict where electrical failure will occur. Furthermore, the current density of $6.44 \times 10^7\,\mathrm{A/cm^2}$ is much higher than that reported by Patil et al. [72] (around $10^4\,\mathrm{A/cm^2}$ for bulk silver), which is encouraging for the development of NW devices capable of withstanding high current densities. The value of the maximal current density also helps to determine the electrical limits when nanowires are implemented in electronic devices.

NW Diameter (nm)	NW Structure	Maximum Current Density	Reference
340	single crystalline AgNW	$3.5 \times 10^7\,\mathrm{A/cm^2}$	Stahlmecke et al. (2006)[77]
20-80	4H-AgNW	$1.32 \times 10^8\,\mathrm{A/cm^2}$	Liu et al. (2008)[75]
53 ± 12	Pentagonal NW	$3.1 \times 10^6\,\mathrm{A/cm^2}$	Lagrange et al. (2016)[33]
70 ± 10	not mentioned	$1.63 \times 10^6\,\mathrm{A/cm^2}$	Charvin et al. (2021)[85]
53-173	Pentagonal NW	$9.7 \pm 2.96 \times 10^7\,\mathrm{A/cm^2}$	Waliullah and Bernal (2022)[86]
92.1 ± 11.2	Pentagonal NW	$6.44 \pm 2.94 \times 10^7\,\mathrm{A/cm^2}$	**This work**

Table 4.1: Table summarising the maximal current density value that a wire can undergo, along with the processes used to obtain this information in different works.

4.3 Computational model analysis

Since electrical failure is known to occur in networks, the numerical code is used as a predictive model based solely on the current-induced instability process to identify potential instabilities in AgNW networks. A comparison between the code and the experimental data is conducted to highlight the electrical failure mechanisms. As a reminder, the code is able to provide three main outputs that can be studied:

- The voltage that should be applied to break the network experimentally,
- The network's initial resistance, which can be compared to the measurements to assess the limits of the model,
- The wires experiencing the highest current therefore associated afterwards to breakdown wires event.

Accordingly, the following subsections focus on investigating these three key parameters.

4.3.1 Breaking voltage comparison

It is important to note beforehand that the simulation process used to determine the breaking voltage relies on a limited set of networks (exactly 10). While this method is not intended to precisely find the breaking voltage, the results provide valuable insight into the code's limitations.

A graph representing the experimentally measured voltage as a function of the breaking voltage pulse applied can be obtained (see Figure 4.18). As observed, the simulation does not accurately predict the breaking voltage. To better understand this discrepancy, a residuals analysis is carried out, highlighting the difference between the simulated and measured values.

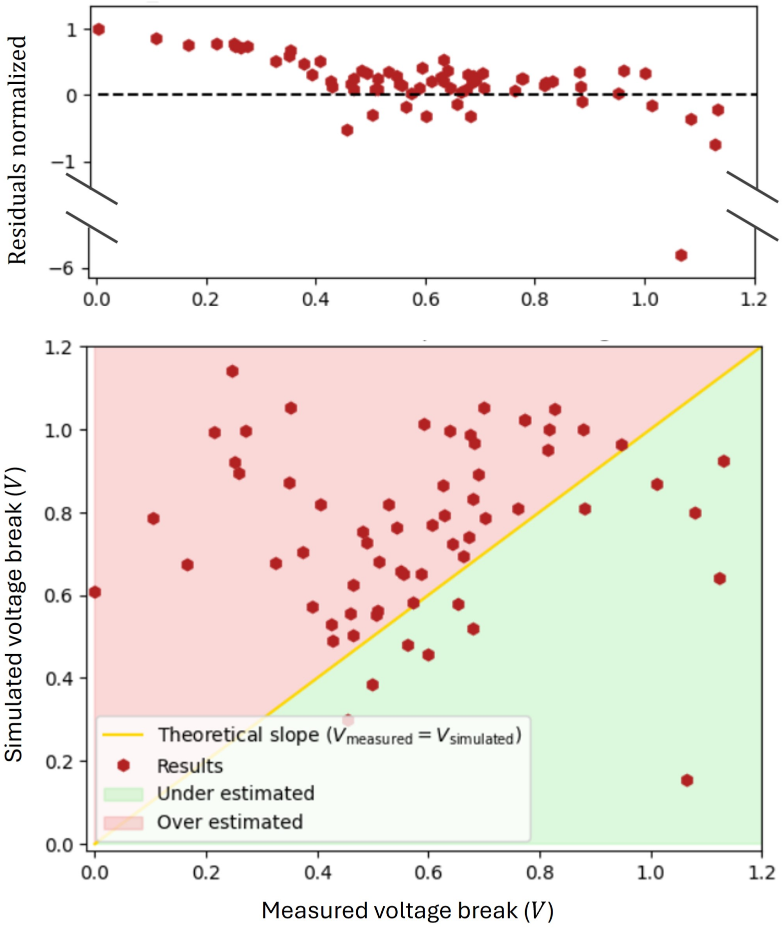

Figure 4.18: Graph showing the simulated voltage plotted against the experimentally measured breaking voltage. Residual analysis as a function of the simulated breaking voltage is also plotted above the first graph. The residuals are normalized and defined as $\frac{V_{simulated}-V_{measured}}{V_{simulated}}$. This graph shows the dispersion of residuals around zero (represented by the dashed horizontal line).

As can be seen, the normalized residuals tend to cluster around zero, indicating that the code currently provides an approximation of the breaking voltage. However, several values deviate from the expected ones. This discrepancy may be related to the method used to determine the breaking voltage. Indeed such a small dataset does not constitute a sufficient or representative sample to draw conclusions. Furthermore, the breaking voltage is likely strongly influenced by three main hypotheses made in the code.

- Neglecting defects: the code assumes that the NWs are defect-free, which is not the case experimentally. The result shown that defects promote instabilities in NWs, which can cause discrepancies between the code's predictions and the experimental results. Defects create favourable sites that serve as origins of the instabilities (see Figure 4.19). Therefore, the voltage found experimentally should be underestimated when considering defect-free NW.

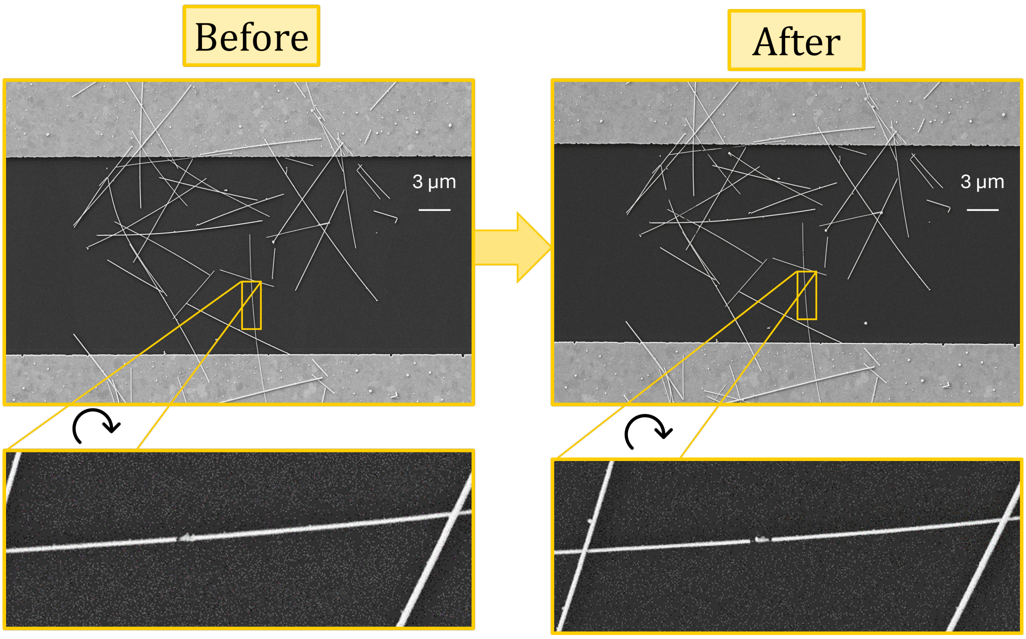

Figure 4.19: SEM images before and after the application of the voltage pulse. The orange boxes highlights the defect-dependent morphological instabilities in AgNWs. The arrows are placed to illustrate the rotation between the original image and the zoom one.

- Diameter assumption: in the experiment, NWs exhibit diameters following a Gaussian distribution (see Section 3.2). Therefore, the current distribution in the code may differ from the real one. As a result, NWs can break at higher or lower voltages depending on whether their diameter is overestimated or underestimated.

- 2D approach: in this approach, percolating paths existing in the code might be absent in the experiment. As a result, the current distribution may be completely different if this occurs. Therefore, the code could overestimate the voltage to apply, as the network possesses more percolating paths than it should.

- Fixed threshold: in this work, it was assumed that wire breaking occurs at a fixed threshold, determined using the method introduced in Chapter 3. However, according to the work of Waliullah and Bernal [86], this current threshold exhibits stochastic behaviour. As a result, assuming a constant breakdown current may lead to discrepancies with experimental data.

- Thermal effects: in this model, temperature is neglected. However, thermal effects, whether arising from Joule heating or from the surrounding environment, can influence electromigration by inducing temperature gradients within the network, or can trigger the onset of spheroidization [22].

4.3.2 Initial resistance comparison

Analysis of the computed initial resistance and the measured one is conducted in this subsection. Similarly to the breaking voltage analysis, a comparison between the experimental value and the computed one is discussed, as well as the dependence on model assumptions, with a particular focus on the junction resistance. Moreover, a discussion on the impact of the electrodes is also presented, which is often a neglected aspect in studies. For instance, in [120], the authors highlight the impact of electrode contact resistance, which appears to be non-negligible. Similarly, this approach is employed here to assess whether the assumption of perfect electrode remains valid for AgNW micro-networks.

Similarly to the breaking voltage analysis, the initial measurement is compared with the simulated one. Figure 4.20 [a] provides insight into the coherence between the model and experimental results.

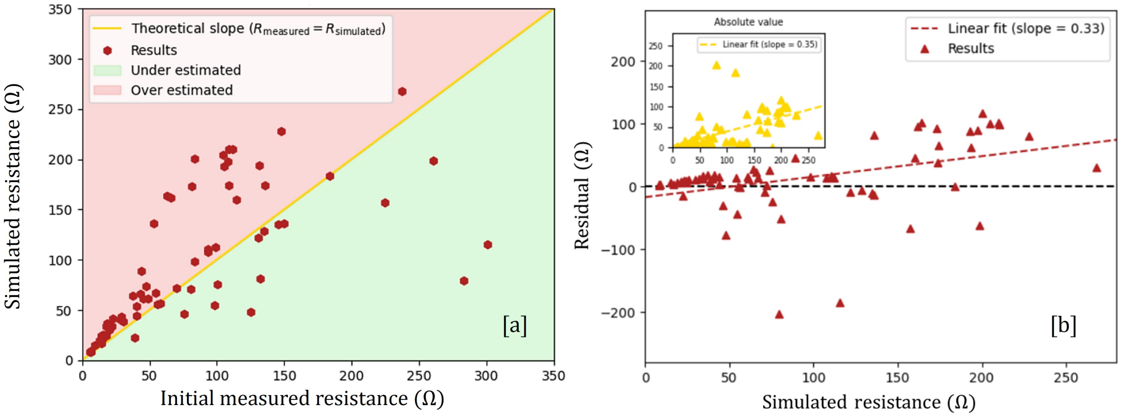

Figure 4.20: [a] Resistance found in the simulation as a function of the initially measured resistance. [b] Residual analysis as a function of the simulated resistance. The residuals are defined as $R_{simulated} - R_{measured}$. This graph shows the spread of residuals around zero (represented by the dashed horizontal line). An inset is also plotted to observe the absolute divergence of the values compared to the expected ones. In the inset, the residuals are defined as $|R_{simulated} - R_{measured}|$.

Low values of the measured resistance are relatively in good agreement with the model. However, when the resistance increases, the results tend to diverge from the expected values. This can also be observed in the residuals analysis 4.20 [b]. As observed in the breaking voltage analysis, these discrepancies can be attributed to the assumptions made in the computational model. In particular, the variations in NW diameter influence the initial resistance. For a given NW the following relation holds:

$$R = \rho \cdot \frac{l}{S} \propto \frac{1}{D^2}. \tag{4.4}$$

Consequently, assuming a uniform wire diameter in the simulation may lead to inaccuracies in predicting the initial resistance. This assumption is further supported by the data: networks with a high density of NWs typically show low resistance values (generally below 50 Ω see Figure 4.21) indicating that considering an average constant diameter is valid in this regime. This makes sense because, as the number of wires increases, the average diameter across the network approaches the expected mean value.

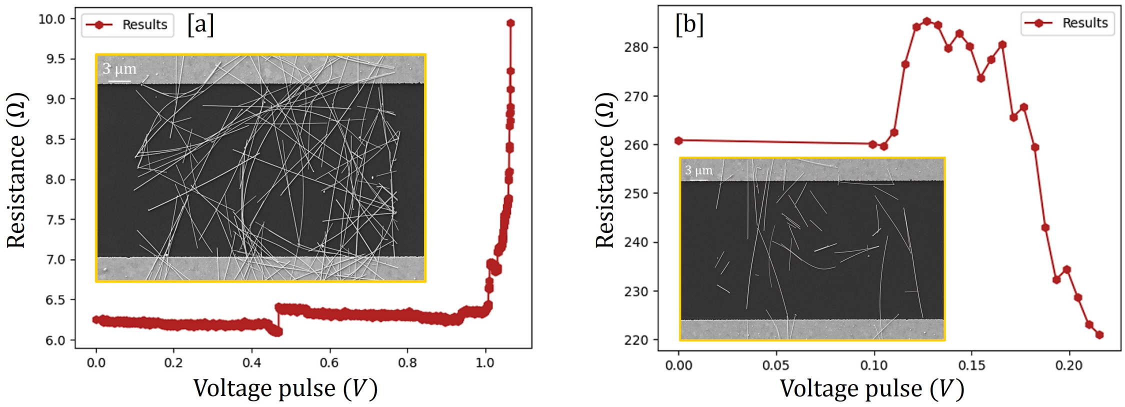

Figure 4.21: [a] SEM image of a low-resistance network with the associated resistance evolution graph. [b] SEM image of a high-resistance network with the associated resistance evolution graph.

This difference between the code and the computational model can also be related to the 2D approach. Indeed, similarly to what is explained in Section 4.3.1, some percolating paths might be absent, leading to an underestimation of the network resistance. However, the diameter is possibly not the only factor explaining this resistance discrepancy. The following paragraph addresses junction resistance as a possible explanation for the observed discrepancy.

Indeed, there is still no consensus regarding the value of the junction resistance due to its stochastic features. Therefore, this value was first estimated using the 10 networks employed as the basis for the breaking voltage analysis. The procedure to obtain this junction resistance is as follows.

- Measure the resistance of the network,
- Use the code to find the junction resistance R_j that minimizes the difference between the measured and computed values,
- Compute the mean value on the 10 R_j values obtained.

By following this procedure, the junction resistance of $35.6\,\Omega$ was obtained. This value was subsequently used for all simulations carried out on the full network.

To assess the discrepancy between the actual junction resistance and the computed value, additional networks, initially simulated using $R_j = 35.6\,\Omega$, are employed to broaden the dataset and recompute the optimized junction resistance. In other words, a larger sample (33 networks) is used for this recalculation. The distribution of the values obtained is presented in Figure 4.22[4].

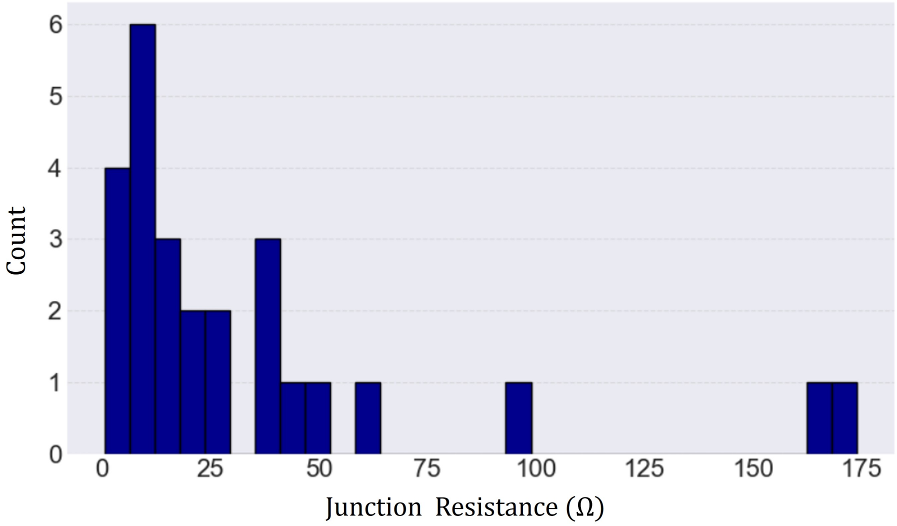

Figure 4.22: Histogram showing the distribution of R_j values recomputed across all networks analysed in this study.

These new results indicate a tendency towards low junction resistance values (below $25\,\Omega$). However, some networks exhibit unusually high junction resistances (above $150\,\Omega$). Moreover, high values (around $200\,\Omega$) appear due to the boundary condition chosen for the computational minimization, as the upper limit was set at $200\,\Omega$. These high values differ significantly from the initial estimate as well as from previously reported values in the literature ($11\,\Omega$ in the study by Bellew et al.[60], and $25.2\,\Omega$ in the work of Selzer et al.[96]) and were excluded from the data presented in Figure 4.22.

---

[4] Some networks produced negative junction resistance values during convergence, which is physically unrealistic. These cases are therefore excluded from the analysis.

The influence of the electrode has also been explored as a potential source of the discrepancy observed with the model. The idea is to consider the electrodes as non-ideal, meaning that the resistance of the junctions between the wires and the electrodes cannot be neglected. Since the value of the junction resistance is not yet well established, it is essential to focus on networks where percolation occurs through a single nanowire to investigate the electrode-wire resistance (see Figure 4.3). Out of 68 networks, 5 satisfy this condition. Firstly, Pouillet's law is used to calculate the resistance ($R_{Pouillet}$) of the each wire (therefore for each network). Thus, by measuring the length of the wire between the electrode and the diameter, the resistance can be calculated. Then, the difference between the measured resistance (R_{meas}) value and the calculated resistance was perform, this value was divided by 2 to give an insight on this electrode-wire resistance. These results are listed in Table 4.2.

Length (μm)	Diameter (nm)	$R_{mes}(\Omega)$	$R_{Pouillet}(\Omega)$	$\frac{(R_{meas}-R_{pouillet})}{2}(\Omega)$
19.14	93 ± 4	83.4	93.64	-5.12
18.69	103 ± 3	66.02	74.52	-4.25
18.72	85 ± 6	108.05	109.63	-0.79
19.47	106 ± 6	63.13	73.32	-5.1
28.54	96 ± 3	147.68	131	8.35

Table 4.2: Table summarizing the impact of the electrode-wire resistance.

These results show a slight difference between the two values, indicating that, as a good approximation, the electrode does not impact the network resistance. Surprisingly, 4 resistances out of 5 are negative, which is completely non-physical. This strange result can be attributed to an assumption made for the calculation of R_{Pouillet}. Indeed, the resistivity of the NW was supposed constant ($2.78\,\mu\Omega\,\text{cm}$) for each NW, which is not the case as it depends on the diameter, as introduced in equation 2.2. Even if these results have no physical meaning, this calculation is performed to provide insight into the junction resistance of the electrode to see if there is an impact on the overall resistance. The results also show that the contact resistance from the electrode can indeed be neglected, as it tends to be around $-1.38 \pm 5.12\,\Omega$.

4.3.3 Predicting failure in the network

As shown, the initial resistance of a network can be estimated by making several assumptions (in the case of low resistance networks). The next step is to compare the predicted locations of instabilities with those observed in networks undergoing voltage application. As previously noted, the code can iteratively break wires and thus track the location of each failure. These data are saved, enabling direct comparison with experimental observations.

The prediction analysis must be approached with caution. Initially, examination on how accurately the code can predict localization of instabilities is investigated. This analysis focuses solely on the code's ability to predict individual failures and does not claim to capture the entire breaking process within the network. To investigate this, the following procedure was followed:

1. Networks are simulated to identify the locations of breaking events,
2. These predicted breaking segments are then compared with the corresponding segments in SEM images,
3. All segments observed to break experimentally are counted.
4. The ratio of experimentally broken segments to those predicted by the simulation is calculated.

To illustrate this, an example is provided in Figure 4.23.

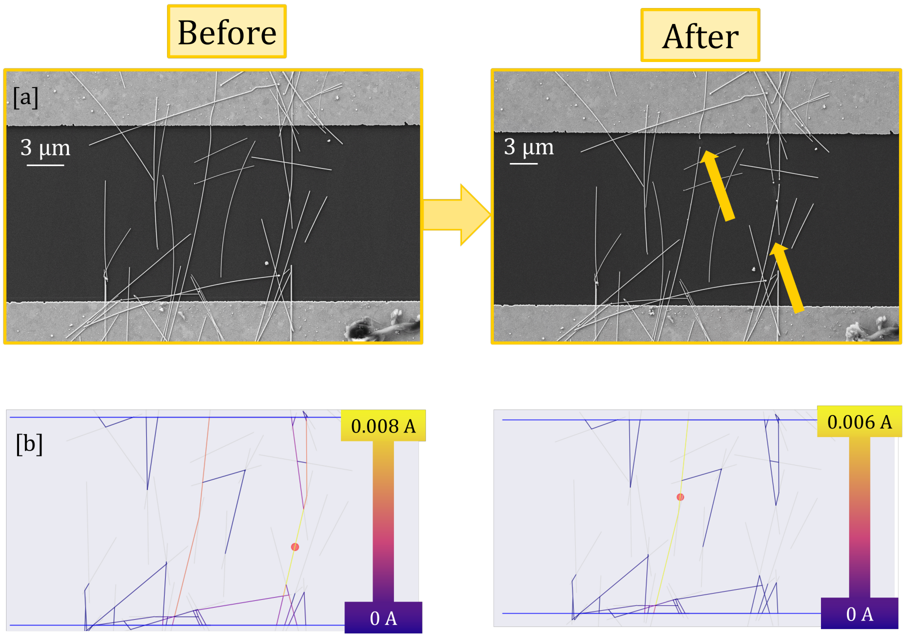

Figure 4.23: [a] SEM images of the network before and after voltage application. [b] Simulation of the network with the current distribution displayed. Red circles highlight the wire segments predicted to fail. According to the methodology described in this section, the code attains an accuracy of 50% for this network: one wire segment (left simulation) broke during the experiment, whereas the other segment (right simulation) showed no change following voltage application.

Excluding networks exhibiting unexpected events, each network is analysed and compared with its digital twin to assess the accuracy of the code. The results are presented in the histogram of Figure 4.24.

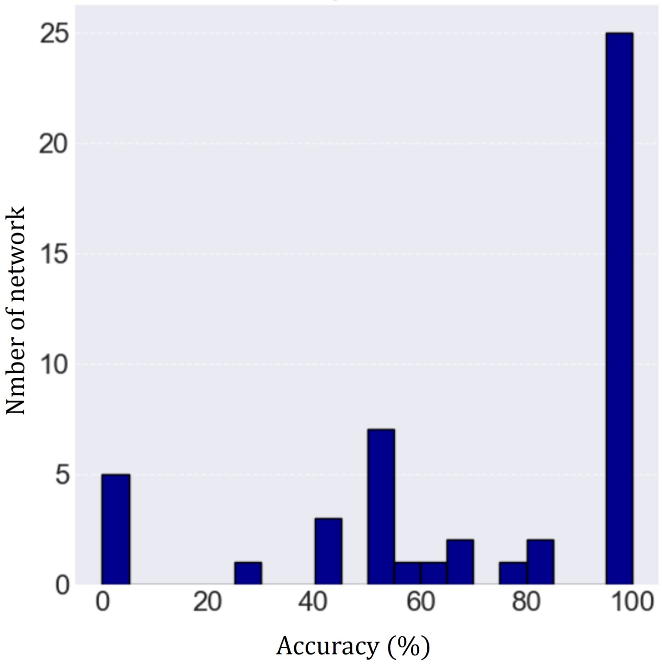

Figure 4.24: Histogram showing the breaking accuracy for 64 networks. Networks exhibiting unexpected instabilities were excluded from this analysis.

These results show that breaking events frequently occur in the wire segments predicted by the code, as indicated by the peak around 100%, which confirms the code's good ability to detect instabilities. However, the ratio of correctly predicted segments to all predicted segments (this also corresponds to the total number of predicted breaking wire identified by the code) is less satisfactory, with a computed value of 61.9%. This implies that approximately six out of ten predicted broken segments actually undergo instabilities during voltage application. It is important to compare this analysis with experimental observations. While it may seem that the code predicts about 60% of instabilities, this is misleading. Indeed a number of breaking events observed in experiments are not predicted by the model, highlighting a limitation in its current assumptions. In particular, the model does not account for collective breaking wires and breaking events involving several interconnected NWs, which are frequently seen in practice (refer to Figure 4.25 and Section 4.1). This indicates that the code might lacks precision when attempting to predict instabilities just via electromigration. Indeed, the code should be updated to account for large-scale breaking events and/or breaking events involving multiple NWs.

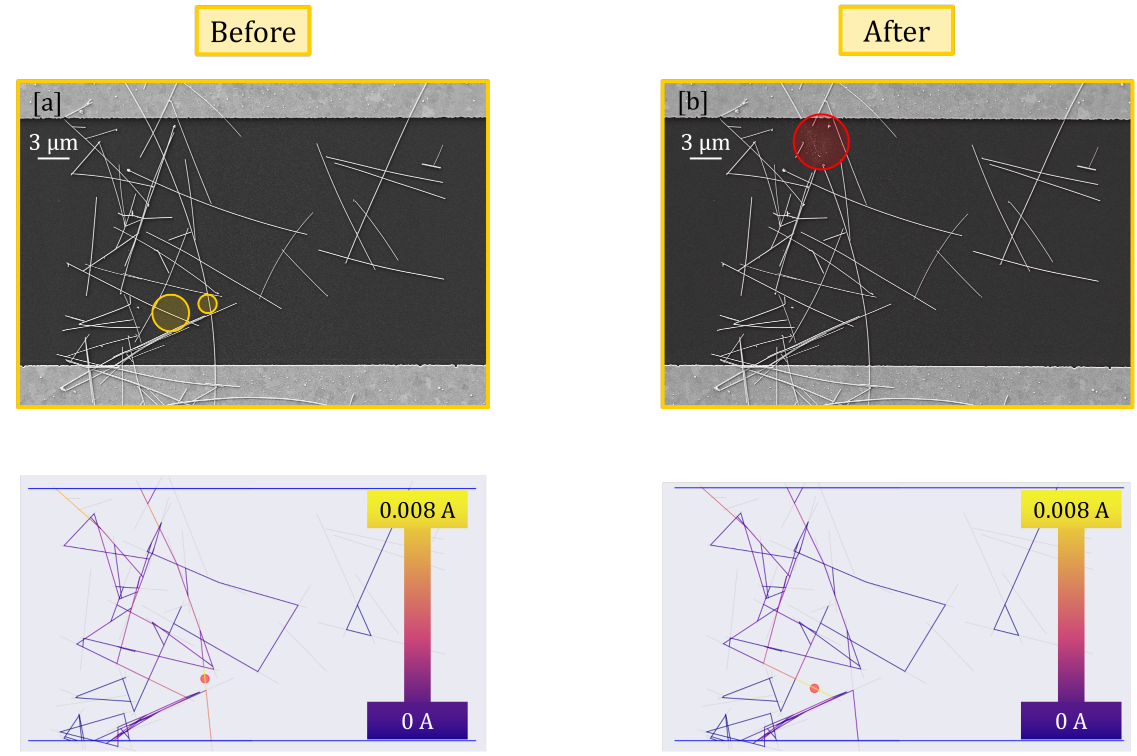

Figure 4.25: [a] SEM images before and after voltage application [b] alongside the simulation predicting the instabilities. In this case, the code does not even identify the area where instabilities occurred, indicating that it misplaces the failure locations due to several assumptions and phenomena discussed in this section.

Therefore, the code exhibits significant limitations when compared to all the breaking events observed experimentally in the network. These discrepancies can obviously also be attributed to the assumptions made in the model. For instance, assuming constant diameter and constant junction resistance leads to a different current distribution, which can lead to wire breakages at locations different from those observed experimentally. Moreover, as previously mentioned, breaking events often involve multiple wires breaking simultaneously, which is not accounted for in the code. the the code assumes the NW segment carrying the highest current breaks without affecting its neighbours, which is too a restrictive assumption. Such large-scale breaking event would result in a current distribution substantially different from that computed by the code. The 2D approach also likely contributes to the misplacement of instabilities. Finally, as discussed in Section 4.1, understanding whether breakdown events occur is another major difference between the code and experiment. It is also worth noting that heat generated by the network during experiments can influence results. For instance, the appearance of small spheres after voltage application suggests possible spheroidization, which may further explain the discrepancies between the code and experiment (see Figure 4.26). The impact of the substrate is also not discussed in this work, although it has been shown to affect the stability of nanowires [51]. Moreover, other types of instabilities not addressed here, such as chemical degradation and photodegradation, might also influence the network's stability [37]. Indeed, the networks were exposed to air and illuminated while the sample was placed in the experimental setup. Although these instabilities are not studied in this work, the methodology and instruments used can trigger light or chemical instabilities.

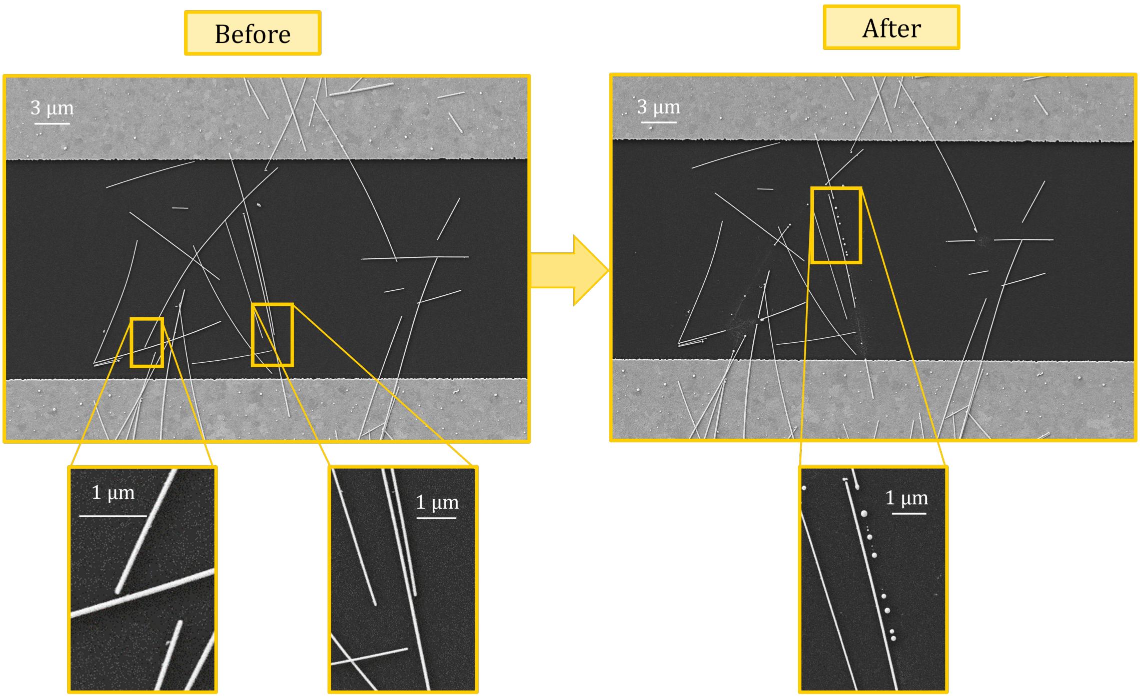

Figure 4.26: SEM images taken before and after voltage application. A zoomed-in view highlights that the wire undergoing the instability, presumed to be due to spheroidization, is theoretically not part of the percolating cluster.

To conclude this section, the model still needs improvement to accurately predict the instabilities that may occur in AgNW networks. However, certain results, such as the breaking voltage, the initial resistance, and the accuracy histogram, are promising and provide a solid basis to reinforce and enhance the current model.

Conclusion and perspectives 5

This work focused on the study of instabilities in AgNW networks under electrical stress induced by voltage pulses. Investigations into the current density triggering electrical failure in nanowires, previously unexplored instabilities induced by electrical stress, and the reliability of the numerical model were carried out through the fabrication of micro-networks. The results show that a current density of $6.44 \pm 2.94 \times 10^7$ A/cm^2 can induce instabilities in AgNWs with a diameter of 92 ± 11.2 nm. The reliability of the numerical model was investigated through digital twin analyses, which revealed discrepancies with the experimental results. However, the analysis of predicted instabilities and computed resistance showed similarities with the observations. Therefore, although the model lacks precision, it has been demonstrated that it can serve as a foundation for the development of a predictive model. The behaviour of AgNW networks under electrical stress also revealed several aspects of electrical instabilities that have not been addressed in the literature and are not accounted for in the model used in this work.

A digital twin model, was used to interpret instabilities such as electromigration in the network. Although the model successfully identified failure events, most of the events observed experimentally were entirely overlooked in the simulations. This discrepancy could be attributed to the simplifying assumptions made during model setup, such as constant nanowire diameter, neglected defects, consideration of single-wire breaking, and a purely electrical failure approach. These discrepancies also highlight the non-localized nature of electrical instabilities. Indeed, while simulations assumed that the latter instabilities would break a single wire, the experiments revealed the breaking of larger areas within the network. Therefore, the model requires further refinement to more accurately reflect reported observations. In this perspective the results obtained in this thesis such as the junction resistance, current density triggering electromigration and multiple failures process could be used to improve and calibrate the model accordingly.

Visual analysis also reveals previously unexplored aspects of AgNW instabilities. Indeed, phenomena such as dendrite formation (displacement of silver atoms), wire bending (indicating internal mechanical stress), and multiple breakdown areas (failure events involving multiple nanowires) are still not fully understood or investigated in the research topic of AgNW networks.

In future works, the role of mechanical stress could be further investigated through CAFM. Indeed, this technique allows the visualization of the current flowing through the network when voltage is applied. Therefore, the activation of percolating paths could be highlighted by this method, potentially indicating that nanowires bent during deposition and thus exhibit deformation under applied voltage. Additionally, the possible occurrence of electrical breakdown in AgNW networks could be explored by first capturing this phenomenon at a smaller scale (sub-micron electrical breakdown). Fabricating electrodes, without the deposition of AgNWs, separated by distances greater than a few dozen nanometers via lithography and applying voltage to these electrodes could help determine whether electrical breakdown can occur at the submicron-scale. Furthermore, by conducting such experiments, the impact of electrical breakdown on silver could also be studied. If confirmed, the next step would be to reproduce the phenomenon in AgNW networks to verify the assumption raised in this master's thesis.

Bibliography

5

[1] Chuanxin Wei, Liang Li, Yingying Zheng, Lizhi Wang, Jingyao Ma, Man Xu, Jinyi Lin, Linghai Xie, Panče Naumov, Xuehua Ding, Quanyou Feng, and Wei Huang. Flexible molecular crystals for optoelectronic applications. *Chemical Society Reviews*, 53(8):3687–3713, April 2024. Publisher: The Royal Society of Chemistry.

[2] Resego Phiri, Sanjay Mavinkere Rangappa, Suchart Siengchin, Oluseyi Philip Oladijo, and Togay Ozbakkaloglu. Advances in lightweight composite structures and manufacturing technologies: A comprehensive review. *Heliyon*, 10(21):e39661, 2024.

[3] Ya-Ru Ding, Rangtong Liu, Yan Zheng, Xue Wang, and Yuanyuan Yu. Fabrication of a superhydrophobic conductive porous film with water-resistance for wearable sensors. *ACS Applied Electronic Materials*, 01 2023.

[4] David Levy and Erick Castellón. *Transparent Conductive Materials: Materials, Synthesis, Characterization, Applications*. John Wiley & Sons, October 2018. Google-Books-ID: afx0DwAAQBAJ.

[5] Yonggao Jia, Chao Chen, Dan Jia, Shuxin Li, Shulin Ji, and Changhui Ye. Silver nanowire transparent conductive films with high uniformity fabricated via a dynamic heating method. *ACS Applied Materials & Interfaces*, 8, 03 2016.

[6] Marina Aburas, Veronica Soebarto, Terence Williamson, Runqi Liang, Heike Ebendorff-Heidepriem, and Yupeng Wu. Thermochromic smart window technologies for building application: A review. *Applied Energy*, 255:113522, 2019.

[7] C. G. Granqvist. Transparent conductive electrodes for electrochromic devices: A review. *Applied Physics A*, 57(1):19–24, July 1993.

[8] Tao Wang, Yu-Zhou Wang, Li-Chao Jing, Qingxia Zhu, Anita Sagadevan Ethiraj, Wenming Geng, Ying Tian, Zeru Zhu, Zhili Meng, and Hong-Zhang Geng. Novel biodegradable and ultra-flexible transparent conductive film for green light OLED devices. *Carbon*, 172:379–389, February 2021.

[9] Xuan Wang, Linjie Zhi, and Klaus Müllen. Transparent, Conductive Graphene Electrodes for Dye-Sensitized Solar Cells. *Nano Letters*, 8(1):323–327, January 2008. Publisher: American Chemical Society.

[10] S. Kiruthika and G. U. Kulkarni. Energy efficient hydrogel based smart windows with low cost transparent conducting electrodes. *Solar Energy Materials and Solar Cells*, 163:231–236, April 2017.

[11] Ran Bi, Chuantao Zheng, William W. Yu, Weitao Zheng, and Dingdi Wang. Breaking Through the Plasma Wavelength Barrier to Extend the Transparency Range of Ultrathin Indium Tin Oxide Films into the Far Infrared, October 2023. arXiv:2310.00984 [physics].

[12] Uday Shankar, Deepa Oberoi, and Anasuya Bandyopadhyay. A review on the alternative of indium tin oxide coated glass substrate in flexible and bendable organic optoelectronic device. *Polymers for Advanced Technologies*, 33(10):3078–3111, 2022. _eprint: https://onlinelibrary.wiley.com/doi/pdf/10.1002/pat.5797.

[13] Mohammad-Reza Azani, Azin Hassanpour, and Tomás Torres. Benefits, Problems, and Solutions of Silver Nanowire Transparent Conductive Electrodes in Indium Tin Oxide (ITO)-Free Flexible Solar Cells. *Advanced Energy Materials*, 10(48):2002536, 2020. _eprint: https://onlinelibrary.wiley.com/doi/pdf/10.1002/aenm.202002536.

[14] S. Sharma, S. Shriwastava, S. Kumar, K. Bhatt, and C. Charu Tripathi. Alternative transparent conducting electrode materials for flexible optoelectronic devices. *Opto-Electronics Review*, 26(3):223–235, September 2018.

[15] Zhe Cheng, Longju Liu, Shen Xu, Meng Lu, and Xinwei Wang. Temperature Dependence of Electrical and Thermal Conduction in Single Silver Nanowire. *Scientific Reports*, 5(1):10718, June 2015. Publisher: Nature Publishing Group.

[16] Guang Zeng, Weijie Chen, Xiaobin Chen, Yin Hu, Yang Chen, Ben Zhang, Haiyang Chen, Weiwei Sun, Yunxiu Shen, Yaowen Li, Feng Yan, and Yongfang Li. Realizing 17.5% efficiency flexible organic solar cells via atomic-level chemical welding of silver nanowire electrodes. *Journal of the American Chemical Society*, 144(19):8658–8668, 2022. PMID: 35469397.

[17] Munsik Oh, Won-Yong Jin, Hyeon Jeong, Mun Seok Jeong, Jae-Wook Kang, and Hyunsoo Kim. Silver nanowire transparent conductive electrodes for high-efficiency iii-nitride light-emitting diodes. *Scientific reports*, 5:13483, 09 2015.

[18] Hyungjin Lee, Donghwa Lee, Yumi Ahn, Eun-Woo Lee, Lee Soon Park, and Youngu Lee. Highly efficient and low voltage silver nanowire-based oleds employing a n-type hole injection layer. *Nanoscale*, 6:8565–8570, 2014.

[19] TaeYoung Kim, Yeon Won Kim, Ho Seok Lee, Hyeongkeun Kim, Woo Seok Yang, and Kwang S. Suh. Uniformly Interconnected Silver-Nanowire Networks for Transparent Film Heaters. *Advanced Functional Materials*, 23(10):1250–1255, 2013. _eprint: https://onlinelibrary.wiley.com/doi/pdf/10.1002/adfm.201202013.

[20] J W Park, D K Shin, J Ahn, and J Y Lee. Thermal property of transparent silver nanowire films. *Semiconductor Science and Technology*, 29(1):015002, December 2013. Publisher: IOP Publishing.

[21] Abhinav Roy, Arjun Varma R, and M. Gururajan. Phase-field study of surface diffusion enhanced break-ups of nanowire junctions. *Journal of Applied Physics*, July 2021.

[22] François Balty, Amaury Baret, Alejandro Silhanek, and Ngoc Duy Nguyen. Insight into the morphological instability of metallic nanowires under thermal stress. *Journal of Colloid and Interface Science*, 673:574–582, November 2024.

[23] Joao Resende, Dorina Papanastasiou, Dominik Moritz, Nil Fontanals, David Muñoz-Rojas, and Daniel Bellet. Time of Failure of Metallic Nanowire Networks under Coupled Electrical and Thermal Stress: Implications for Transparent Electrodes Lifetime. *ACS Applied Nano Materials*, 5, February 2022.

[24] Rajaprakash Ramachandramoorthy, Yanming Wang, Amin Aghaei, Gunther Richter, Wei Cai, and Horacio D. Espinosa. Reliability of Single Crystal Silver Nanowire-Based Systems: Stress Assisted Instabilities. *ACS Nano*, 11(5):4768–4776, May 2017. Publisher: American Chemical Society.

[25] Ehsan Marzbanrad, Geoffrey Rivers, Peng Peng, Boxin Zhao, and Norman Y. Zhou. How morphology and surface crystal texture affect thermal stability of a metallic nanoparticle: the case of silver nanobelts and pentagonal silver nanowires. *Physical Chemistry Chemical Physics*, 17(1):315–324, 2015. Publisher: Royal Society of Chemistry.

[26] Yanzhe Zhu, Tao Wan, Peiyuan Guan, Yutao Wang, Tom Wu, Zhaojun Han, Genchu Tang, and Dewei Chu. Improving thermal and electrical stability of silver nanowire network electrodes through integrating graphene oxide intermediate layers. *Journal of Colloid and Interface Science*, 566:375–382, April 2020.

[27] Chang-Lae Kim, Joon-Young Lee, Dong-Gap Shin, Jong-Souk Yeo, and Dae-Eun Kim. Mechanism of Heat-Induced Fusion of Silver Nanowires. *Scientific Reports*, 10(1):9271, June 2020. Publisher: Nature Publishing Group.

[28] Seunghoe Koo, Jaehee Park, Sangmo Koo, and Kyeongtae Kim. Local Heat Dissipation of Ag Nanowire Networks Examined with Scanning Thermal Microscopy. *The Journal of Physical Chemistry C*, 125(11):6306–6312, March 2021. Publisher: American Chemical Society.

[29] Hiesang Sohn, Chulhwan Park, Jong-Min Oh, Sang Wook Kang, and Mi-Jeong Kim. Silver Nanowire Networks: Mechano-Electric Properties and Applications. *Materials*, 12(16):2526, January 2019. Number: 16 Publisher: Multidisciplinary Digital Publishing Institute.

[30] Aaron Kobler, Thorsten Beuth, Tobias Klöffel, Robby Prang, Markus Moosmann, Torsten Scherer, Stefan Walheim, Horst Hahn, Christian Kübel, Bernd Meyer, Thomas Schimmel, and Erik Bitzek. Nanotwinned silver nanowires: Structure and mechanical properties. *Acta Materialia*, 92:299–308, June 2015.

[31] Lei Wang, Dongchen Huang, Min Li, Hua Xu, Jianhua Zou, Hong Tao, Junbiao Peng, and Miao Xu. Highly transparent and thermal-stable silver nanowire conductive film covered with ZnMgO by atomic-layer-deposition. *Journal of Physics and Chemistry of Solids*, 111:328–334, December 2017.

[32] Wenwen Wang, Zhonglin Yang, Yujia Gu, Zelei Wu, Guixin Wang, Guinan Chen, Minchu Huang, Chenhui Xu, Cui Ye, Wang Zhang, Jianwei Nai, Yongwu Peng, Jun Pan, and Changhui Ye. Enhanced stability of silver nanowire transparent conductive films against ultraviolet light illumination. *Nanotechnology*, 32(5):055603, November 2020. Publisher: IOP Publishing.

[33] Mélanie Lagrange, Thomas Sannicolo, David Muñoz-Rojas, B Lohan, Afzal Khan, M Anikin, Carmen Jiménez, Franz Bruckert, Yves Bréchet, and Daniel Bellet. Understanding the mechanisms leading to failure in metallic nanowire-based transparent heaters, and solution for stability enhancement. *Nanotechnology*, 28:055709, 12 2016.

[34] Claudia Gomes da Rocha, Hugh G. Manning, Colin O'Callaghan, Carlos Ritter, Allen T. Bellew, John J. Boland, and Mauro S. Ferreira. Ultimate conductivity performance in metallic nanowire networks. *Nanoscale*, 7(30):13011–13016, July 2015. Publisher: The Royal Society of Chemistry.

[35] Céline Mayousse, Caroline Celle, Alexandra Fraczkiewicz, and Jean-Pierre Simonato. Stability of silver nanowire based electrodes under environmental and electrical stresses. *Nanoscale*, 7:2107–2115, 2015.

[36] Thomas Sannicolo, Nicolas Charvin, Lionel Flandin, Silas Kraus, Dorina T. Papanastasiou, Caroline Celle, Jean-Pierre Simonato, David Muñoz-Rojas, Carmen Jiménez, and Daniel Bellet. Electrical Mapping of Silver Nanowire Networks: A Versatile Tool for Imaging Network Homogeneity and Degradation Dynamics during Failure. *ACS Nano*, 12(5):4648–4659, May 2018. Publisher: American Chemical Society.

[37] Fandi Chen Peiyuan Guan, Renbo Zhu andYanzhe Zhu, Zhemi Xu Tao Wan, Zhaojun Han Rakesh Joshi, Tom Wu Long Hu, Yuerui Lu, and Dewei Chu. Performance degradation and mitigation strategies of silver nanowire networks: a review. *Critical Reviews in Solid State and Materials Sciences*, 47(3):435–459, 2022.

[38] H. H. Khaligh, L. Xu, A. Khosropour, A. Madeira, M. Romano, C. Pradére, M. Tréguer-Delapierre, L. Servant, M. A. Pope, and I. A. Goldthorpe. The Joule heating problem in silver nanowire transparent electrodes. *Nanotechnology*, 28(42):425703, October 2017.

[39] Dongchen Tan, Chengming Jiang, Qikun Li, Sheng Bi, and Jinhui Song. Silver nanowire networks with preparations and applications: a review. *Journal of Materials Science: Materials in Electronics*, 31(18):15669–15696, September 2020.

[40] Shohreh Hemmati, Michael T. Harris, and Dale P. Barkey. Polyol silver nanowire synthesis and the outlook for a green process. *Journal of Nanomaterials*, 2020(1):9341983, 2020.

[41] Dongbai Zhang, Limin Qi, Jinhu Yang, Jiming Ma, Humin Cheng, and Lan Huang. Wet Chemical Synthesis of Silver Nanowire Thin Films at Ambient Temperature. *Chemistry of Materials*, 16(5):872–876, March 2004.

[42] Sergei Vlassov, Magnus Mets, Boris Polyakov, Bian Jianjun, Leonid Dorogin, and Veronika Zadin. *Abrupt elastic to plastic transition in pentagonal nanowires under bending.* August 2019.

[43] Sergei Vlassov, Boris Polyakov, Leonid M. Dorogin, Mikk Antsov, Magnus Mets, Madis Umalas, Rando Saar, Rünno Lõhmus, and Ilmar Kink. Elasticity and yield strength of pentagonal silver nanowires: In situ bending tests. *Materials Chemistry and Physics*, 143(3):1026–1031, February 2014.

[44] Chi Hao, Jiangbin Su, Peng Pan, Litao Sun, Zuming He, and Bin Tang. Structural evolution of PVP@Ag nanowires induced by focused electron beam irradiation: The passivation effect of PVP. *Journal of Materials Research and Technology*, 29:1467–1475, March 2024.

[45] Jinyoung Hwang, Youngseon Shim, Seon-Mi Yoon, Sang Hyun Lee, and Sung-Hoon Park. Influence of polyvinylpyrrolidone (PVP) capping layer on silver nanowire networks: theoretical and experimental studies. *RSC Advances*, 6(37):30972–30977, 2016.

[46] Matthew McCallum, Peter Voorhees, Michael Miksis, Stephen Davis, and Harris Wong. Capillary instabilities in solid thin films: Lines. *Journal of Applied Physics*, 79:7604–7611, May 1996.

[47] Arash Vafaei, Anming Hu, and Irene A. Goldthorpe. Joining of individual silver nanowires via electrical current. *Nano-Micro Letters*, 6(4):293–300, October 2014.

[48] Hyungseok Kang, Gi-Ra Yi, Young Jun Kim, and Jeong Ho Cho. Junction Welding Techniques for Metal Nanowire Network Electrodes. *Macromolecular Research*, 26(12):1066–1073, December 2018.

[49] Daniel Langley, Mélanie Lagrange, Gaël Giusti, Carmen Jiménez, Yves Bréchet, Ngoc Duy Nguyen, and Daniel Bellet. Metallic nanowire networks: Effects of thermal annealing on electrical resistance. *Nanoscale*, 6, 09 2014.

[50] Erik C. Garnett, Wenshan Cai, Judy J. Cha, Fakhruddin Mahmood, Stephen T. Connor, M. Greyson Christoforo, Yi Cui, Michael D. McGehee, and Mark L. Brongersma. Self-limited plasmonic welding of silver nanowire junctions. *Nature Materials*, 11(3):241–249, February 2012.

[51] Elyad Damerchi, Sven Oras, Edgars Butanovs, Allar Liivlaid, Mikk Antsov, Boris Polyakov, Annamarija Trausa, Veronika Zadin, Andreas Kyritsakis, Loïc Vidal, Karine Mougin, Siim Pikker, and Sergei Vlassov. Heat-induced morphological changes in silver nanowires deposited on a patterned silicon substrate. *Beilstein Archives*, January 2024.

[52] Nitin M. Batra, Ahad Syed, and P. Costa. Current-induced restructuring in bent silver nanowires. *Nanoscale*, 11, 01 2019.

[53] Yuwen Zhu, Yujun Deng, Peiyun Yi, Linfa Peng, Xinmin Lai, and Zhongqin Lin. Flexible transparent electrodes based on silver nanowires: Material synthesis, fabrication, performance, and applications. *Advanced Materials Technologies*, 4, 08 2019.

[54] Geoffrey Deignan and Irene A. Goldthorpe. The dependence of silver nanowire stability on network composition and processing parameters. *RSC Adv.*, 7:35590–35597, 2017.

[55] A. Graff, D. Wagner, H. Ditlbacher, and U. Kreibig. Silver nanowires. *The European Physical Journal D - Atomic, Molecular, Optical and Plasma Physics*, 34(1):263–269, July 2005.

[56] Aveek Bid, Achyut Bora, and A. K. Raychaudhuri. Temperature dependence of the resistance of metallic nanowires of diameter $\geqslant 15$ nm: Applicability of bloch-grüneisen theorem. *Phys. Rev. B*, 74:035426, Jul 2006.

[57] Mélanie Lagrange, Daniel Langley, Gaël Giusti, Carmen Jiménez, Yves Bréchet, and Daniel Bellet. Optimization of silver nanowire-based transparent electrodes: Effects of density, size and thermal annealing. *Nanoscale*, 7, October 2015.

[58] Matweb material property data. `https://www.matweb.com/search/DataSheet.aspx?MatGUID=63cbd043a31f4f739ddb7632c1443d33&ckck=1`. Accessed Mai 27 2025.

[59] U. Kreibig and C. v. Fragstein. The limitation of electron mean free path in small silver particles. *Zeitschrift für Physik*, 224(4):307–323, August 1969.

[60] Allen Bellew, Hugh Manning, Claudia Gomes da Rocha, Mauro Ferreira, and John Boland. Resistance of Single Ag Nanowire Junctions and Their Role in the Conductivity of Nanowire Networks. *ACS nano*, 9, October 2015.

[61] Rose M. Mutiso, Michelle C. Sherrott, Aaron R. Rathmell, Benjamin J. Wiley, and Karen I. Winey. Integrating simulations and experiments to predict sheet resistance and optical transmittance in nanowire films for transparent conductors. *ACS nano*, 7(9):7654–7663, September 2013.

[62] Jung-Yong Lee, Stephen Connor, Yi Cui, and Peter Peumans. Solution-Processed Metal Nanowire Mesh Transparent Electrodes. *Nano letters*, 8:689–92, March 2008.

[63] Liangbing Hu, Han Sun Kim, Jung-Yong Lee, Peter Peumans, and Yi Cui. Scalable coating and properties of transparent, flexible, silver nanowire electrodes. *ACS nano*, 4(5):2955–2963, May 2010.

[64] Tze-Bin Song, Yu Chen, Choong-Heui Chung, Yang (Michael) Yang, Brion Bob, Hsin-Sheng Duan, Gang Li, King-Ning Tu, Yu Huang, and Yang Yang. Nanoscale Joule Heating and Electromigration Enhanced Ripening of Silver Nanowire Contacts. *ACS Nano*, 8(3):2804–2811, March 2014. Publisher: American Chemical Society.

[65] Dietrich Stauffer, Amnon Aharony, and Sidney Redner. Introduction to Percolation Theory. *Physics today*, 46(4):64–64, 1993.

[66] Daniel Langley. *Silver Nanowire Networks: Effects of Percolation and Thermal Annealing on Physical Properties.* Ph.D., Universite de Liege (Belgium), Belgium, 2014. ISBN: 9798384147015.

[67] Wonho Jeong, Kyeongtae Kim, Youngsang Kim, Woochul Lee, and Pramod Reddy. Corrigendum: Characterization of nanoscale temperature fields during electromigration of nanowires. *Scientific reports*, 4:4975, 07 2014.

[68] Danvers E. Johnston, Douglas R. Strachan, and A. T. Charlie Johnson. Parallel Fabrication of Nanogap Electrodes. *Nano Letters*, 7(9):2774–2777, September 2007. Publisher: American Chemical Society.

[69] P. S. Ho and T. Kwok. Electromigration in metals. *Reports on Progress in Physics*, 52(3):301, March 1989.

[70] Joseph Lombardo. *Tailoring weak links by electromigration.* PhD thesis, ULiège - Université de Liège, 13 September 2019.

[71] James R. Black. Mass Transport of Aluminum by Momentum Exchange with Conducting Electrons. In *6th Annual Reliability Physics Symposium (IEEE)*, pages 148–159, November 1967. ISSN: 0735-0791.

[72] H.R. Patil and H.B. Huntington. Electromigration and associated void formation in silver. *Journal of Physics and Chemistry of Solids*, 31(3):463–474, 1970.

[73] Zesheng Shen, Siyi Jing, Yiyuan Heng, Yifan Yao, K. N. Tu, and Yingxia Liu. Electromigration in three-dimensional integrated circuits. *Applied Physics Reviews*, 10(2):021309, 05 2023.

[74] Hadi Hosseinzadeh Khaligh and Irene A. Goldthorpe. Failure of silver nanowire transparent electrodes under current flow. *Nanoscale Research Letters*, 8(1):235, May 2013.

[75] Xiaohua Liu, Jing Zhu, Chuanhong Jin, Lian-Mao Peng, Dai-Ming Tang, and Huiming Cheng. In situ electrical measurements of polytypic silver nanowires. *Nanotechnology*, 19:085711, 02 2008.

[76] Benjamin J. Wiley, Zenghui Wang, Jiang Wei, Yadong Yin, David H. Cobden, and Younan Xia. Synthesis and electrical characterization of silver nanobeams. *Nano Letters*, 6(10):2273–2278, 2006. PMID: 17034096.

[77] Burkhard Stahlmecke, Frank Meyer zu Heringdorf, L. Chelaru, Michael Horn-von Hoegen, G. Dumpich, and Kelly Roos. Electromigration in self-organized single-crystalline silver nanowires. *Applied Physics Letters*, 88:053122–053122, 02 2006.

[78] Shih-Ming Kuo and Kwang-Lung Lin. Polarity effect of electromigration on intermetallic compound formation in a Cu/Sn–9Zn/Cu sandwich. *Journal of Materials Research*, 23(4):1087–1094, April 2008.

[79] Kaiqing Wang, Yunxia Jin, Xiaocun Wang, Baifan Qian, Jianzhong Wang, and Fei Xiao. Investigation into the failure mechanism of silver nanowire network film under electrical stress. In *2020 IEEE 70th Electronic Components and Technology Conference (ECTC)*, pages 1218–1224, Orlando, FL, USA, June 2020. IEEE.

[80] Burkhard Stahlmecke and Guenter Dumpich. In situ observation of electromigration in gold nanowires. *Defect and Diffusion Forum*, 237-240:1163–1167, 04 2005.

[81] K. N. Tu. Recent advances on electromigration in very-large-scale-integration of interconnects. *Journal of Applied Physics*, 94(9):5451–5473, November 2003.

[82] D.G. Pierce and P.G. Brusius. Electromigration: A review. *Microelectronics Reliability*, 37(7):1053–1072, July 1997.

[83] RICHARD S. SORBELLO. Theory of electromigration. In Henry Ehrenreich and Frans Spaepen, editors, *Solid State Physics*, volume 51 of *Solid State Physics*, pages 159–231. Academic Press, 1998.

[84] Raju P. Gupta. Theory of electromigration in noble and transition metals. *Phys. Rev. B*, 25:5188–5196, Apr 1982.

[85] Nicolas Charvin, Joao Resende, Dorina T. Papanastasiou, David Muñoz-Rojas, Carmen Jiménez, Ali Nourdine, Daniel Bellet, and Lionel Flandin. Dynamic degradation of metallic nanowire networks under electrical stress: a comparison between experiments and simulations. *Nanoscale Adv.*, 3:675–681, 2021.

[86] Mohammad Waliullah and Rodrigo Bernal. Current density at failure of twinned silver nanowires. *Nanotechnology*, 33, May 2022.

[87] Farhan Nur Kholid, Hui Huang, Yongqi Zhang, and Hong Jin Fan. Multiple electrical breakdowns and electrical annealing using high current approximating breakdown current of silver nanowire network. *Nanotechnology*, 27(2):025703, dec 2015.

[88] Dengming Xiao. *Gas Discharge and Gas Insulation.* Springer, Berlin, Heidelberg, 2016.

[89] Boris M. Smirnov. Cathode and Wall Processes. In Boris M. Smirnov, editor, *Theory of Gas Discharge Plasma*, pages 229–256. Springer International Publishing, Cham, 2015.

[90] Michael Lieberman and Alan Lichtenberg. Principles of plasma discharges and materials processing: Second edition. *Principles of Plasma Discharges and Materials Processing, 2nd Edition, by Michael A. Lieberman, Alan J. Lichtenberg, pp. 800. ISBN 0-471-72001-1. Wiley-VCH , September 2003.*, 30, 09 2003.

[91] Sajjad Rahmanzadeh and Mir Pishvaee. Electron radar search algorithm: a novel developed meta-heuristic algorithm. *Soft Computing*, 24:1–23, 06 2020.

[92] Corona discharge – factors affecting corona. `https://electricalbaba.com/corona-discharge-factors-affecting-corona-2/`, 2016. Accessed April 8 2025.

[93] Glow discharge. `https://en.wikipedia.org/wiki/Glow_discharge`, 2024. Accessed April 8 2025.

[94] How to build a jacob's ladder. `https://www.popsci.com/how-to-build-jacobs-ladder/`, 2021. Accessed April 8 2025.

[95] Jessamyn A. Fairfield, Carlos Ritter, Allen T. Bellew, Eoin K. McCarthy, Mauro S. Ferreira, and John J. Boland. Effective Electrode Length Enhances Electrical Activation of Nanowire Networks: Experiment and Simulation. *ACS Nano*, 8(9):9542–9549, September 2014.

[96] Franz Selzer, Carlo Floresca, David Kneppe, Ludwig Bormann, Christoph Sachse, Nelli Weiß, Alexander Eychmüller, Aram Amassian, Lars Müller-Meskamp, and Karl Leo. Electrical limit of silver nanowire electrodes: Direct measurement of the nanowire junction resistance. *Applied Physics Letters*, 108(16):163302, April 2016.

[97] D Fantanas, A Brunton, S J Henley, and R A Dorey. Investigation of the mechanism for current induced network failure for spray deposited silver nanowires. *Nanotechnology*, 29(46):465705, sep 2018.

[98] Moritz Glatt, Chantal Sinnwell, Li Yi, Sean Donohoe, Bahram Ravani, and Jan C. Aurich. Modeling and implementation of a digital twin of material flows based on physics simulation. *Journal of Manufacturing Systems*, 58:231–245, January 2021.

[99] Alexandre Vallée. Digital twin for healthcare systems. *Frontiers in Digital Health*, 5, September 2023. Publisher: Frontiers.

[100] Hui Xiong, Congying Chu, Lingzhong Fan, Ming Song, Jiaqi Zhang, Yawei Ma, Ruonan Zheng, Junyang Zhang, Zhengyi Yang, and Tianzi Jiang. The Digital Twin Brain: A Bridge between Biological and Artificial Intelligence. *Intelligent Computing*, 2:0055, September 2023. Publisher: American Association for the Advancement of Science.

[101] Yifang Chen. Nanofabrication by electron beam lithography and its applications: A review. *Microelectronic Engineering*, 135:57–72, March 2015.

[102] KayakuAM. Pmma and copolymer. `https://kayakuam.com/wp-content/uploads/2021/07/KAM-PMMA-Datasheet-4.12.21-final.pdf`, 2021. Accessed April 20 2025.

[103] Niranjan Sahu, B. Parija, and S. Panigrahi. Fundamental understanding and modeling of spin coating process: A review. *Indian Journal of Physics*, 83(4):493–502, April 2009.

[104] Robert Pasquarelli, David Ginley, and Ryan O'Hayre. ChemInform Abstract: Solution Processing of Transparent Conductors: From Flask to Film. *Chemical Society reviews*, 40:5406–41, June 2011.

[105] D. P. Birnie. Spin Coating Technique. In Michel A. Aegerter and Martin Mennig, editors, *Sol-Gel Technologies for Glass Producers and Users*, pages 49–55. Springer US, Boston, MA, 2004.

[106] Jan-Otto Carlsson and Peter M. Martin. Chapter 7 - Chemical Vapor Deposition. In Peter M. Martin, editor, *Handbook of Deposition Technologies for Films and Coatings (Third Edition)*, pages 314–363. William Andrew Publishing, Boston, January 2010.

[107] Donald M. Mattox. *Handbook of Physical Vapor Deposition (PVD) Processing.* William Andrew, April 2010. Google-Books-ID: aGUxoVTYjA8C.

[108] Hamza Ichou, Nadia Arrousse, Elyor Berdimurodov, and Nizomiddin Aliev. Exploring the Advancements in Physical Vapor Deposition Coating: A Review. *Journal of Bio- and Tribo-Corrosion*, 10(1):3, November 2023.

[109] Lu Kang, Hui Chen, Zhong-Jian Yang, Yongbo Yuan, Han Huang, Bingchu Yang, Yongli Gao, and Conghua Zhou. Seesaw-like polarized transmission behavior of silver nanowire arrays aligned by off-center spin-coating. *Journal of Applied Physics*, 123(20):205110, May 2018.

[110] Keithley model 2450-ec / 2460-ec potentiostats electrochemistry lab systems self-guided demo tou. `https://www.tek.com/en/keithley-source-measure-units/smu-2450-60-graphical-sourcemeter-manual-12`. Accessed Mai 19 2025.

[111] Caroline Celle, Céline Mayousse, Eléonore Moreau, Henda Basti, Alexandre Carella, and Jean-Pierre Simonato. Highly flexible transparent film heaters based on random networks of silver nanowires. *Nano Research*, 5(6):427–433, June 2012.

[112] Qucs technical papers. `https://qucs.github.io/docs/technical/technical.pdf`. Accessed Mai 19 2025.

[113] Modified nodal analysis. `https://spicesharp.github.io/SpiceSharp/index.html`. Accessed Mai 19 2025.

[114] Rajaprakash Ramachandramoorthy, Yanming Wang, Amin Aghaei, Gunther Richter, Wei Cai, and Horacio D. Espinosa. Reliability of Single Crystal Silver Nanowire-Based Systems: Stress Assisted Instabilities. *ACS Nano*, 11(5):4768–4776, May 2017.

[115] Michael N. Kozicki and. Information in electrodeposited dendrites. *Advances in Physics: X*, 6(1):1920846, 2021.

[116] H. Mishina and D. H. Buckley. Friction behavior of silicon in contact with titanium, nickel, silver and copper, September 1984. NTRS Author Affiliations: Institute of Physical and Chemical Research, NASA Lewis Research Center NTRS Report/Patent Number: E-2036 NTRS Document ID: 19840025519 NTRS Research Center: Legacy CDMS (CDMS).

[117] Thomas Sannicolo, David Muñoz-Rojas, Ngoc Duy Nguyen, Stéphane Moreau, Caroline Celle, Jean-Pierre Simonato, Yves Bréchet, and Daniel Bellet. Direct Imaging of the Onset of Electrical Conduction in Silver Nanowire Networks by Infrared Thermography: Evidence of Geometrical Quantized Percolation. *Nano Letters*, 16(11):7046–7053, November 2016.

[118] Joseph Shaw, Ajay Perumal, Donal Bradley, Paul Stavrinou, and Thomas Anthopoulos. Nanoscale current spreading analysis in solution-processed graphene oxide/silver nanowire transparent electrodes via conductive atomic force microscopy. *Journal of Applied Physics*, 119:195501, May 2016.

[119] Mélanie Lagrange. *Physical analysis of percolating silver nanowire networks used as transparent electrodes for flexible applications.* phdthesis, Université Grenoble Alpes, October 2015.

[120] Huading Song, Zitong Zhang, Dong Pan, Donghao Liu, Zhaoyu Wang, Zhan Cao, Lei Liu, Lianjun Wen, Dunyuan Liao, Ran Zhuo, Dong E. Liu, Runan Shang, Jianhua Zhao, and Hao Zhang. Large zero bias peaks and dips in a four-terminal thin InAs-Al nanowire device. *Physical Review Research*, 4(3):033235, September 2022. Publisher: American Physical Society.